# Postpolymerization Modification of Polystyrene-*block*-poly(methyl methacrylate) to Fabricate 10-nm-Scale Microphase-Separated Structure

***A Dissertation for the Degree of Doctor of Philosophy***

Kohei Yoshida

Hokkaido University

March 2019

## *Acknowledgements*

The study presented in this dissertation has been performed under the direction of Professor Toshifumi Satoh, Division of Applied Chemistry, Faculty of Engineering, Hokkaido University, from 2016 to 2019. The author wishes to express his sincere appreciation to Professor Toshifumi Satoh, for his kind instruction, helpful advice, and unstinting encouragement during the course of this work.

The author is deeply grateful to Assistant Professor Takuya Isono, Division of Applied Chemistry, Faculty of Engineering, Hokkaido University, for his helpful and valuable suggestions with continuous encouragement throughout this study.

The author also would like to express his sincere thanks to Associate Professor Kenji Tajima and Associate Professor Takuya Yamamoto, Division of Applied Chemistry, Faculty of Engineering, Hokkaido University, and Dr. Redouane Borsali, Centre de Recherchers sur les Macromolécules Végétales, Centre National de la Recherche Scientifique (CERMAV-CNRS), whose kind understanding and generous supports have been indispensable throughout this work.

The author is particularly indebted to Professor Hajime Ito, Division of Applied Chemistry, Faculty of Engineering, Hokkaido University, for his assistance with the AFM experiments; Dr. Hiroaki Mamiya, Quantum Beam Unit, Advanced Key Technologies Division, National Institute for Materials Science, for his assistance with the SAXS experiments; and Mr. Ken Miyagi, Next Generation Material Development Division Research & Development Department, Tokyo Ohka Kogyo Co., Ltd., for his useful support with thin film experiments.

The author is grateful to thank Mr. Lin Tian and other members of Professor Satoh's group for their good collaborations and for providing a good working atmosphere.

This work was supported by Research Fellowship of Japan Society for the Promotion of Science (JSPS) for Young Scientists and Ministry of Education, Culture, Sports, Science and Technology (MEXT) program for Leading Graduate Schools (Hokkaido University "Ambitious Leader's Program").

March 2019

Kohei Yoshida

# Contents

# *Chapter 1*

## *General Introduction*

## 1.1 Microphase separation

### *1.1.1 Nanofabrication using Block Copolymer*

Block copolymers (BCPs) consisting of two or more chemically-distinct polymer chains (blocks) spontaneously self-assemble to form a variety of nanoscale periodic structures when the constituent blocks have a sufficient incompatibility to separate from each other.[1] This self-assembly behavior, the so-called microphase separation, is driven by the demixing of the blocks into different phases referred to as the microdomain and matrix. Since the periodic length of the microphase-separated structures typically ranges from 5 to 50 nm and is controllable by the molecular weight adjustment, the BCP self-assembly has attracted much attention as a promising platform for the "bottom-up" nanotechnologies. Starting from microphase-separated BCPs in the bulk and thin film states, a variety of functional nanomaterials, such as nanoporous materials, electronic devices, and patterned inorganic materials, are fabricated by the processes shown in Figure 1.1.[2–6] For example, Chen and coworkers prepared highly stretchable memory devices using the saccharide-containing BCP systems and found that the memory-type behaviors can be tuned by the morphologies of the microphase-separated structures.[7] Zhao and coworkers demonstrated the reproducible synthesis of highly-ordered mesoporous polymers and carbons from the composite of the poly(ethylene oxide)-*b*-poly(propylene oxide)-*b*-poly(ethylene oxide) triblock copolymers with the low-molecular-weight phenolic resin precursors.[8] Several researchers reported that the nanoporous polymer films generated by the selective removal of the microdomains are expected to be used as nanotemplates to fabricate the patterned organic/inorganic nanoarrays and filtration membranes to remove specific molecules.[9–16] Importantly, the BCP nanolithography that transfers the nanopattern from the nanoporous thin film to the underlayer is expected to be an innovative technique to fabricate a circuit pattern with a small feature size unachievable by the existing photolithography (>43 nm resolution by ArF excimer laser).[17–25] For further development of such next-generation nanotechnologies, the fine-tuning of the morphologies and minimization of the periodic length of the microphase separation are the most important and challenging issues in this field.

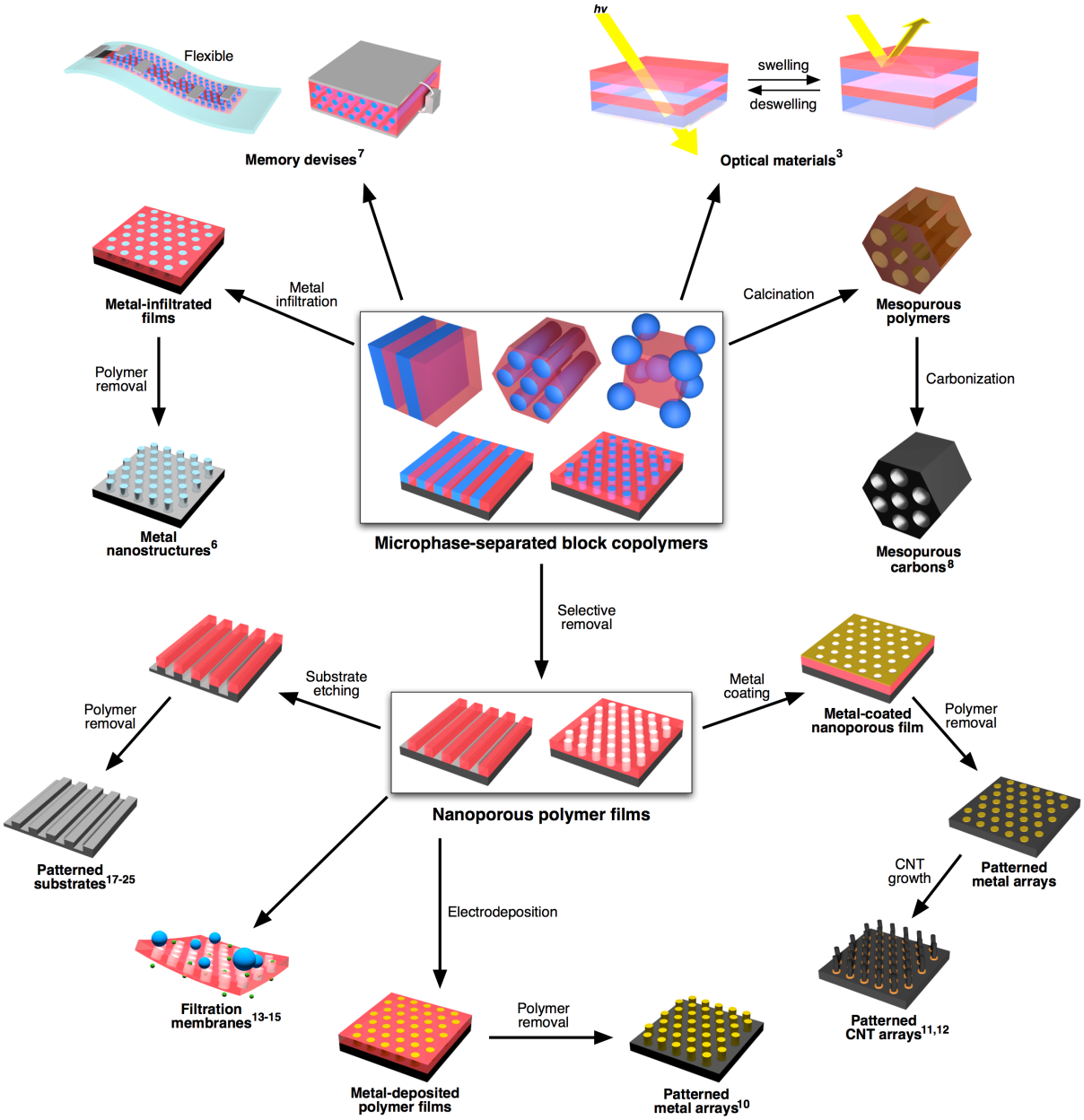


**Figure 1.1**. Next-generation nanotechnologies using BCP self-assembly for a wide range of applications.

### *1.1.2 Theory of Microphase Separation Behavior*

When a BCP system has a sufficient incompatibility between the blocks, the polymer chains are arranged to minimize the interface area between the domains at equilibrium, as shown in Figure 1.2a (Note that only amorphous BCPs are considered in this section).[1,5,26] Thus, the morphology of the microphase-separated structures depends on the volume fraction ($f$) of the constituent blocks, and the increase in the $f$ of one block causes the continuous morphological changes from a body-centered cubic sphere structure (BCC) through a hexagonally close-packed cylinder (HEX), bicontinuous gyroid (GYR), and lamella (LAM), as shown in Figure 1.2b. The volume fraction of a diblock copolymer is described as

$$f_A = 1 - f_B = \frac{\nu_A}{\nu_A + \nu_B}$$

where $v$ is the molar volume of the blocks while the subscripts A and B represent the constituent blocks.

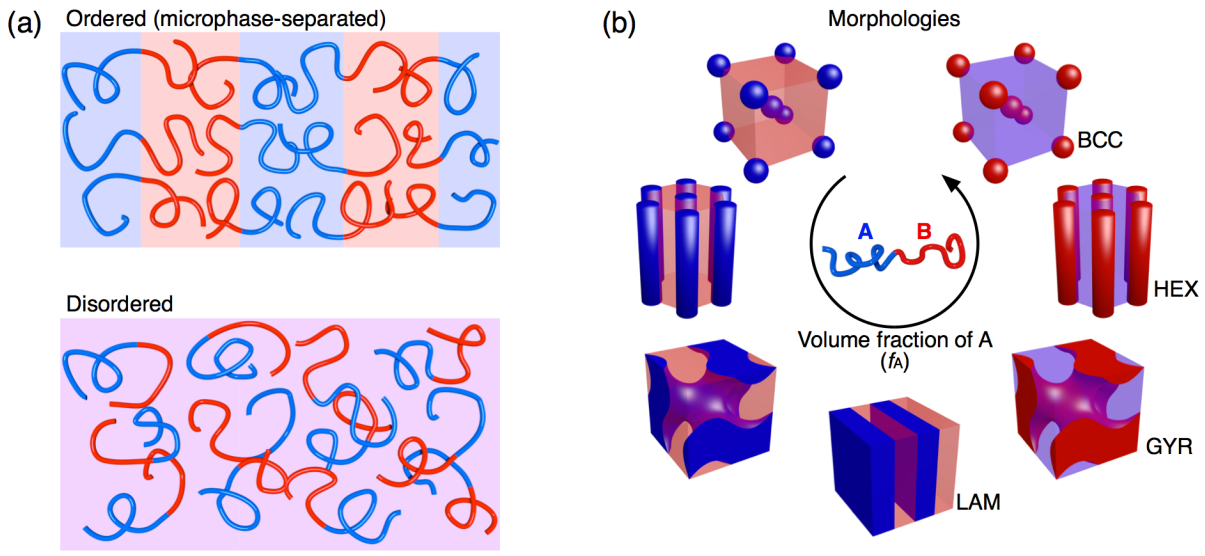


**Figure1.2**. (a) Schematic illustration of symmetric BCP chains in the ordered (upper) and disordered states (lower). (b) The morphologies of the microphase-separated structures of diblock copolymers at equilibrium in a strong segregation limit (SSL).

The BCP phase behavior is governed by several factors, such as the *f* of the constituent polymers, incompatibility between the blocks characterized by the Flory-Huggins interaction parameter ($\chi$), overall degree of polymerization ($N$), macromolecular architecture, and conformational asymmetry. The $\chi$ is generally expressed as a function of the temperature by the following equation:

$$\chi = \frac{A}{T} + B$$

where A and B are experimentally obtained constants for the block pair. Unlike the chemical degree of polymerization, $N$ is described as

$$N = \frac{M}{\nu_0 \rho N_A}$$

where $M$, $v_0$, $\rho$, and $N_A$ are the number-averaged molecular weight, reference volume of the monomer, polymer density, and the Avogadro constant, respectively. Based on the "$\chi N$" value, the phase behavior of the BCPs is classified into two segregation limits. In the $\chi N << 1$ region, the BCP chains are homogeneously dispersed to have apparent volumes similar to the polymer radius of gyration ($R_g$) due to the insufficient incompatibility to separate the blocks from each other, leading to a disordered state.[27,28] With the increasing $\chi N$ to *ca.* 10, the disorder-to-order transition occurs and each polymer block weakly segregates to form microdomains. Such a phase-behavior limit in the $\chi N < 10$ is referred to as the "weak segregation limit (WSL)" and the periodic length, termed the domain spacing ($d$), is a function of $N^{1/2}$ in this region, as follows:

$$d \sim R_g \sim aN^{\frac{1}{2}} \quad (\chi < 10)$$

where $a$ is the characteristic segment length of the repeating unit in the copolymer. The $a$ of a copolymer is given as follows:

$$a = \sqrt{\frac{f_A}{{a_A}^2} + \frac{f_B}{{a_B}^2}}$$

In the $\chi N >> 10$ region, the two blocks in a BCP system significantly separated from each other form well-ordered microphase-separated structures. This phase-behavior limit is called the "strong segregation limit (SSL)" and the $d$ value is a function of $\chi^{1/6}$ and $N^{2/3}$as described by

$$d \sim a\chi^{\frac{1}{6}}N^{\frac{2}{3}} \quad (\chi \gg 10)$$

The self-consistent mean field (SCMF) theory was developed to combine the two described segregation limits, which gives the phase diagram to predict the phase behavior of linear diblock copolymers as shown in Figure 1.3.[29,30] Importantly, the SCMF theory predicts the boundary between the ordered and disordered states, *i.e.*, boundary line of the order-to-disorder transition (ODT) or disorder-to-order transition. With the increasing temperature, the ordered BCP undergoes the order-to-disorder transition at the critical temperature ($T_{ODT}$) because the $\chi$ value decreases with the increasing temperature. The critical $\chi N$ value of a symmetric diblock copolymer ($f_A$ = 0.50) at $T_{ODT}$ is predicted to be 10.495 according to the phase diagram, suggesting that $\chi N$ must be >10.495 to induce microphase separation. Considering that the $d$ value is directly proportional to $\chi^{1/6}N^{2/3}$, the decrease in $N$ is a reasonable approach to reduce the $d$ while a large $\chi$ is required to achieve microphase separation at a given small $N$.

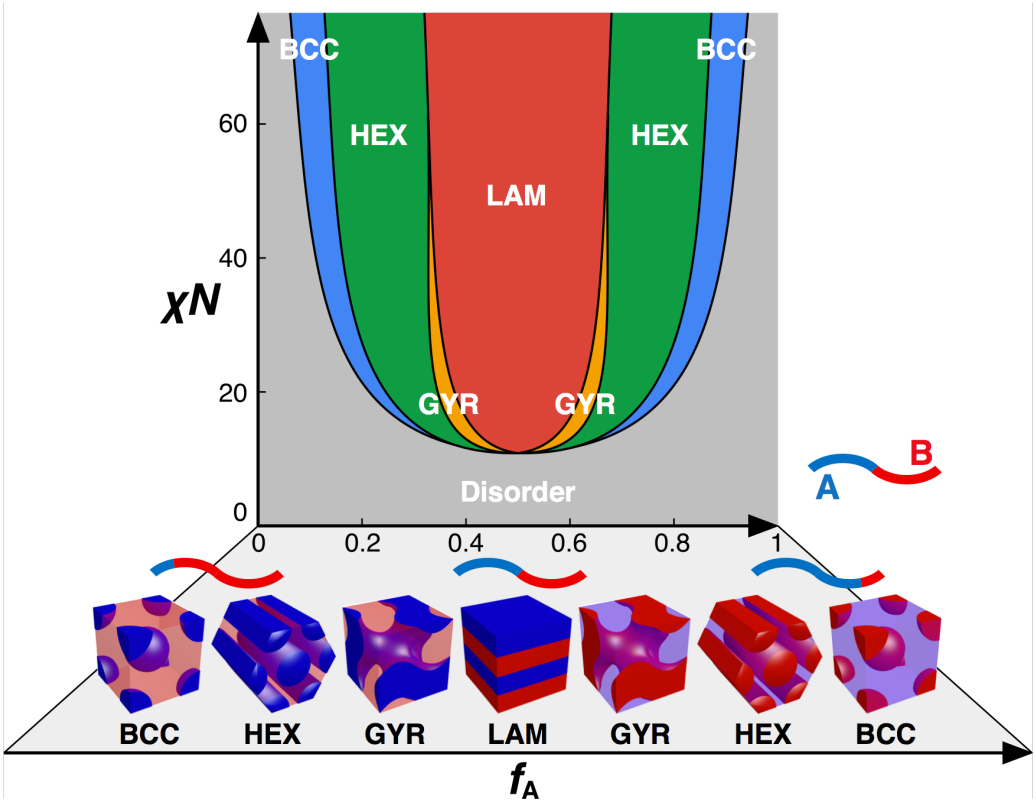


**Figure 1.3**. Theoretical phase diagram of linear-type coil-coil diblock copolymers based on SCMF theory.

### *1.1.3 High-χ Block Copolymer*

In the past decade, a number of high-$\chi$ BCPs has been designed for producing microphase separation with an extremely low *d* value (<20 nm) unachievable by conventional low-$\chi$ BCPs like polystyrene-*block*-polyisoprene (PS-*b*-PI) and polystyrene-*block*-poly(methyl methacrylate) (PS-*b*-PMMA).[31–39] The high-$\chi$ BCPs generally consist of a specific combination of hydrophobic blocks (e.g., polydimethylsiloxane, poly(cyclohexylethylene), and poly(4-*tert*-butylstyrene)) with highly polar blocks (e.g., polylactide, poly(hydroxystyrene), and poly(4-vinylpyridine)) (Chart 1.1). Hillmyer and Bates groups found that poly(cyclohexylethylene)-*block*-poly(methyl methacrylate) possesses a significantly higher $\chi$ value than that of PS-*b*-PMMA.[40] This BCP system formed lamellar structures with the extremely low *d* value of ~10 nm, which corresponds to an ~5 nm feature size (Note that the feature size is defined as the width of one microdomain (i.e., half-pitch) while the *d* corresponds to one full periodic length in the case of a lamellar structure). Kim and coworkers reported extremely small microphase-separated structures with a sub-3 nm feature size from the poly(3,4-dihydroxystyrene)-*block*-polystyrene system.[41] Alternatively, several research groups employed the highly hydrophobic or hydrophilic oligomeric segments as building blocks to produce the high-$\chi$ polymer systems. For example, the Meijer group prepared the monodisperse oligo(dimethylsiloxane)-*block*-oligo(lactide), which formed the microphase-separated structures with a sub-5 nm feature size.[42] Hayakawa and several groups designed the polyhedral oligomeric silsesquioxanes (POSS)-containing polymers to produce a high-$\chi$ character.[43–47] Kakuchi and Borsali groups prepared the sugar-based BCP systems to produce sub-10 nm-scale microphase-separated structures.[48–51] Although these polymer designs rely on the highly incompatible blocks to realize the size reduction of the microphase-separated structures, such polymer systems generally suffer from industrial issues including low productivity, high cost due to the difficul synthesis, and poor accessibility of the monomers. Therefore, a simple and efficient strategy to produce high-$\chi$ BCPs from readily available starting materials is required for further development of nanofabrication technologies.

**Chart 1.1**. High-$\chi$ BCPs that form sub-10 nm-scale microphase-separated structures

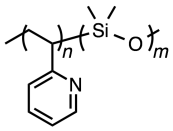

poly(2-vinylpyridine)-*block*-polydimethylsiloxane
(P2VP-*b*-PDMS)[37]

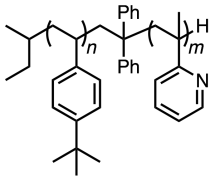

poly(4-*tert*-butylstyrene)-*block*-poly(2-vinylpyridine)
(PtBSt-*b*-P2VP)[38]

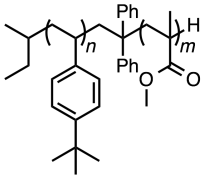

poly(4-*tert*-butylstyrene)-*block*-poly(methyl methacrylate)
(PtBSt-*b*-PMMA)[39]

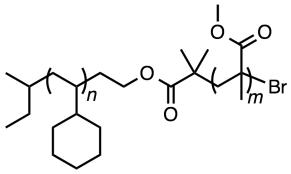

poly(cyclohexylethylene)-*block*-poly(methyl methacrylate)
(PCHE-*b*-PMMA)[40]

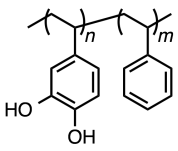

poly(3,4-dihydroxystyrene)-*block*-polystyrene
(PDHS-*b*-PS)[41]

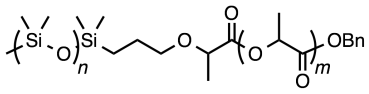

oligodimethylsiloxane-*block*-oligolactide
(ODMS-*b*-OLA)[42]

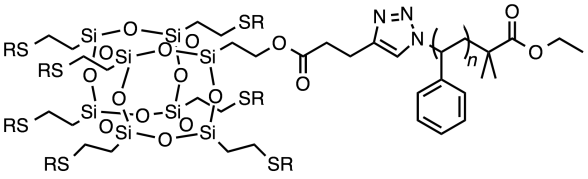

polyhedral oligomeric silsesquioxane-*block*-polystyrene
(POSS-*b*-PS)[47]

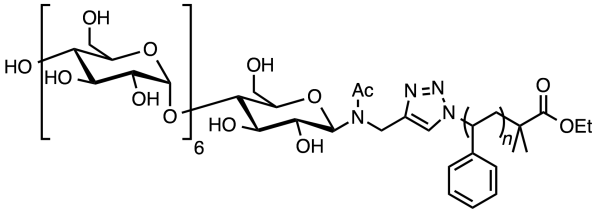

maltoheptaose-*block*-polystyrene
(MH-*b*-PS)[51]

## 1.2 Postpolymerization Modification

Postpolymerization modification enables transforming a polymer into its various derivatives without any change in the *N* and dispersity from the original one.[52–54] In fact, the preparation of the high-$\chi$ BCPs using the postpolymerization modification strategies has been reported by several research groups, which can be classified into two major types; i.e., the pendant-group and chain-end modifications (Scheme 1.1).

**Scheme 1.1**. Postpolymerization modifications for controlling the microphase-separated structures using (a) poly(solketal methacrylate)-*block*-polystyrene,[55] (b) polystyrene-*block*-poly(vinyl azlactone),[56,57] (c) polystyrene-*block*-poly(methyl vinyl siloxane),[58] and (d) polystyrene-*block*-poly(ethylene oxide)[59] as the parent BCPs.

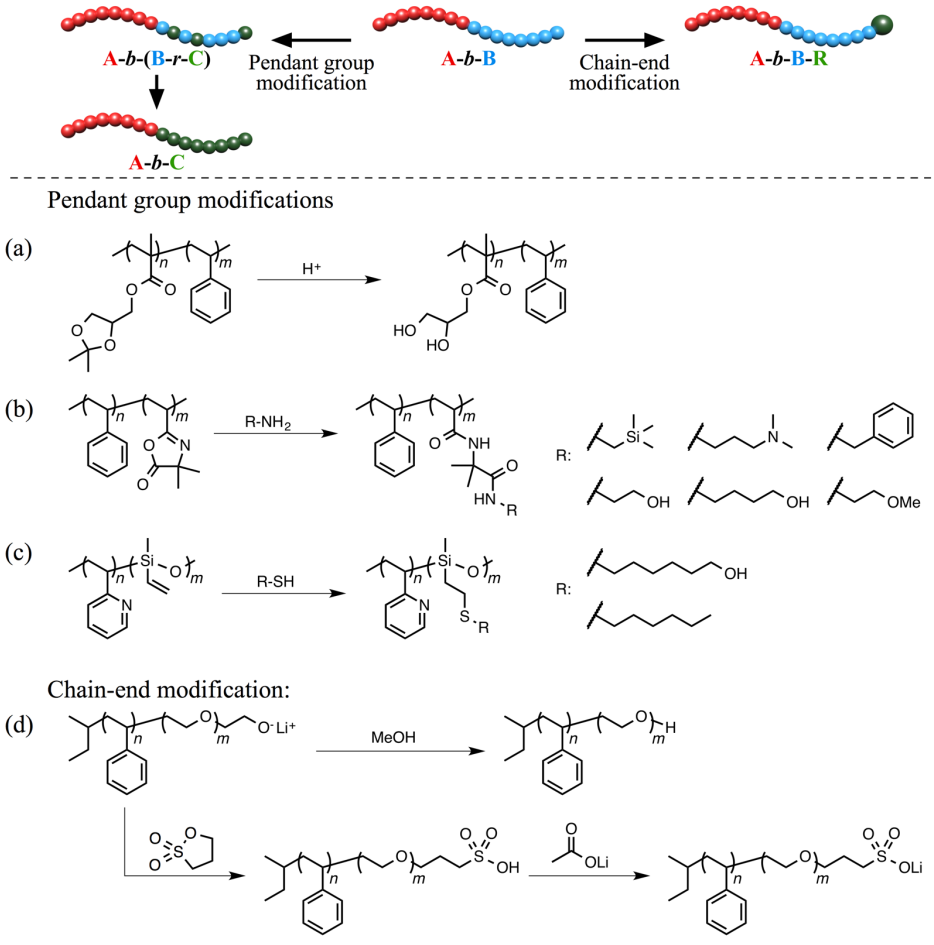

In the case of pendant-group-modification for a diblock copolymer (A-*b*-B), the repeating units of one block are partially or fully converted to yield A-*b*-(B-*r*-C) or A-*b*-C type BCPs, respectively, where A, B, and C are distinct components. When the segregation strength of A−C is sufficiently stronger than that of A−B, the $\chi$ values of the A-*b*-(B-*r*-C) and A-*b*-C are higher than that of the A-*b*-B. Importantly, for the A-*b*-(B-*r*-C), the incompatibility between the blocks is easily controllable by changing the composition of the comonomer (C). Thus, the A-*b*-(B-*r*-C) type BCPs are suitable materials to obtain small microphase-separated structures and to control the morphologies while keeping the polymer backbone of the original BCP. Russell showed the simple chemical transformation from poly(solketal methacrylate)-*block*-polystyrene to poly(glycerol monomethacrylate)-*block*-polystyrene to enhance the effective interaction parameter ($\chi_{eff}$), enabling the microphase separation (Scheme 1.1a).[55] In addition, they demonstrated the fine-tuning of $\chi_{eff}$ by simply adjusting the conversion of the solketal. Mahanthappa and coworkers designed a new BCP system consisting of polystyrene and poly(vinyl azlactone), which undergoes selective and quantitative reactions with functional primary amines, to yield the corresponding PS-*b*-poly(acrylamide)s (Scheme 1.1b).[56,57] The $\chi_{eff}$ value of the BCP clearly increased after the conversion from poly(vinyl azlactone) to poly(acrylamide), thereby leading to the microphase separation even at a low *N*. Importantly, the $\chi_{eff}$ can be controlled by changing the functional amines. Hayakawa also developed the postpolymerization modification of polysiloxane-based BCPs by the thiol-ene reaction to control $\chi_{eff}$ (Scheme 1.1c).[58]

Recently, several studies about the chain-end modification for controlling the BCP morphologies have been reported. Park et al. demonstrated a simple way of tuning the microphase-separated structures generated from polystyrene-*block*-poly(ethylene oxide) (PS-*b*-PEO) by modification of the PEO chain-end structure (Scheme 1.1d).[59,60] For example, PS-*b*-PEO bearing sulfonic acid groups at the PEO chain end formed a lamellar nanostructure, while the unmodified PS-*b*-PEO with a terminal hydroxyl group was less ordered, demonstrating that the block incompatibility can be controlled by the end groups. In addition, the morphology transition was clearly observed from the lamellar to cylindrical phase as the end group was changed from sulfonic acid to lithium sulfonate.

These pioneering studies suggested that modifications of the pendant-group and chain-end structures enable the enhancements in $\chi$ and fine-tuning of the BCP morphology. However, the preparation

of such BCP systems capable of postpolymerization modifications generally includes a complicated synthetic route to produce a sufficient reactivity, resulting in a poor accessibility. Thus, the development of a postpolymerization method using classical BCPs, which are composed of commercially-available monomers and prepared by a conventional polymerization process, is of great interest for controlling the morphologies. In particular, the facile and effective transformation from the commercially-available low-$\chi$ BCPs to high-$\chi$ BCPs is expected as a practical approach to realize the downsizing of the microphase-separated structure.

## 1.3 Polystyrene-*block*-poly(methyl methacrylate)

Polystyrene-*block*-poly(methyl methacrylate) (PS-*b*-PMMA), one of the classical BCPs, is a leading candidate for the BCP nanofabrication because of its practical advantages, such as the commercial availability of its monomers; its synthetic accessibility; and the fact that it can be mass produced on a pilot scale.[61−63] In fact, there have been a number of fundamental studies about the nanofabrication using PS-*b*-PMMA as a template.[11,12,14−16,64,65] In addition, PS-*b*-PMMA is the current industry standard as a nanotemplate for the BCP lithography process because of the following characteristics: the comparable surface energies between the PS and PMMA blocks enables the perpendicular orientation of the microdomains to the substrate by a simple thermal annealing;[66] and the sufficient difference in etch rate between the blocks leads to the selective removal of the PMMA component from the thin film by dry etching.[67,68] These remarkable characteristics of PS-*b*-PMMA are important requirements for the pattern transfer to the substrate during the BCP lithography process. Nealey and co-workers demonstrated the pattern-transfer strategy from the microphase-separated PS-*b*-PMMA thin film to the underlying silicon substrate (Figure 1.4).[68] The thin film of PS-*b*-PMMA spun-coated onto the silicon substrate was thermally annealed to form a microphase-separated structure. The PMMA domains in the thin film were selectively removed by the reactive ion etching with oxygen or argon plasmas as the chemical and physical etching gasses, respectively, to fabricate a PS nanopattern as a lithographic template. The PS nanopattern was then transferred to the underlaying silicon substrate by dry etching using $C_2H_2F_4/SF_6$ plasma followed by the PS removal. So far, significant efforts have been made to the BCP lithography based on PS-*b*-PMMA, providing a deeper understanding of BCP thin film physics, material design, and processing.[68−73] However, the insufficient incompatibility between the PS and PMMA blocks is a major drawback of the PS-*b*-PMMA system, which prevents the system from having a microphase separation with a $d$ value of <20 nm.[71,74−76] Accordingly, the high-$\chi$ BCPs have been developed to fabricate a much smaller feature size, although the use of the new high-$\chi$ BCPs requires reoptimization of the lithographic processes for each system. Therefore, for further advancement of nanofabrications based on the BCP self-assembly, development of a slightly modified version of PS-*b*-PMMA that retains the original backbone is of great interest as it enables both achieving a high-$\chi$ character and applying it to the established standard nanofabrication process.

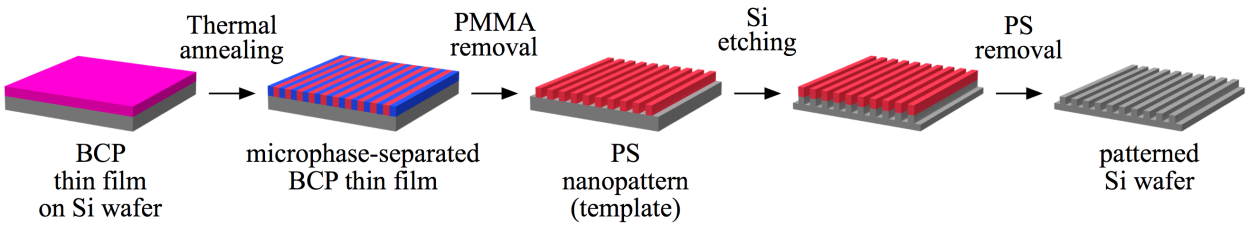


**Figure 1.4**. Schematic illustration of the BCP lithography process.

PS-*b*-PMMA can be synthesized by sequential monomer addition via the living/controlled radical polymerization (LCRP) including nitroxide-mediated polymerization (NMP), reversible addition-fragmentation chain transfer (RAFT) polymerization, and atom transfer radical polymerization (ATRP) and living anionic polymerization (Scheme 1.2).[77–84] The LCRPs have been widely used as facile and efficient techniques to synthesize vinyl polymers with controlled molecular weights because of the simple experimental procedure, broad range of applicable monomers and solvents, and commercial availability of the initiators and catalysts.[85–87] In addition, the suitable design of the initiator and postpolymerization reaction lead to the production of the functional polymers having a mono- or bi- functional group at the chain ends. For the polymer synthesis by LCRPs, particularly for the BCPs, however, the dispersity tends to be broader due to the unstable nature of the active propagating species during the polymerization. The broad dispersity often causes the disordering in the low-$N$ and even high-$\chi$ regions.[88] Furthermore, in the synthesis of BCP by LCRP, the purification processes are required after each polymerization to remove the unreacted monomers, resulting in a time-consuming process and decrease in the product yield.

**Scheme 1.2.** Synthesis of PS-*b*-PMMA by living/controlled radical polymerizations.

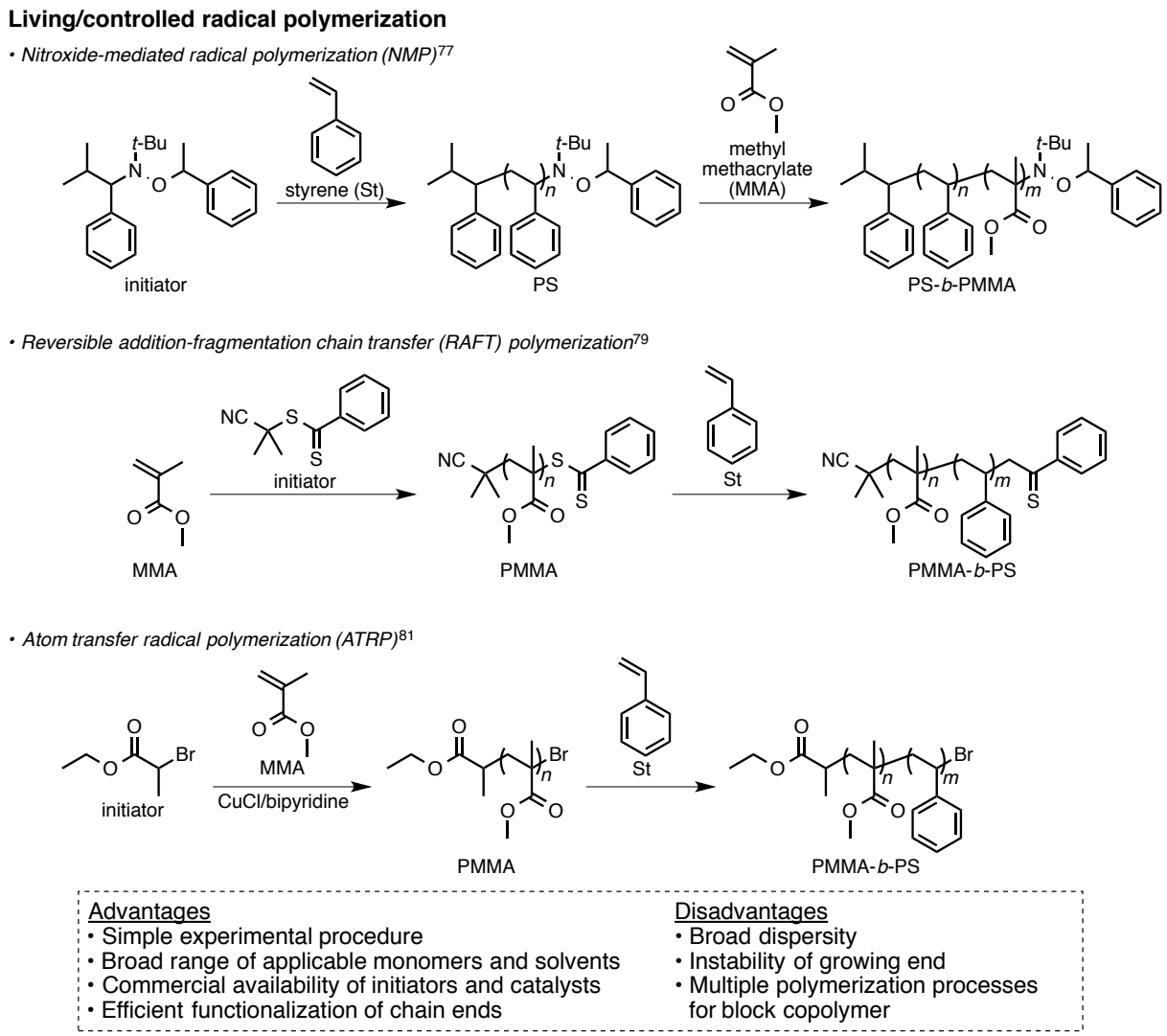


In contrast, the anionic polymerization technique provides PS-*b*-PMMAs with an extremely narrow dispersity of *ca.* 1.02 with well-defined structures in a one-pot process due to the excellent livingness, indicating its suitability for the synthesis of PS-*b*-PMMAs for the systematic investigation of microphase-separation behaviors (Scheme 1.3).[89] The fact that the synthesis of PS-*b*-PMMA via anionic polymerization has been achieved on a pilot scale demonstrates its feasibility of mass production on an industrial scale.[90,91] However, anionic polymerization suffers from a narrow range of applicable reagents including the monomer,

initiator, and solvent, due to the high sensitivity of the growing chain end, which sometimes cause difficulty in the optimization of the synthesis condition and process when the polymer designs, such as chain-end structure and comonomer compositions, were changed. Therefore, the postpolymerization modification approach should be a suitable strategy to make a series of modified PS-*b*-PMMA systems for the systematic investigations of the microphase-separation behavior. Whereas the postpolymerization modifications of the PS and PMMA homopolymers have been well studied, direct postpolymerization modification of the PS-*b*-PMMA for the fine-tuning and reduction of the microphase separated structure is still lacking.

**Scheme 1.3**. Synthesis of PS-*b*-PMMA by living anionic polymerization.[89]

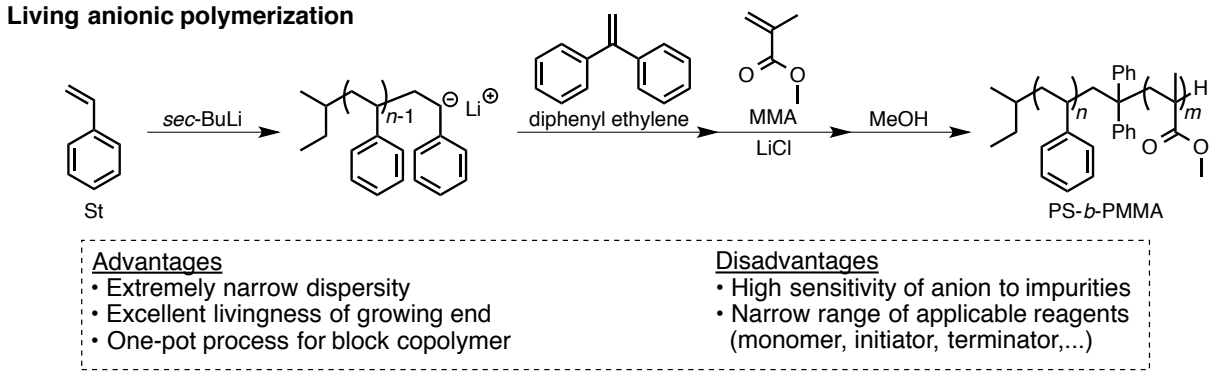

## 1.4 Objective and Outline of the Dissertation

The nanofabrication techniques using the BCP microphase separation is a promising strategy as a "bottom-up" fabrication for producing functional nanomaterials, such as nanopatterned materials, nanoporous materials, and flexible devices, as mentioned in Section 1.1. In particular, the next-generation lithography technique using the microphase-separated BCP thin film as the template has attracted much attention to achieve a higher resolution than that achievable by the conventional photolithography process. The morphological control and reduction of the feature size in the microphase separation is of significant importance toward further development of these practical applications. The combination of the enhancement in $\chi$ and reduction in $N$ is the most reasonable and widely accepted strategy to reduce the size of the microphase separation because its feature size mainly depends on the $N$ while the BCP undergoes disordering in the low $\chi N$ region. As described in Section 1.2, although the postpolymerization modification strategy has been expected as a facile method to produce high-$\chi$/low-$N$ BCPs, the synthetic process is usually complicated because highly-reactive sites must be incorporated into the parent BCPs. Therefore, this dissertation is directed toward the development of a facile and efficient postpolymerization modification for the classical BCP, which is composed of common monomers and synthesized by a conventional polymerization process, to endow it with a high $\chi$ character, leading to extremely small microphase-separated structures. PS-*b*-PMMA is one of the classical BCPs having many practical advantages and used for the BCP lithography as the current industry standard of nanotemplate material as mentioned in Section 1.3. However, the weak incompatibility between the blocks of PS-*b*-PMMA makes it difficult to microphase-separate at a molecular weight of <30 kg mol$^{-1}$, thereby leading to the lower limit of the $d$ value of *ca.* 20 nm. Increasing the $\chi$ value of PS-*b*-PMMA by a slight chemical modification at a low $N$ would allow forming small microphase-separated structures while keeping the original polymer backbone. This strategy enables the modified PS-*b*-PMMAs to form extremely small nanopatterns by the established nanofabrication techniques that is optimized for PS-*b*-PMMA, leading to further development of the next-generation bottom-up nanotechnology. For this contribution, therefore, the author aimed to establish facile postpolymerization modifications of PS-*b*-PMMA to induce the microphase separation even in the low $N$ region and to fabricate sub-20-nm-scale nanostructures by the modified PS-*b*-PMMA. Specifically, the author proposes the "pendant group" and "chain-end"

modifications of PS-*b*-PMMA as facile and efficient methods for realizing the fine-tuning of the size and morphology of the microphase separation. These developments should provide a significant insight into the suitable modification techniques of PS-*b*-PMMA and great benefits in the nanotechnology field.

An outline of this dissertation is as follows:

Chapter 2 describes the simple and efficient method for the postpolymerization modification of PS-*b*-PMMA to effectively increase the incompatibility between the two blocks, so that microphase separation can be achieved even at a low degree of polymerization (Figure 1.5). The ester–amide exchange reactions of PS-*b*-PMMA with primary and secondary amines were performed to introduce a small number of methacrylamides into the PMMA block to increase its hydrophilicity. The results of small-angle X-ray scattering measurements performed on the bulk samples showed that the modified PS-*b*-PMMA self-assembled to form a lamellar phase even at the extremely low molecular weight of 8.5 kg mol$^{-1}$ due to the increased incompatibility between the blocks. The smallest domain spacing of the modified PS-*b*-PMMA observed in this chapter was 11.1 nm. That is to say, the smallest feature size was 5.6 nm. The modified PS-*b*-PMMA thin film created well-aligned line patterns by the combination with the graphoepitaxy directed self-assembly process, demonstrating that these materials obtained from PS-*b*-PMMA have the potential to be used for sub-10 nm nanofabrication applications.

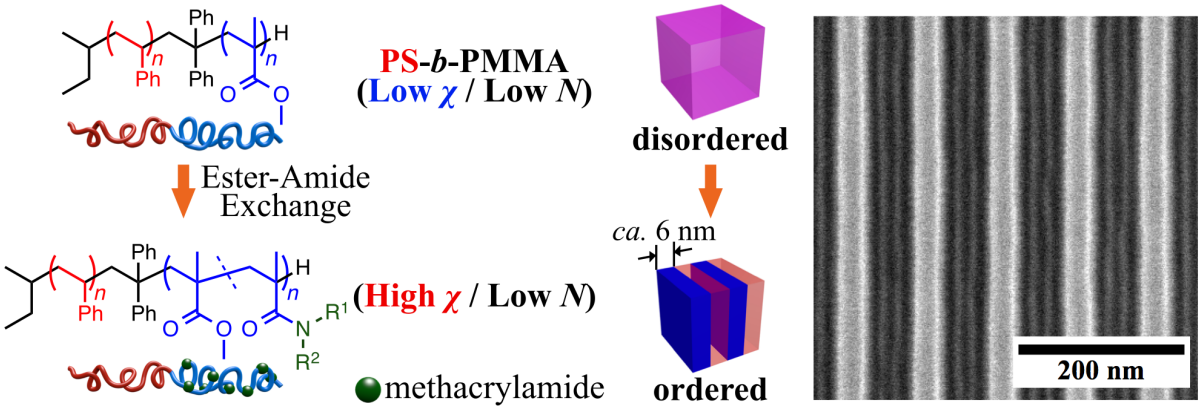


**Figure 1.5**. Schematic representation of the ester-amide exchange reaction of PS-*b*-PMMA for increasing the incompatibility between the PS and PMMA blocks.

Chapter 3 describes the development of the chain-end modification by the terminal-selective transesterification of PMMA and PS-*b*-PMMA (Figure 1.6). Starting from the anionically-synthesized PMMA and PS-*b*-PMMA, the ester side chains of the MMA units at the *ω*-chain end were selectively transesterified in the presence of various alcohols with the aid of the corresponding titanium alkoxides to yield the end-functionalized PMMAs and PS-*b*-PMMAs. The wide range of alcohols having various functional groups, such as an alkyl chain, aromatic ring, and fluorocarbon chain, were applicable for the terminal-selective transesterification. The azido-functionalized alcohol was also successfully incorporated into the ester side chain of the *ω*-terminal MMA unit, leading to the further functionalization by the click reaction with ethynyl-functionalized compounds. Importantly, even hydroxy-functionalized polymers, i.e., the poly(ethylene glycol) monomethyl ether, as well as oligo(ethylene glycol) monomethyl ether, can be used for the terminal-selective transesterification of PS-*b*-PMMA to yield triblock terpolymers. The present transesterification system can be a powerful tool for the chain-end functionalization of the apparently inactive chain-ends of PMMA and PS-*b*-PMMA, enabling the systematic investigation to extract the pure effect of the chain-end structure on the microphase-separation behaviors.

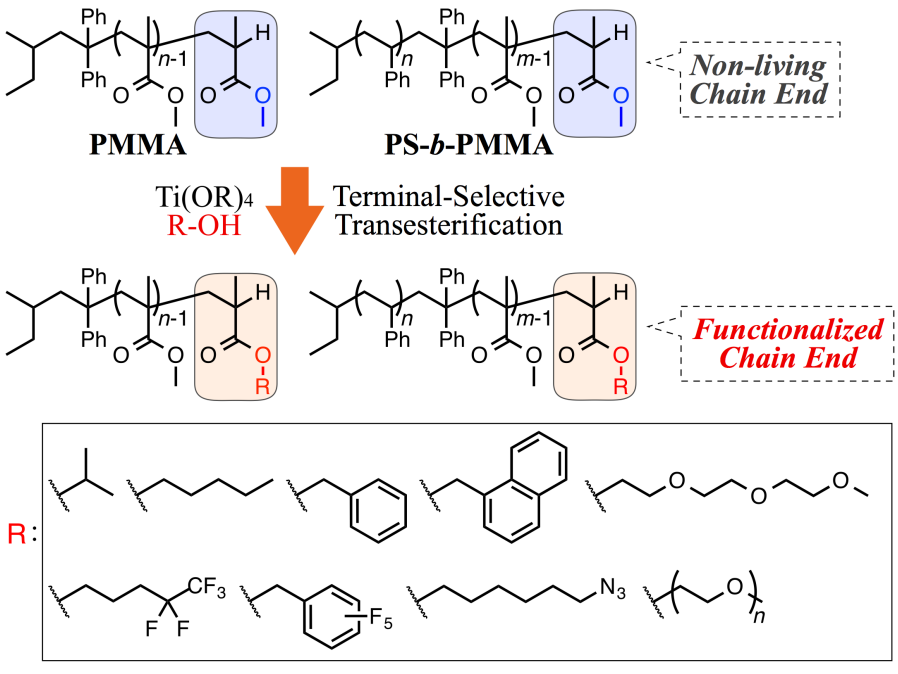


**Figure 1.6**. Schematic representation of the terminal-selective transesterification of PMMA and PS-*b*-PMMA.

Chapter 4 describes the preparation of well-defined PS-*b*-PMMAs bearing highly hydrophilic mono/oligosaccharide moieties at their PMMA chain ends and demonstrates the impact of the mono/oligosaccharide on the microphase-separation behavior (Figure 1.7). The PS-*b*-PMMAs were terminal-selectively transesterified using the titanium alkoxide of 6-azido-1-hexanol to incorporate an azido group into the side chain of the terminal MMA unit. The azido-functionalized PS-*b*-PMMAs were subsequently reacted with ethynyl-functionalized mono/oligosaccharides via click chemistry to incorporate a saccharide segment into the *ω*-chain end. Small-angle X-ray scattering and microscopy experiments revealed that PS-*b*-PMMAs bearing maltotrioses at their chain ends, with total molecular weights of *ca.*10 kg mol$^{-1}$, successfully form microphase-separated structures, although the unmodified PS-*b*-PMMAs exist in miscible states. Interestingly, the maltotrioses-incorporated PS-*b*-PMMA with equivalent PS- and PMMA-MT-block volume fractions microphase-separated to form a hexagonally close-packed cylinder with a domain spacing of 11.5 nm, rather than a lamellar structure, implying that the phase diagram for microphase separation is significantly affected by the strong maltotriose aggregation. Hence, the results presented herein demonstrate that the incorporation of oligosaccharide moieties at chain ends is an efficient means of fine-tuning the size features as well as the morphologies of the BCP microphase-separated structures.

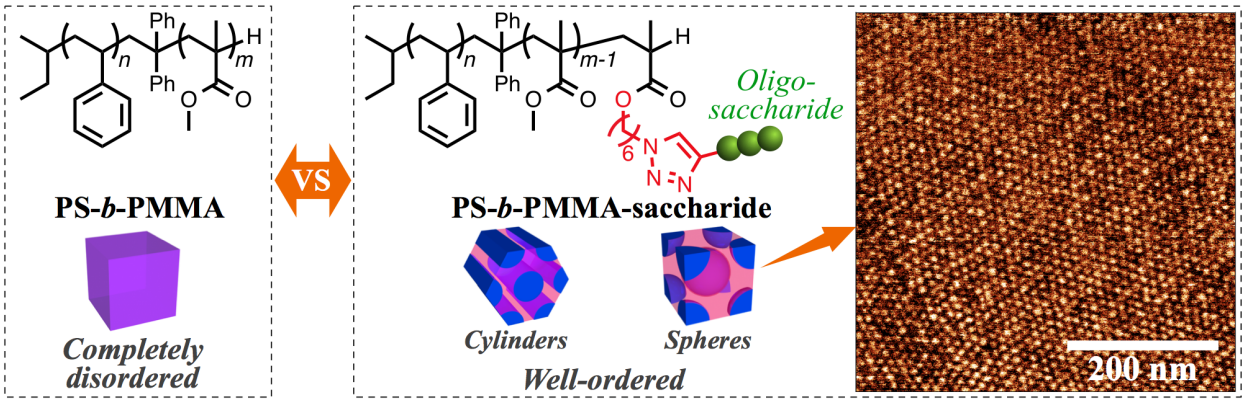


**Figure 1.7**. Schematic representation of the microphase-separation behavior of the classical PS-*b*-PMMA and saccharide-modified PS-*b*-PMMA.

The concluding Chapter 5 summarizes the methodology of the postpolymerization modification for the PS-*b*-PMMA and the microphase-separation behavior of the modified PS-*b*-PMMAs.

## 1.5 Reference

1. Bates, F. S. Block Copolymer Thermodynamics: Theory and Experiments. *Annu. Rev. Phys. Chem.* **1990**, *41*, 525−557.

2. Hamley, I. W. Nanostructure fabrication using block copolymers. *Nanotechnology* **2003**, *14*, R39–R54.

3. Kang, Y.; Walish, J. J.; Gorishnyy, T.; Thomas, E. L. Broad-wavelength-range chemically tunable block-copolymer photonic gels. *Nature Materials* **2007**, *6*, 957–960.

4. Hamley, I.W. Ordering in thin films of block copolymers: Fundamentals to potential applications. *Prog. Polym. Sci.* **2009**, *34*, 1161–1210.

5. Kim, H. C.; Park, S. M.; Hinsberg, W. D. Block Copolymer Based Nanostructures: Materials, Processes, and Applications to Electronics. *Chem. Rev.* **2010**, *110*, 146–177.

6. Tseng, C.; Peng, Q.; Ocola, L. E.; Elam, J. W.; Darling, S. B. Enhanced Block Copolymer Lithography Using Sequential Infiltration Synthesis. *J. Phys. Chem. C* **2011**, *115*, 17725–17729.

7. Hung, C.; Chiu, Y. C.; Wu, H. C.; Lu, C.; Bouilhac, C.; Otsuka, I.; Halila, S.; Borsali, R.; Tung, S. H.; Chen, W. C. Conception of Stretchable Resistive Memory Devices Based on Nanostructure-Controlled Carbohydrate-block-Polyisoprene Block Copolymers. *Adv. Funct. Mater.* **2017**, *27*, 1606161.

8. Meng, Y.; Gu; D.; Zhang, F.; Shi, Y.; Cheng, L.; Feng, D.; Wu, Z.; Chen, Z.; Wan, Y.; Stein, A.; Zhao, D. A family of highly ordered mesoporous polymer resin and carbon structures from organic–organic self-assembly. *Chem. Mater.* **2006**, *18*, 4447–4464.

9. Li, R. R.; Dapkus, P. D.; Thompson, M. E.; Jeong, W. G.; Harrison, C.; Chaikin, P. M.; Register, R. A.; Adamson, D. H. Dense arrays of ordered GaAs nanostructures by selective area growth on substrates patterned by block copolymer lithography. *Appl. Phys. Lett.* **2000**, *76*, 1689–1691.

10. Haupt, M.; Miller, S.; Glass, R.; Arnold, M.; Sauer, R.; Thonke, K.; Möller, M.; Spatz, J. P. Nanoporous Gold Films Created Using Templates Formed from Self-Assembled Structures of Inorganic–Block Copolymer Micelles. *Adv. Mater.* **2003**, *15*, 829–831.

11. Lee, D. Y.; Shin, D. O.; Lee, W. J.; Kim, S. O. Hierarchically Organized Carbon Nanotube Arrays from Self-Assembled Block Copolymer Nanotemplates. *Adv. Mater.* **2008**, *20*, 2480–2485.

12. Lee, D. Y.; Lee, W. J.; Kim, S. O. Vertical Single-Walled Carbon Nanotube Arrays via Block Copolymer Lithography. *Chem. Mater.* **2009**, *21*, 1368–1374.

13. Phillip, W. A.; Rzayev, J.; Hillmyer, M. A. Cussler, E. L. Gas and water liquid transport through nanoporous block copolymer membranes. *J. Membrane Sci.* **2006**, *286*, 144–152.

14. Yang, S. Y.; Ryu, I.; Kim, H. Y.; Kim, J. K.; Jang, S. K.; Russell, T. P. Nanoporous Membranes with Ultrahigh Selectivity and Flux for the Filtration of Viruses. *Adv. Mater.* **2006**, *18*, 709–712.

15. Yang, S. Y.; Park, J.; Yoon, J.; Ree, M.; Jang, S. K.; Kim, J. K. Virus Filtration Membranes Prepared from Nanoporous Block Copolymers with Good Dimensional Stability under High Pressures and Excellent Solvent Resistance. *Adv. Funct. Mater.* **2008**, *18*, 1371–1377.

16. Yang, S. Y.; Yang, J. A.; Kim, E. S.; Jeon, G.; Oh, E. J.; Choi, K. Y.; Hahn, S. K.; Kim, J. K. Single-File Diffusion of Protein Drugs through Cylindrical Nanochannels. *ACS Nano* **2010**, *4*, 3817–3822.

17. Park, M.; Harrison, C.; Chaikin, P. M.; Register, R. A.; Adamson, D. H. Block Copolymer Lithography: Periodic Arrays of ~1011 Holes in 1 Square Centimeter. *Science* **1997**, *276*, 1401–1404.

18. Stoykovich, M. P.; Kang, H.; Daoulas, K. C.; Liu, G.; Liu, C. C.; Pablo, J. J.; Müller, M.; Nealey, P. F. Directed Self-Assembly of Block Copolymers for Nanolithography: Fabrication of Isolated Features and Essential Integrated Circuit Geometries. *ACS Nano* **2007**, *1*, 168–175.

19. Jeong, J. W.; Park, W. I.; Do, L. M.; Park, J. H.; Kim, T. H.; Chae, G.; Jung, Y. S. Nanotransfer Printing with sub-10 nm Resolution Realized using Directed Self-Assembly. *Adv. Mater.* **2012**, *24*, 3526–3531.

20. Bang, J.; Jeong, U.; Ryu, D. Y.; Russell, T. P.; Hawker, C. J. Block Copolymer Nanolithography: Translation of Molecular Level Control to Nanoscale Patterns. *Adv. Mater.* **2009**, *21*, 4769–4792.

21. Gu, X.; Gunkel, I.; Russell, T. P. Pattern transfer using block copolymers. *Phil. Trans. R. Soc. A* **2013**, *371*, 20120306.

22. Koo, K.; Ahn, H.; Kim, S. W.; Ryu, D. Y; Russell, T. P. Directed self-assembly of block copolymers in the extreme: guiding microdomains from the small to the large. *Soft Matter* **2013**, *9*, 9059–9071.

23. Griffiths, R. A.; Williams, A.; Oakland, C.; Roberts, J.; Vijayaraghavan, A.; Thomson, T. Directed self-assembly of block copolymers for use in bit patterned media fabrication. *J. Phys. D: Appl. Phys.* **2013**, *46*, 503001.

24. Luo, M.; Epps, T. H. III Directed Block Copolymer Thin Film Self-Assembly: Emerging Trends in Nanopattern Fabrication. *Macromolecules* **2013**, *46*, 7567–7579.

25. Hu, H.; Gopinadhan, M.; Osuji, C. O. Directed self-assembly of block copolymers: a tutorial review of strategies for enabling nanotechnology with soft matter. *Soft Matter*, **2014**, *10*, 3867–3889.

26. Matsen, M. W. The standard Gaussian model for block copolymer melts. *J. Phys.: Condens. Matter* **2002**, *14***,** R21–R47.

27. Bates, F. S. Measurement of the Correlation Hole in Homogeneous Block Copolymer Melts. *Macromolecules* **1985**, 18, 525-528.

28. Nojima, S.; Kato, K.; Yamamoto, S.; Ashida, T. Crystallization of Block Copolymers. 1. Small-Angle X-ray Scattering Study of an ε-Caprolactone-Butadiene Diblock Copolymer. *Macromolecules* **1992**, 25, 2237-2242.

29. Helfand E. Theory of inhomogeneous polymers: Fundamentals of the Gaussian random-walk model. *J. Chem. Phys.* **1975**, *62*, 999–1005.

30. Helfand E. Block Copolymer Theory. III. Statistical Mechanics of the Microdomain Structure. *Macromolecules* **1975**, *8*, 552–556.

31. Sinturel, C.; Bates, F. S.; Hillmyer, M. A. High $\chi$−Low $N$ Block Polymers: How Far Can We Go? *ACS Macro Lett.* **2015**, *4*, 1044–1050.

32. Keen, I.; Yu, A.; Cheng, H.; Jack, K. S.; Nicholson, T. M.; Whittaker, A. K.; Blakey, I. Control of the Orientation of Symmetric Poly(styrene)-*block*- poly(D,L-lactide) Block Copolymers Using Statistical Copolymers of Dissimilar Composition. *Langmuir* **2012**, *28*, 15876−15888.

33. Yao, L.; Oquendo, L. E.; Schulze, M. W.; Lewis, R. M. III,; Gladfelter, W. L.; Hillmyer, M. A. Poly(cyclohexylethylene)-*block*-Poly(lactide) Oligomers for Ultrasmall Nanopatterning Using Atomic Layer Deposition. *ACS Appl. Mater. Interfaces* **2016**, *8*, 7431−7439.

34. Kanimozhi, C.; Kim, M.; Larson, S. R.; Choi, J. W.; Choo, Y.; Sweat, D. P.; Osuji, C. O.; Gopalan , P. Isomeric Effect Enabled Thermally Driven Self-Assembly of Hydroxystyrene-Based Block Copolymers. *ACS Macro Lett.* **2016**, *5*, 833−838.

35. Rodwogin, M. D. Spanjers, C. S.; Leighton, C.; Hillmyer, M. A. Polylactide−Poly(dimethylsiloxane)−Polylactide Triblock Copolymers as Multifunctional Materials for Nanolithographic Applications. *ACS Nano* **2010**, *4*, 725−732.

36. Luo, Y.; Montarnal, D.; Kim, S.; Shi, W.; Barteau, K. P.; Pester, C. W.; Hustad, P. D.; Christianson, M. D.; Fredrickson, G. H.; Kramer, E. J.; Hawker, C. J. Poly(dimethylsiloxane-*b*-methyl methacrylate): A Promising Candidate for Sub-10 nm Patterning. *Macromolecules* **2015**, *48*, 3422−3430.

37. Jeong, J. W.; Park, W. I; Kim, M.; Ross, C. A.; Jung, Y. S. Highly Tunable Self-Assembled Nanostructures from a Poly(2-vinylpyridine-*b*-dimethylsiloxane) Block Copolymer. *Nano Lett.* **2011**, *11*, 4095–4101.

38. Sweat, D. P.; Kim, M.; Larson, S. R.; Choi, J. W.; Choo, Y.; Osuji, C. O.; Gopalan, P. Rational Design of a Block Copolymer with a High Interaction Parameter. *Macromolecules* **2014**, *47*, 6687−6696.

39. Kennemur, J. G.; Hillmyer, M. A.; Bates, F. S. Synthesis, Thermodynamics, and Dynamics of Poly(4-*tert*-butylstyrene-*b*-methyl methacrylate). *Macromolecules* **2012**, *45*, 7228−7236.

40. Kennemur, J. G.; Yao, L.; Bates, F. S.; Hillmyer, M. A. Sub-5 nm Domains in Ordered Poly(cyclohexylethylene)-*block*-poly(methyl methacrylate) Block Polymers for Lithography. *Macromolecules* **2014**, *47*, 1411−1418.

41. Kwak, J.; Mishra, A. K.; Lee, J.; Lee, K. S.; Choi, C.; Maiti, S.; Kim, M.; Kim, J. K. Fabrication of Sub-3 nm Feature Size Based on Block Copolymer Self-Assembly for Next-Generation Nanolithography. *Macromolecules* **2017**, *50*, 6813−6818.

42. Genabeek, B.; Waal, B. F. M.; Gosens, M. M. J.; Pitet, L. M.; Palmans, A. R. A.; Meijer, E. W. Synthesis and Self-Assembly of Discrete Dimethylsiloxane−Lactic Acid Diblock Co-oligomers: The Dononacontamer and Its Shorter Homologues. *J. Am. Chem. Soc.* **2016**, *138*, 4210−4218.

43. Ahn, B.; Hirai, T.; Jin, S.; Rho, Y.; Kim, K. W.; Kakimoto, M.; Gopalan, P.; Hayakawa, T.; Ree, M. Hierarchical Structure in Nanoscale Thin Films of a Poly(styrene-*b*-methacrylate grafted with POSS) ($PS_{214}$-*b*-$PMAPOSS_{27}$). *Macromolecules* **2010**, *43*, 10568–10581.

44. Tada, T.; Yoshida, H.; Ishida, Y.; Hirai, T.; Bosworth, J. K.; Dobisz, E.; Ruiz, R.; Takenaka, M.; Hayakawa, T.; Hasegawa, H. Directed Self-Assembly of POSS Containing Block Copolymer on Lithographically Defined Chemical Template with Morphology Control by Solvent Vapor. *Macromolecules* **2012**, *45*, 292−304.

45. Goseki, R.; Hirao, A.; Kakimoto, M.; Hayakawa, T. Cylindrical Nanostructure of Rigid-Rod POSS-Containing Polymethacrylate from a Star-Branched Block Copolymer. *ACS Macro Lett.* **2013**, *2*, 625−629.

46. Hirai, T.; Leolukman, M.; Liu, C. C.; Han, E.; Kim, Y. J.; Ishida, Y.; Hayakawa, T.; Kakimoto, M.; Nealey, P. F.; Gopalan, P. One-Step Direct-Patterning Template Utilizing Self-Assembly of POSS-Containing Block Copolymers. *Adv. Mater.* **2009**, *21*, 4334–4338.

47. Yue, K.; Liu, C.; Huang, M.; Huang, J.; Zhou, Z.; Wu, K.; Liu, H.; Lin, Z.; Shi, A. C.; Zhang, W. B.; Cheng, S. Z. D. Self-Assembled Structures of Giant Surfactants Exhibit a Remarkable Sensitivity on Chemical Compositions and Topologies for Tailoring Sub-10 nm Nanostructures. *Macromolecules* **2017**, *50*, 303−314.

48. Cushen, J. D.; Otsuka, I.; Bates, C. M.; Halila, S.; Fort, S.; Rochas, C.; Easley, J. A.; Rausch, E. L.; Thio, A.; Borsali, R.; Willson, C. G.; Ellison, C. J. Oligosaccharide/Silicon-Containing Block Copolymers with 5 nm Features for Lithographic Applications. *ASC Nano* **2012**, *6*, 3424−3433.

49. Isono, T.; Otsuka, I.; Kondo, Y.; Halila, S.; Fort, S.; Rochas, C.; Satoh, T.; Borsali, R.; Kakuchi , T. Sub-10 nm Nano-Organization in AB2- and AB3-Type Miktoarm Star Copolymers Consisting of Maltoheptaose and Polycaprolactone. *Macromolecules* **2013**, *46*, 1461−1469.

50. Isono, T.; Otsuka, I.; Suemasa, D.; Rochas, C.; Satoh, T.; Borsali, R.; Kakuchi , T. Synthesis, Self-Assembly, and Thermal Caramelization of Maltoheptaose-Conjugated Polycaprolactones Leading to Spherical, Cylindrical, and Lamellar Morphologies. *Macromolecules* **2013**, *46*, 8932−8940.

51. Otsuka, I.; Zhang, Y.; Isono, T.; Rochas, C.; Kakuchi, T.; Satoh, T.; Borsali, R. Sub-10 nm Scale Nanostructures in Self-Organized Linear Di- and Triblock Copolymers and Miktoarm Star Copolymers Consisting of Maltoheptaose and Polystyrene. *Macromolecules* **2015**, *48*, 1509−1517.

52. Boaen, N. K.; Hillmyer, M. A. Post-polymerization functionalization of polyolefins. *Chem. Soc. Rev.* **2005**, *34*, 267–275.

53. Gauthier, M. A.; Gibson, M. I.; Klok, H. Synthesis of Functional Polymers by Post-Polymerization Modification. *Angew. Chem. Int. Ed.* **2009**, *48*, 48–58.

54. Günay, K. A.; Theato, P.; Klok, H. Standing on the Shoulders of Hermann Staudinger: Post-polymerization Modification from Past to Present. *J. Polymer Science Part A: Polm. Chem.* **2013**, *51*, 1–28.

55. Yu, D. M.; Mapas, J. K. D.; Kim, H.; Choi, J.; Ribbe, A. E.; Rzayev, J.; Russell, T. P. Evaluation of the Interaction Parameter for Poly(solketal methacrylate)-*block*-polystyrene Copolymers. Macromolecules **2018**, *51*, 1031−1040.

56. Carter, M. C. D.; Jennings, J.; Speetjens, F. W., II; Lynn, D. M.; Mahanthappa, M. K. A Reactive Platform Approach for the Rapid Synthesis and Discovery of High $\chi$/Low $N$ Block Polymers. *Macromolecules* **2016**, *49*, 6268−6276.

57. Choi, J. W.; Carter, M. C. D.; Wei, W.; Kanimozi, C.; Speetjens, F. W., II; Mahanthappa, M. K.; Lynn, D. M.; Gopalan, P. Self- Assembly and Post-Fabrication Functionalization of Microphase Separated Thin Films of a Reactive Azlactone-Containing Block Copolymer. *Macromolecules* **2016**, *49*, 8177−8186.

58. Seshimo, T.; Maeda, R.; Odashima, R.; Takenaka, Y.; Kawana, D.; Ohmori, K.; Hayakawa, T. Perpendicularly oriented sub-10-nm block copolymer lamellae by atmospheric thermal annealing for one minute. *Sci. Rep.* **2016**, *6*, 19481−19488.

59. Jo, G.; Ahn, H.; Park, M. J. Simple Route for Tuning the Morphology and Conductivity of Polymer Electrolytes: One End Functional Group is Enough. *ACS Macro Lett.* **2013**, *2*, 990−995.

60. Jung, H. Y.; Mandal, P.; Jo, G.; Kim, O.; Kim, M.; Kwak, K.; Park, M. J. Modulating Ion Transport and Self-Assembly of Polymer Electrolytes via End-Group Chemistry. *Macromolecules* **2017**, *50*, 3224−3233.

61. Ahn, H.; Ryu, D. Y.; Kim, Y.; Kwon, K. W.; Lee, J.; Cho, J. Phase Behavior of Polystyrene-*b*-Poly(methyl methacrylate) Diblock Copolymer. *Macromolecules* **2009**, *42*, 7897−7902.

62. Tremblay, J.-F. AZ Readies for Chip Self-Assembly. *Chem. Eng. News* **2013**, *91*, 10.

63. Aimi, J.; Komura, M.; Iyoda, T.; Saeki, A.; Seki, S.; Takeuchi, M.; Nakanishi, T. Synthesis and Self-Assembly of Phthalocyanine-tethered Block Copolymers. *J. Mater. Chem. C* **2015**, *3*, 2484−2490.

64. Thurn-Albrecht, T.; Steiner, R.; DeRouchey, J.; Stafford, C. M.; Huang, E.; Bai, M.; Tuominen, M.; Hawker, C. J.; Russell, T. P. Nanoscopic Templates from Oriented Block Copolymer Films. *AdV. Mater.* **2000**, *12*, 787–791.

65. Melde, B. J.; Burkett, S. L.; Xu, T.; Goldbach, J. T.; Russell, T. P.; Hawker, C. J. Silica Nanostructures Templated by Oriented Block Copolymer Thin Films Using Pore-Filling and Selective-Mineralization Routes. *Chem. Mater.* **2005**, *17*, 4743–4749.

66. Mangipudi, V. S.; Huang, E.; Tirrell, M; Pocius, A. V. Measurement of Interfacial Adhesion Between Glassy Polymers Using the JKR Method. *Macromol. Symp.* **1996**, *102*, 131−143.

67. Asakawa, K.; Hiraoka, T.; Hieda, H.; Sakurai, M.; Kamata, Y.; Naito, K. Nano-Patterning for Patterned Media Using Block-Copolymer. *J. Photopolym. Sci. Technol.* **2002**, *15*, 465−470.

68. Liu, C.; Nealey, P. F.; Ting, Y.; Wendt, A. E. Pattern transfer using poly(styrene-*block*-methyl methacrylate) copolymer films and reactive ion etching. *J. Vac. Sci. Technol. B* **2007**, *25*, 1963−1968.

69. Kim, B. H.; Shin, D. O.; Jeong, S. J.; Koo, C. M.; Jeon, S. C.; Hwang, W. J.; Lee, S.; Lee, M. G.; Kim, S. O. Hierarchical Self-Assembly of Block Copolymers for Lithography-Free Nanopatterning. *Adv. Mater.* **2008**, *20*, 2303−2307.

70. Kim, B. H.; Lee, D. H.; Kim, J. Y.; Shin, D. O.; Jeong, H. Y.; Hong, S.; Yun, J. M.; Koo, C. M.; Lee, H.; Kim, S. O. Mussel-Inspired Block Copolymer Lithography for Low Surface Energy Materials of Teflon, Graphene, and Gold. *Adv. Mater.* **2011**, *23*, 5618−5622.

71. Wan, L.; Ruiz, R.; Gao, H.; Patel, K. C.; Albrecht, T. R.; Yin, J.; Kim, J.; Cao, Y.; Lin, G. The Limits of Lamellae-Forming PS-*b*-PMMA Block Copolymers for Lithography. *ACS Nano* **2015**, *9*, 7506−7514.

72. Kim, K.; Park, S.; Kim, Y.; Bang, J.; Park, C.; Ryu, D. Y. Optimized Solvent Vapor Annealing for Long-Range Perpendicular Lamellae in PS-*b*-PMMA Films. *Macromolecules* **2016**, *49*, 1722− 1730.

73. Jin, H. M.; Lee, S. H.; Kim, J. Y.; Son, S. W.; Kim, B. H.; Lee, H. K.; Mun, J. H.; Cha, S. K.; Kim, J. S.; Nealey, P. F.; Lee, K. J.; Kim, S. O. Laser Writing Block Copolymer Self-Assembly on Graphene Light-Absorbing Layer. *ACS Nano* **2016**, *10*, 3435−3442.

74. Russell, T. P.; Hjelm, R. P.; Seeger, P. A. Temperature Dependence of the Interaction Parameter of Polystyrene and Poly(methyl methacrylate). *Macromolecules* **1990**, *23*, 890−893.

75. Sivaniah, E.; Matsubara, S.; Zhao, Y.; Hashimoto, T.; Fukunaga, K.; Kramer, E. J.; Mates, T. E. Symmetric Diblock Copolymer Thin Films on Rough Substrates: Microdomain Periodicity in Pure and Blended Films. *Macromolecules* **2008**, *41*, 2584−2592.

76. Zhao, Y.; Sivaniah, E.; Hashimoto, T. SAXS Analysis of the Order-Disorder Transition and the Interaction Parameter of Polystyrene-*block*-poly(methyl methacrylate). *Macromolecules* **2008**, *41*, 9948−9951.

77. Ji, S.; Liao, W.; Nealey, P. F. Block Cooligomers: A Generalized Approach to Controlling the Wetting Behavior of Block Copolymer Thin Films. *Macromolecules* **2010**, *43*, 6919–6922.

78. Spruell, J. M.; Levy, B. A.; Sutherland A.; Dichtel, W. R.; Cheng, J. Y.; Stoddart, J. F.; Nelson, A. Facile Postpolymerization End-Modification of RAFT Polymers. *J. Polym. Sci. Part A: Polym. Chem.* **2009**, *47*, 346–356.

79. Khaydarov, A. A.; Hamley, I. W.; Legge, T. M.; Perrier, S. Surface structure of thin asymmetric PS-*b*-PMMA diblock copolymers investigated by atomic force microscopy. *Euro. Polym. J.* **2007**, *43*, 789–796.

80. Schubert, U. S.; Hochwimmer, G.; Spindler, C. E.; Nuyken, O. Controlled polymerization of methylmethacrylate and ethylacrylate using tris(4,4'-dimethyl-2,2'-bipyridine) copper(II) hexafluorophosphate complexes and aluminium isopropoxide. *Polym. Bull.* **1999**, *43*, 319–326.

81. Wang, X.; Luo, N.; Ying, S. Controlled radical polymerization of methacrylates at ambient temperature and the synthesis of block copolymers containing methacrylates. *Polymer* **1999**, *40*, 4157–4161.

82. Treat, N. J.; Sprafke, H.; Kramer, J. W.; Clark, P. G.; Barton, B. E.; Alaniz, J. R.; Fors, B. P.; Hawker, C. J. Metal-Free Atom Transfer Radical Polymerization. *J. Am. Chem. Soc.* **2014**, *136*, 16096−16101.

83. Lu, Z.; Wan, D.; Hung, J. Preparation of PMMA–PS–PMMA via Combination of Anionic and Photoinduced Charge-Transfer Polymerization. *J. Appl. Polym. Sci.* **1999**, *74*, 2072–2076.

84. Sugiyama, K.; Oie, T.; El-Magd, A. A.; Hirao, A. Synthesis of Well-Defined $(AB)_n$ Multiblock Copolymers Composed of Polystyrene and Poly(methyl methacrylate) Segments Using Specially Designed Living AB Diblock Copolymer Anion. *Macromolecules* **2010,** *43*, 1403–1410.

85. Nicolas, J.; Guillaneuf, Y.; Lefay, C.; Bertin, D.; Gigmes, D.; Charleux, B. Nitroxide-mediated polymerization. *Prog. Polym. Sci.* **2013**, *38*, 63–235.

86. Moad, G.; Rizzardo, E.; Thang, S. H. Radical additionefragmentation chemistry in polymer synthesis. *Polymer* **2008**, *49*, 1079–1131.

87. Matyjaszewski, K.; Xia, J. Atom Transfer Radical Polymerization. *Chem. Rev.* **2001**, *101*, 2921−2990.

88. Genabeek, B.; Waal, B. F. M.; Ligt, B.; Palmans, A. R. A.; Meijer, E. M. Dispersity under Scrutiny: Phase Behavior Differences between Disperse and Discrete Low Molecular Weight Block Co-Oligomers. *ACS Macro Lett.* **2017**, *6*, 674−678.

89. Hadjichiristidis, N.; Hirao, A. Anionic Polymerization: Principle, Practice, Strength, Consequences and Applications. *Springer* **2015**.

90. Kim, J.; Kweon, J.; Lee, J.; Noh, S. Synthesis of high molecular weight poly(styrene-*b*-methyl methacrylate) using a plug flow reactor system by anionic polymerization. *Macromol. Res.* **2015**, *23*, 100–110.

91. Tremblay, J.-F. AZ Readies for Chip Self-Assembly. *Chem. Eng. News* **2013**, *91*, 10.

# *Chapter 2*

## *Ester-Amide Exchange Reaction of Polystyrene-block-Poly(methyl methacrylate) for Achieving Sub-10 nm Feature Size*

## 2.1 Introduction

The microphase-separated structures of a block copolymer (BCP) varies depending on several factors, such as the volume fraction of the constituent polymers (*f*), the incompatibility of the blocks, the degree of polymerization, and the molecular architecture.[1,2] The domain spacing (*d*) of a microphase-separated structure is a function of its statistical segment length (*a*), the Flory-Huggins interaction parameter ($\chi$), and the degree of polymerization (*N*) that can be estimated using the expression $d = a\chi^{1/6}N^{2/3}$, where the $\chi$ value is related to the index of incompatibility between the blocks.[3–5] An increase in $\chi$ allows a BCP having a low *N* to be microphase-separated while an insufficient $\chi$ value causes disordering. Consequently, various high $\chi$ BCPs have been designed for achieving features smaller than 10 nm.[6–9] Such high $\chi$ BCPs consist of a specific combination of hydrophobic polymers (e.g., polystyrene and polydimethylsiloxane) with highly polar polymers (e.g., polylactide, polydihydroxystyrene, and oligosaccharides) and thus generally suffer from industrial issues, such as low productivity and high cost due to the difficulty in the synthesis and poor accessibility of the monomers, as described in Section 1.1.3. Therefore, the development of a simple and efficient strategy to produce high-$\chi$ BCPs from readily-available starting materials is of significant interest.

Polystyrene-*block*-poly(methyl methacrylate) (PS-*b*-PMMA) is a leading candidate for the BCP nanofabrication because of its practical advantages as described in Section 1.3, whereas its insufficient incompatibility, i.e., low $\chi$, between the PS and PMMA blocks is a significant disadvantage in the fabrication of the microphase-separated structures with a sub-20 nm domain spacing (*d*).[1,2] Since the PS-*b*-PMMA system has been widely employed as an industrial standard in the practical nanofabrications, the BCP system having both a high-$\chi$ character and chemical structure resembling PS-*b*-PMMA can be a new standard material, leading to the further advancement of the BCP nanofabrication technologies.[10–28] For producing a series of PS-*b*-PMMA derivatives, postpolymerization modification is a suitable procedure because the comonomer compositions and substituent groups can be easily controlled while keeping the original *N* and dispersity (*Đ*).

The methyl ester side chains of PMMA can be transesterified to produce the random copolymers consisting of MMA and modified methacrylate units. Although the transesterification reaction is one of simple modification methods for PMMA, it generally requires base catalysts because of the low reactivity of

the methyl esters in the PMMA.[19] In contrast, the ester-amide exchange (aminolysis) reaction is ideal for the straightforward modification of PMMA, allowing the direct conversion of the methyl ester group into a functional amide or imide group without any catalyst.[20–23] In this study, the author investigated the ester-amide exchange reaction of the PS-*b*-PMMAs with various primary and secondary amines to produce high-$\chi$/low-$N$ PS-*b*-PMMA analogues in a single step (Scheme 2.1). A small number of polar side chains was introduced into the PMMA block of PS-*b*-PMMA to increase the incompatibility between the two blocks and thus realize microphase-separated structures even at a low $N$. This strategy allows to systematically screen a series of high-$\chi$/low-$N$ PS-*b*-PMMA analogues that vary in terms of their comonomer composition, side-chain structure, and $N$ to determine the most promising materials. Various amines, such as ethanolamine, 2-methoxyethanolamine, 2-(2-aminoethoxy)ethanol, *N*-methylethanolamine, benzylamine, and *n*-hexylamine, were used for the ester-amide exchange reaction to introduce a small number of methacrylamide groups into the PMMA block of the parent PS-*b*-PMMA. A small-angle X-ray scattering (SAXS) analysis revealed that a tiny amount of the methacrylamide substituent led to a significant increase in the incompatibility between the blocks. Consequently, the author obtained a lamellar microphase-separated structure with a $d$-spacing as low as 11.1 nm through the simple postpolymerization modification of PS-*b*-PMMA. More importantly, some of the modified PS-*b*-PMMAs indeed formed line patterns in the thin film state with the aid of the directed self-assembly (DSA) technique, thus highlighting the practical utility of the proposed method in nanofabrication such as BCP lithography.

**Scheme 2.1**. Ester-amide exchange reaction of PS-*b*-PMMA with various amines

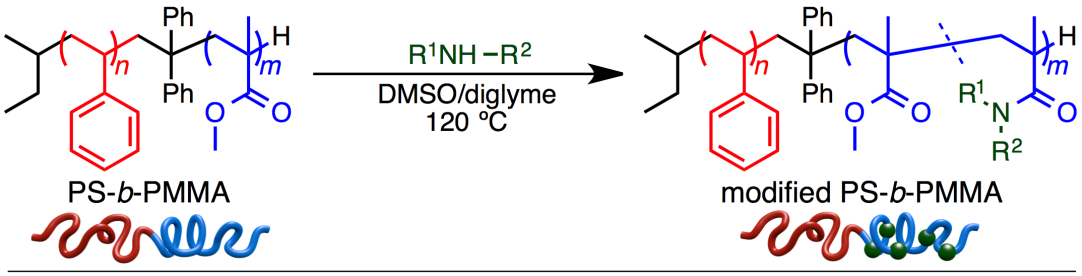


| Total $M_n$ (kg mol$^{-1}$) | Polymer name | |
|---|---|---|
| 42 | **S21M21** | **S21M21-XY** |
| 28 | **S14M12** | **S14M12-XY** |
| 20 | **S10M10** | **S10M10-XY** |
| 14 | **S7M7** | **S7M7-XY** |
| 8.5 | **S4M4** | **S4M4-XY** |

$f_{St}$ = 0.5

X: amines = A,B,C,D,E,F
Y: reaction time = 6,12,18,24 h

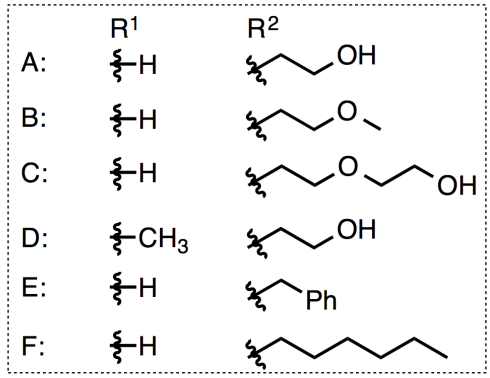


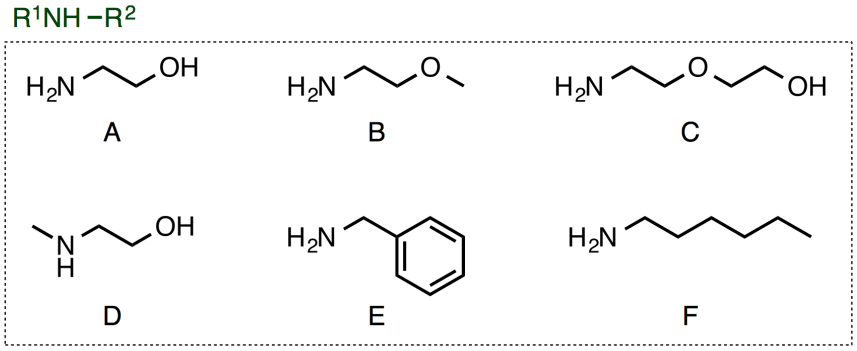

## 2.2 Experimental Section

### *2.2.1 Material*

Ethanolamine (>99.0%), 2-methoxyethylamine (>98.0%), 2-(2-aminoethoxy)ethanol (>98.0%), *N*-methylethanolamine (>99.0%), benzylamine (>99.0%), *n*-hexylamine (>99.0%), diethylene glycol dimethyl ether (diglyme; >99.0%), propylene glycol 1-monomethyl ether 2-acetate (PGMEA; >98%), and 1-methoxy-2-propanol (PGME; >98.0 %) were purchased from Tokyo Chemical Industry Co., Ltd., and used as received. Dimethyl sulfoxide (DMSO; >98.0%) was purchased from Kanto Chemical Co., Inc., and used as received. The cellophane tube (Spectra/por® 6 Membrane; MWCO: 1,000) was purchased from Spectrum Laboratories and was washed with water before use. The solutions of PS-*b*-PMMAs (**S21M21**, 42 kg mol$^{-1}$, $f_{St}$ = 0.54; **S14M14**, 28 kg mol$^{-1}$, $f_{St}$ = 0.54; **S10M10**, 20 kg mol$^{-1}$, $f_{St}$ = 0.54; **S7M7**, 14 kg mol$^{-1}$, $f_{St}$ = 0.52; and **S4M4**, 8.5 kg mol$^{-1}$, $f_{St}$ = 0.52) in PGMEA and random copolymer brushes (PS-*r*-PMMA) were provided by Tokyo Ohka Kogyo Co., Ltd. The PS-*b*-PMMAs were precipitated in methanol and dried before use.

### *2.2.2 Characterization*

The size exclusion chromatography (SEC) experiments were performed at 40 °C in THF using a Shodex GPC-101 gel permeation chromatography system (Shodex DU-2130 dual pump, Shodex RI-71 reflective index detector, and Shodex ERC-3125SN degasser) equipped with a Shodex KF-804L columns (linear, 8 mm × 300 mm linear; particle size, 5 μm; exclusion limit, 4 × 10$^6$) and two Shodex KF-804L columns (linear, 8 mm × 300 mm) at a flow rate of 1.0 mL min$^{-1}$. The number-average molecular weight ($M_{n,SEC}$) and dispersity ($Đ$) values of the polymers were calculated based on the calibration of the polystyrene standards. The $^1$H NMR (400 MHz) spectra were recorded using a JEOL JNM-ECS400 instrument. The FT-IR analysis was performed at room temperature using a Perkin-Elmer Frontier MIR spectrometer equipped with a single-reflection diamond universal attenuated total reflection attachment. The DSC measurements were performed in a nitrogen atmosphere from 30 to 180 °C at the heating rate of 10 °C min$^{-1}$ and cooling rate of −20 °C min$^{-1}$ using a Bruker AXS DSC 3100 system. The SAXS measurements of the bulk samples were performed at room temperature using a Bruker AXS NanoSTAR (light source, Mo-K$\alpha$; $\lambda$ = 0.71 Å; detector, Hi-star: a gas-filled multiwire proportional counter; sample-to-detector distance, 1.06 m) system.

The bulk samples were placed in 1.5-mm-diameter glass capillaries and annealed under vacuum at 200 °C for 24 h. The SAXS profiles were obtained as the plot of the scattering intensity versus scattering vector ($q$), where $q = (4\pi/\lambda)\sin(\theta/2)$ ($\lambda$, wave length; $\theta$, scattering angle). The SEM images were obtained using a Hitachi SU8000 system. The thin films for the static contact angles measurement were prepared by spin-coating (2000 rpm, 60 s) 1% (w/v) polymer solutions in PGME onto Si (100) substrates with a native oxide surface. The static contact angles of water and diiodomethane ($CA_w$ and $CA_I$, respectively) were measured using a DM-700 system (Kyowa Interface Science Co., Ltd.); the volume of a single droplet was 2 μL. The SFE was calculated from the static contact angles of water and diiodomethane using Wu's equation.[24]

### *2.2.3 Ester-Amide Exchange Reaction of PS-b-PMMA*

**Ester-Amide Exchange Reaction of PS-*b*-PMMA with Ethanolamine (S10M10-A18).**

A typical procedure is described as follows (Procedure A): **S10M10** (1.00 g, 50.0 μmol), ethanolamine (415 μL, 25.0 mmol), diglyme (3.0 mL), and DMSO (3.0 mL) were placed in a round-bottom flask. The mixture was stirred at 120 °C for 18 h in a nitrogen atmosphere, then dialyzed with a cellophane tube in methanol; this yielded **S10M10-A18** as a white solid. Yield: 94%; $M_{n,SEC}$ = 19.4 kg mol$^{-1}$; $Đ$ = 1.02.

**Ester-Amide Exchange Reaction of PS-*b*-PMMA with 2-Methoxyethylamine (S10M10-B18).**

Procedure A was used for the reaction of **S10M10** (1.00 g, 0.500 g, 25.0 μmol) with 2-methoxyethylamine (1.08 mL, 12.5 mmol) in diglyme (1.5 mL) and DMSO (1.5 mL); this yielded **S10M10-B18**. Yield: 65 %; $M_{n,SEC}$ = 15.9 kg mol$^{-1}$; $Đ$ = 1.03.

**Ester-Amide Exchange Reaction of PS-*b*-PMMA with 2-(2-Aminoethoxy)ethanol (S10M10-C18).**

Procedure A was used for the reaction of **S10M10** (1.00 g, 0.50 g, 12 μmol) with diethylene glycolamine (1.25 mL, 12.5 mmol) in diglyme (1.5 mL) and DMSO (1.5 mL); this yielded **S10M10-C18** (0.37 g). Yield: 92 %; $M_{n,SEC}$ = 17.8 kg mol$^{-1}$; $Đ$ = 1.04.

**Ester-Amide Exchange Reaction of PS-*b*-PMMA with *N*-Methylethanolamine (S10M10-D18).**

Procedure A was used for the reaction of **S10M10** (1.00 g, 0.50 g, 12 μmol) with *N*-methylethanolamine (1.00 mL, 12.5 mmol) in diglyme (1.5 mL) and DMSO (1.5 mL); this yielded **S10M10-D18**. Yield: 76 %. $M_{n,SEC}$ = 14.9 kg mol$^{-1}$; $Đ$ = 1.09.

**Ester-Amide Exchange Reaction of PS-*b*-PMMA with Benzylamine (S10M10-E18).**

Procedure A was used for the reaction of **S10M10** (1.00 g, 0.50 g, 12 μmol) with benzylamine (1.37 mL, 12.5 mmol) in diglyme (1.5 mL) and DMSO (1.5 mL); this yielded **S10M10-E18**. Yield: 84 %. $M_{n,SEC}$ = 19.5 kg mol$^{-1}$; $Đ$ = 1.02.

**Ester-Amide Exchange Reaction of PS-*b*-PMMA with *n*-Hexylamine (S10M10-F18).**

Procedure A was used for the reaction of **S10M10** (1.00 g, 0.50 g, 12 μmol) with *n*-hexylamine (1.65 mL, 12.5 mmol) in diglyme (1.5 mL) and DMSO (1.5 mL); this yielded **S10M10-F18** (0.45 g). Yield: 90 %. $M_{n,SEC}$ = 18.5 kg mol$^{-1}$; $Đ$ = 1.03.

### *2.2.4 Thin Film Processing for SEM study*

PS-*r*-PMMAs with different compositions were grafted onto the surfaces of silicon substrates before the spin-coating of the polymer solutions. The thin films were prepared by spin-coating a 0.8 wt% polymer solution in PGMEA or PGME onto the substrates using a Mikasa 1H-360S system and thermal annealing at 140 °C for 10 min. Oxygen plasma ashing (200 mL min$^{-1}$, 40 Pa, 40 °C, 200 W, 20 s) was performed on the thin films using a Tokyo Ohka TCA-3822 system to the remove PMMA domain. The film thickness was adjusted to be *ca.* 20 nm. In the DSA study, a 0.4 wt% polymer solution in PGMEA or PGME was spin-coated onto substrates having a guide pattern and a PS-preferential layer. The film thickness was adjusted to 18 nm. The annealing and ashing of the thin films were performed in the same manner.

## 2.3. Results and Discussion

### *2.3.1 Ester-Amide Exchange Reaction of PS-b-PMMA with Ethanolamine*

The author initially subjected PS-*b*-PMMAs to the ester-amide exchange reaction using ethanolamine to introduce a small number of hydroxyethyl methacrylamide groups into the PMMA block (Scheme 1). It was assumed that the incorporation of the hydroxy and amide groups into the PMMA block would increase its incompatibility with the PS block. PS-*b*-PMMAs with the number-average molecular weights of 42, 28, 20, 14, and 8.5 kg mol$^{-1}$ (labeled as **S21M21**, **S14M14**, **S10M10**, **S7M7**, and **S4M4**, respectively) were used as the starting materials. The volume fraction of styrene ($f_{St}$) was fixed at 0.5 to ensure the formation of lamellar structures. The ester-amide exchange reactions were conducted in a mixture of diethylene glycol dimethyl ether (diglyme) and dimethyl sulfoxide (DMSO) (1/1 (v/v)) at 120 °C for 6, 12, 18, and 24 h, wherein a 5-fold molar excess of ethanolamine was added with respect to the MMA units of the PS-*b*-PMMA sample in question. The molecular characteristics of the ethanolamine-modified PS-*b*-PMMAs and the parent PS-*b*-PMMA are shown in Table 2.1. As a representative example, the size exclusion chromatography (SEC) traces of the reaction products from **S10M10**, are depicted in Figure 2.1 along with that of **S10M10**. The products obtained by the reaction of **S10M10** with ethanolamine for 6, 12, 18, and 24 h (**S10M10-A6**, **S10M10-A12**, **S10M10-A18**, and **S10M10-A24**, respectively) displayed a unimodal elution peak with very narrow *Đ* values of <1.03. In the FT-IR spectra of the products, the absorption peaks due to the O−H and C=O stretching vibration were newly observed at around 3,400 and 1,670 cm$^{-1}$, respectively, whose intensity increased with the increasing reaction time (Figure 2.2).[20,25–27] In the $^{1}$H NMR spectra of the obtained products, the signal due to methylene protons adjacent to the amide group was newly observed at 3.5 ppm after the reaction (Figure 2.3). The signal due to the methyl protons adjacent to the unreacted ester group was broadened and diminished with the increasing reaction time, while the side reaction on the PS moiety did not occur because the aromatic signals were still clearly observed without any change. Quantifying the conversion of ester by $^{1}$H NMR was unsuccessful due to the broadened signals, and elemental analysis was therefore employed as an alternative mean. The nitrogen contents of the obtained polymers were found to be 0.11, 0.30, 0.45, and 0.81% for **S10M10-A6**, **S10M10-A12**, **S10M10-A18**, and **S10M10-A24** and the degrees of substitution (DSs) were calculated to be 2, 4, 7, and 12 mol-MMA %, respectively. The ester-

amide exchange reactions of the **S21M21**, **S14M14**, **S7M7**, and **S4M4** with ethanolamine were also performed for the four different reaction times in the same manner (Figure S2.1−S2.9). Importantly, the obtained polymers retained the narrow *Đ* values after the reaction and the DSs were in the range of 1−30 % depending on the reaction time (Table 1). Thus, the author confirmed that the hydroxyethyl amide group was introduced into the PMMA block of PS-*b*-PMMAs by the ester-amide exchange reaction.

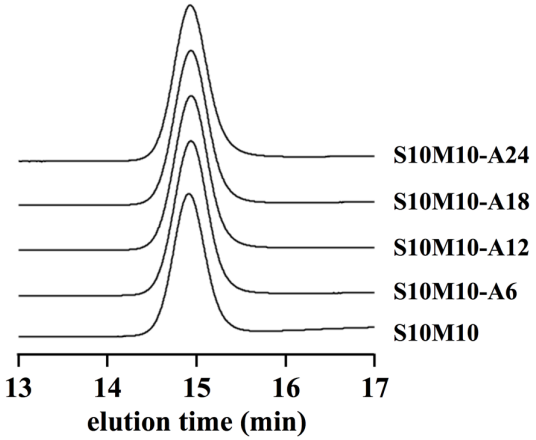


**Figure 2.1**. SEC traces of the ethanolamine-modified **S10M10**s and the parent PS-*b*-PMMA (eluent, THF; flow rate, 1.0 mL $min^{-1}$).

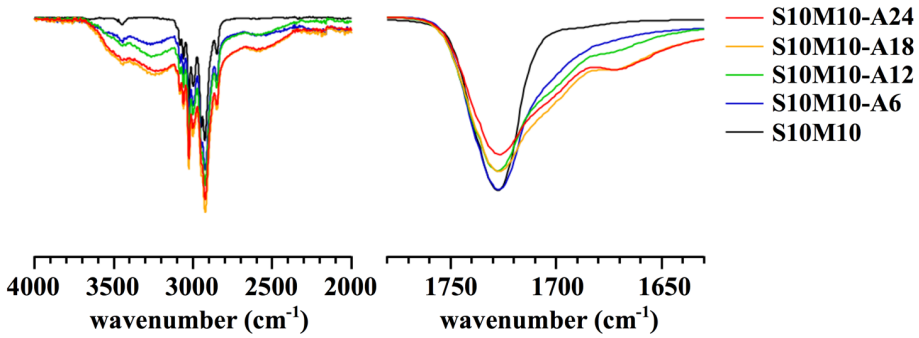


**Figure 2.2.** FT-IR spectra of **S10M10** (black), **S10M10_A6** (blue), **S10M10-A12** (green), **S10M10-A18** (yellow), and **S10M10-A24** (red).

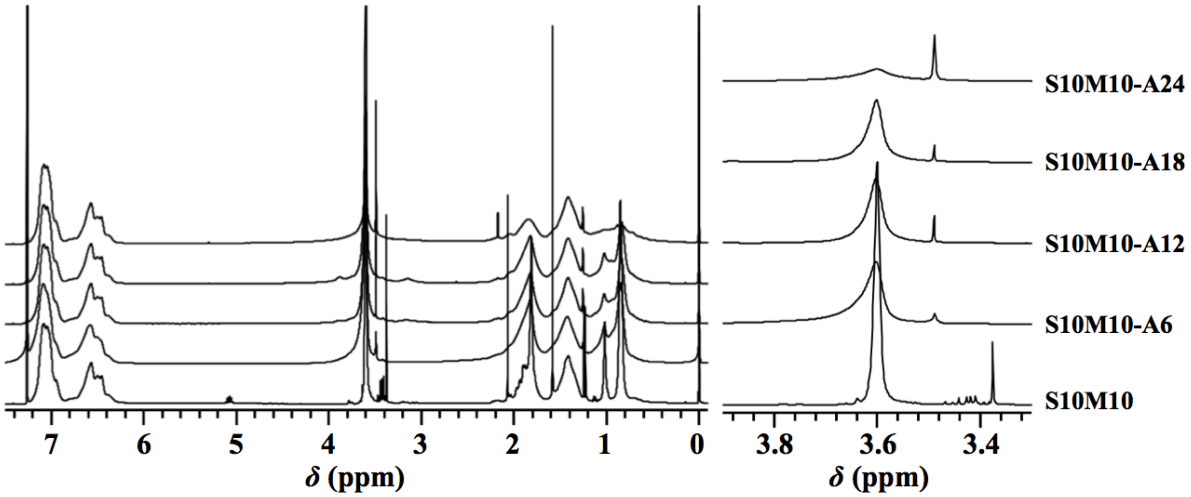


**Figure 2.3**. $^{1}$H NMR spectra of the ethanolamine-modified **S10M10**s and the parent PS-*b*-PMMA in $CDCl_3$ (400 MHz).

**Table 2.1**. Ester-amide exchange reaction of PS-*b*-PMMAs with ethanolamine[a]

| parent polymer | reaction time (h) | $M_{n,SEC}$[b] (kg mol$^{-1}$) | $Đ$[b] | DS[c] (%) | $T_{g1}/T_{g2}$ (°C)[d] | sample name |
|---|---|---|---|---|---|---|
| $PS_{21k}$-*b*-$PMMA_{21k}$ ($f_{St}$ = 0.54) | - | 29.3 | 1.05 | - | 104/124 | **S21M21** |
| | 6 | 21.9 | 1.12 | 4 | 106/158 | **S21M21-A6** |
| | 12 | 26.0 | 1.08 | 3 | 107/168 | **S21M21-A12** |
| | 18 | 28.5 | 1.06 | 5 | 105/170 | **S21M21-A18** |
| | 24 | 27.0 | 1.09 | 11 | 106/ - | **S21M21-A24** |
| $PS_{14k}$-*b*-$PMMA_{14k}$ ($f_{St}$ = 0.54) | - | 21.4 | 1.04 | - | 104/126 | **S14M14** |
| | 6 | 24.3 | 1.03 | 1 | 102/ - | **S14M14-A6** |
| | 12 | 24.1 | 1.03 | 6 | 106/168 | **S14M14-A12** |
| | 18 | 21.6 | 1.07 | 19 | 102/161 | **S14M14-A18** |
| | 24 | 21.7 | 1.07 | 30 | 103/ - | **S14M14-A24** |
| $PS_{10k}$-*b*-$PMMA_{10k}$ ($f_{St}$ = 0.54) | - | 19.8 | 1.02 | - | 109/ - | **S10M10** |
| | 6 | 19.5 | 1.02 | 2 | 102/135 | **S10M10-A6** |
| | 12 | 19.4 | 1.02 | 4 | 103/146 | **S10M10-A12** |
| | 18 | 19.4 | 1.02 | 7 | 101/143 | **S10M10-A18** |
| | 24 | 19.3 | 1.03 | 12 | 101/167 | **S10M10-A24** |
| $PS_{6.6k}$-*b*-$PMMA_{6.9k}$ ($f_{St}$ = 0.52) | - | 13.2 | 1.02 | - | 98/ - | **S7M7** |
| | 6 | 13.1 | 1.02 | 6 | 102/128 | **S7M7-A6** |
| | 12 | 13.2 | 1.04 | 15 | 100/155 | **S7M7-A12** |
| | 18 | 13.1 | 1.03 | 21 | 100/159 | **S7M7-A18** |
| | 24 | 13.2 | 1.04 | 22 | 101/165 | **S7M7-A24** |
| $PS_{4.2k}$-*b*-$PMMA_{4.3k}$ ($f_{St}$ = 0.52) | - | 8.70 | 1.03 | - | 101/ - | **S4M4** |
| | 6 | 8.60 | 1.03 | 5 | 101/ - | **S4M4-A6** |
| | 12 | 8.60 | 1.06 | 12 | 100/158 | **S4M4-A12** |
| | 18 | 8.60 | 1.05 | 13 | 099/149 | **S4M4-A18** |
| | 24 | 8.70 | 1.04 | 29 | 098/159 | **S4M4-A24** |

[a]Reaction condition: nitrogen atmosphere; solvent: DMSO/diglyme = 1/1 (v/v); temperature: 120 °C [b]Determined by SEC in tetrahydrofuran (THF) using PS standards. [c]Degree of substitution of ester group was calculated from nitrogen content as determined by elemental analysis. [d]Dtermined by DSC measurement during second heating (10 °C min$^{-1}$) after first heating (10 °C min$^{-1}$) and cooling (20 °C min$^{-1}$).

Prior to a morphological study, the author performed differential scanning calorimetry (DSC) measurements on the modified PS-*b*-PMMAs and their starting materials to obtain insights into their thermal behaviors. Figure 2.4 displays the DSC curves corresponding to the second heating stage of the products obtained by the reaction of **S10M10** with ethanolamine for 6, 12, 18, and 24 h (**S10M10-A6**, **S10M10-A12**, **S10M10-A18**, and **S10M10-A24**, respectively). The DSC curve of **S10M10** exhibits a baseline shift at approximately 110 °C; this is attributable to the glass transition of the mixed phase of the PS and PMMA blocks and is in keeping with the fact that low-molecular-weight PS-*b*-PMMAs do not phase-separate. In

contrast, two baseline shifts can be clearly observed in the DSC curves of **S10M10-A6** (DS = 2%), **S10M10-A12** (DS = 4%), **S10M10-A18** (DS = 7%), and **S10M10-A24** (DS = 12%) (Table 2.1). These correspond to the glass transition temperatures ($T_g$s) of the PS and PMMA blocks ($T_{g1}$ and $T_{g2}$, respectively), suggesting that the two blocks underwent microphase separation. The enhanced hydrophilicity of the PMMA block increased the incompatibility between the two blocks, resulting in the microphase separation. The baseline shift observed at approximately 102 °C ($T_{g1}$) can be assigned to the PS block; $T_{g1}$ was not affected by the reaction time for the ester-amide exchange. Meanwhile, $T_{g2}$, which was related to the modified PMMA block, lay between 135 to 167 °C and shifted to a higher temperature with an increase in the DS value. The hydroxy and amide groups, which were incorporated during the ester-amide exchange reaction, formed inter- and intramolecular hydrogen bonds that retarded the chain mobility, leading to the observed increase in $T_{g2}$.

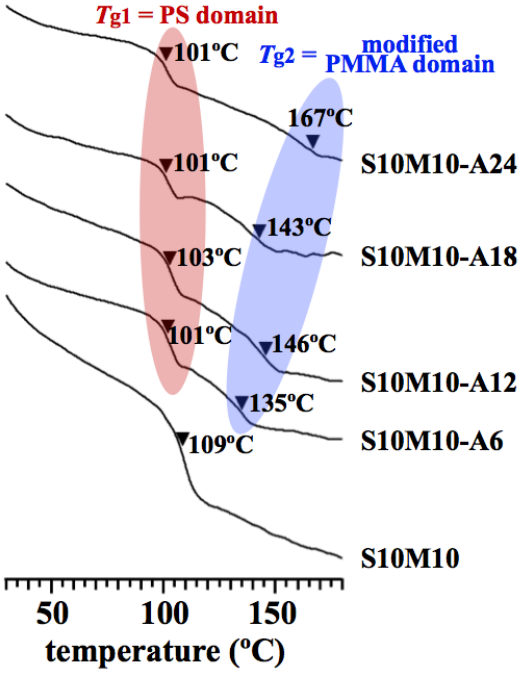


**Figure 2.4**. DSC curves of **S10M10**, **S10M10-A6**, **S10M10-A12**, **S10M10-A18**, and **S10M10-A24** during second heating stage in nitrogen atmosphere at heating rate of 10 °C $min^{-1}$.

### *2.3.2 Microphase Separation of Ethanolamine-modified PS-b-PMMAs in Bulk*

The microphase separation of the modified PS-*b*-PMMAs in the bulk state was investigated using SAXS measurements along with that of the corresponding starting materials. The samples were subjected to thermal annealing at 200 °C for 24 h and subsequently rapidly quenched. Their SAXS profiles were acquired at room temperature. The SAXS profile of **S21M21** clearly showed a primary scattering peak ($q^*$) along with higher-ordered scattering peaks at the $2q^*$ and $3q^*$ positions (Figure 2.5a), indicating the formation of a microphase-separated structure with a lamellar phase. This is in line with the fact that **S21M21** has an $N$ value high enough to be microphase-separated ($N > 300$). The domain spacing ($d$) was calculated from the $q^*$ position, as $d = 2\pi/q^*$, and was determined to be 23.9 nm. The bulk samples of **S21M21-A6** and **S21M21-A18** were also microphase-separated and had lamellar structures with their $d$ values being 29.0 and 29.2 nm, respectively. Based on the SAXS results, it can be concluded that the introduction of the polar side-chains into the PMMA block had a negligible effect on the lamellar morphology of the microphase-separated structure. On the other hand, the $d$ value significantly increased after the incorporation of the polar side-chains. This should be related to the increase in the effective interaction parameter ($\chi_{eff}$) as well as the volume change in the PMMA block after the post-polymerization modification. It is known that the $d$ value of the microphase-separated structure is proportional to $\chi^{1/6}$ as well as $N^{2/3}$, *i.e.*, $d \sim a\chi^{1/6}N^{2/3}$. Given that the value of the constant $a$ remained unchanged after the post-polymerization modification process because of the low DS value, it can be seen that the $\chi_{eff}$ value increased 3.3-fold when only 5% of the methacrylate moieties were replaced by the methacrylamide ones.

The author then examined the nanostructures of the modified PS-*b*-PMMAs with an $M_n$ value of 28.0 kg mol$^{-1}$, *i.e.*, **S14M14-A6** and **S14M14-A18** (Figure 2.5b). The parent PS-*b*-PMMA, **S14M14**, seems to be microphase-separated as evidenced by the sharpness of the primary SAXS scattering peak, albeit without a highly-ordered structure like a lamellar. This was mainly because the $N$ value was not high enough to induce the sharp microphase separation. In contrast, distinct higher-ordered scattering peaks were present at the $2q^*$ and $3q^*$ positions in the SAXS profiles of **S14M14-A6** and **S14M14-A18**, indicating the formation of microphase-separated structures with a lamellar phase. Although the SAXS profiles of **S10M10** and **S7M7** only contained a single broad scattering peak ($q^*$), peaks associated with a lamellar phase were observed in

the case of the corresponding modified PS-*b*-PMMAs (**S10M10-AY** and **S7M7-AY**) (Figure 2.5c, d). The emergence of the higher-ordered scattering patterns in the case of the modified PS-*b*-PMMAs strongly suggested that the low-molecular-weight PS-*b*-PMMAs, which are intrinsically phase-inseparable because of their low $N$ values, had $\chi_{eff}$ values high enough to meet the condition $\chi N > 10.5$ after the hydroxyethyl methacrylamide groups had been introduced into the PMMA block. It is important to note that a low number of hydroxyethyl methacrylamide groups were enough to induce the microphase separation of PS-*b*-PMMA. For example, **S10M10-A6** microphase-separated into a lamellar phase with a $d$ value of 17.0 nm despite its very low DS of 2% (Figure 2.5c). A $d$ value of 17 nm is already beyond the lower limit of the bare PS-*b*-PMMA.[14,28]

To achieve even lower $d$ values using the proposed strategy, the microphase separation of the ethanolamine-modified PS-*b*-PMMAs having the smallest molecular weight was then examined. Notably, the parent PS-*b*-PMMA, **S4M4**, showed a featureless SAXS profile, suggesting that the PS and PMMA blocks were in a completely miscible state in this molecular-weight range (Figure 2.5e). This indicated that a higher DS is required to ensure microphase separation in the case of these low-$N$ PS-*b*-PMMAs. Indeed, the SAXS profile of **S4M4-A6**, which had a DS value as low as 5%, showed only a broad scattering peak ($q^*$); this was reflective of the insufficient incompatibility between the blocks. In contrast, increasing the DS beyond 12% (as in the cases of **S4M4-A12**, **S4M4-A18**, and **S4M4-A24**) resulted in the formation of a lamellar phase, as evidenced by the higher-ordered scattering peaks at positions corresponding to integer multiples of the position of the primary peak ($q^*$). More importantly, the $d$ values for the lamellar phases of **S4M4-A12**, **S4M4-A18**, and **S4M4-A24** were calculated to be 11.3, 11.1, and 12.0 nm, respectively; these are nearly half the minimum $d$ value that can be successfully pattern transferred to silicon substrate (~20 nm).[14,21] Therefore, the ethanolamine-modified PS-*b*-PMMAs, whose parent polymer did not phase-separate due to its low $N$ value, successfully formed microphase-separated structures with extremely low $d$ values because of the simple ester-amide exchange reaction.

To satisfy the requirement for microphase separation, *i.e.*, $\chi N > 10.5$, the $\chi_{eff}$ value of **S4M4-A12** ($N$ = 83) must be greater than 0.127, under the assumption that the volume of the PMMA block was maintained even after the modification. Note that the $\chi$ value of the bare PS-*b*-PMMA was reported to be

approximately 0.036 at 200 °C.[29] In order to briefly estimate the $\chi_{eff}$ values of the ethanolamine-modified PS-*b*-PMMAs, the author used the following equation:[30,31]

$$d_{lam} = 1.10\, a\chi^{1/6}N^{2/3}$$

where $d_{lam}$ are the characteristic lamellar domain spacing (at $f = 0.5$). Although this equation is rigorously valid only for the strong segregation regime, the earlier studies suggested that it give plausible estimates even close to the order-to-disorder transition.[32–34] The average $a$ value for PS-*b*-PMMA is 0.708 nm, as determined using the following equation:

$$a = \left(\frac{f_{PS}}{{a_{PS}}^2} + \frac{f_{PMMA}}{{a_{PMMA}}^2}\right)^{-1/2}$$

where $a_{PS}$ and $a_{PMMA}$ are the statistical segment lengths of PS (0.68 nm) and PMMA (0.74 nm), respectively.[29] Here, the author assumed that $a_{PMMA}$ is the same as the incorporated methacrylamide unit because of the low DS value of the samples. In addition, statistical segment length of structurally related polymers is known to be very similar each other (are typically less than 10 %).[35,36] Taking the $d$ value of **S4M4-A12** (DS = 12%) to be 11.3 nm, the $\chi_{eff}$ value was estimated to be 0.193 (at 200 °C), which is approximately five times that of bare PS-*b*-PMMA (0.036) and is much greater than 0.127, which is the minimum $\chi_{eff}$ value that satisfies the requirement $\chi N > 10.5$. It should be noted that the calculated $\chi_{eff}$ values in this chapter represent a slight overestimation because of the difference in the volume between MMA and the incorporated methacrylamide units in the PMMA block. Nevertheless, the significant increase in the $\chi_{eff}$ value is undoubtedly due to the presence of a number of hydrophilic moieties, including amide and hydroxyl groups, in the PMMA block.

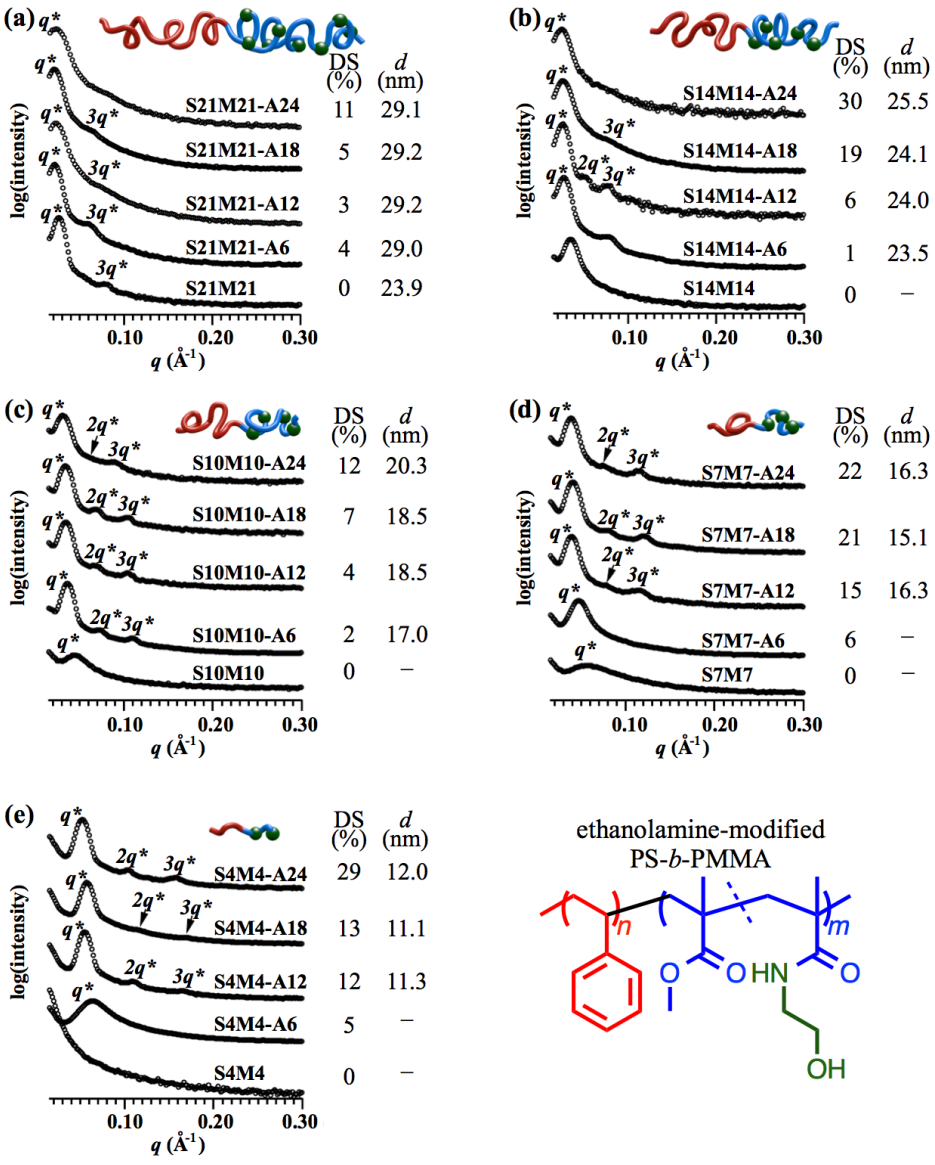


**Figure 2.5**. SAXS profiles of ethanolamine-modified PS-*b*-PMMAs (a: **S21M21-AY**, b: **S14M14-AY**, c: **S10M10-AY**, d: **S7M7-AY**, and e: **S4M4-AY**) and the corresponding PS-*b*-PMMAs (**S21M21**, **S14M14**, **S10M10**, **S7M7**, and **S4M4**) after thermal annealing at 200 °C for 24 h. Degrees of substitution (DSs) were calculated from the nitrogen content as measured by elemental analysis. Domain spacings (*d* values) were determined from the position of the primary peak (*q**) in the SAXS profiles.

### *2.3.3 Preparation and Microphase Separation of Various Amine-Modified PS-b-PMMAs*

To further probe the role of the substituents in the PMMA block responsible for the microphase separation, the author prepared a series of modified PS-*b*-PMMAs with various methacrylamide substituents (Scheme 2.1). Thus, the ester-amide exchange reactions of **S14M14** with 2-methoxyethanolamine (B), 2-(2-aminoethoxy)ethanol (C), *N*-methylethanolamine (D), benzylamine (E), and *n*-hexylamine (F) were performed for 18 h to produce **S14M14-B18** (DS = 2%), **S14M14-C18** (DS = 11%), **S14M14-D18** (DS = 22%), **S14M14-E18** (DS = 4%), and **S14M14-F18** (DS = 11%), respectively, with an *N* value of 274 (Table 2.2). These polymers were then characterized by SEC, FT-IR, and $^1$H NMR measurements as well as elemental analysis (Figure S2.11−2.15). Notably, the DSC thermograms of **S14M14-B18**, **S14M14-C18**, **S14M14-E18**, and **S14M14-F18** exhibited two baseline shifts corresponding to the $T_g$s of the PS and modified PMMA blocks (Figure S2.16 and Table 2.2); this was indicative of the formation of a microphase-separated structure. On the other hand, only a single baseline shift was observed in the DSC thermogram of **S14M14-D18**, suggesting that the PS and modified PMMA blocks were not phase-separated. The ester-amide exchange reactions of **S10M10** were also performed under the same conditions to obtain **S10M10-B18** (DS = 2%), **S10M10-C18** (DS = 9%), **S10M10-D18** (DS = 21%), **S10M10-E18** (DS = 3%), and **S10M10-F18** (DS = 4%) (Table 2.2).

**Table 2.2.** Ester-amide exchange reaction of PS-*b*-PMMA with various amines[a]

| parent polymer | amine[b] | $M_{n,SEC}$[c] (kg mol$^{-1}$) | $Đ$[c] | DS[d] (%) | $T_{g1}/T_{g2}$[f] (°C) | sample name |
|---|---|---|---|---|---|---|
| **S14M14** | B | 24.4 | 1.03 | 2 | 105/143 | **S14M14-B18** |
| | C | 24.3 | 1.03 | 11 | 104/157 | **S14M14-C18** |
| | D | 26.2 | 1.02 | 22 | 102/ - | **S14M14-D18** |
| | E | 25.0 | 1.03 | 4 | 105/150 | **S14M14-E18** |
| | F | 25.1 | 1.03 | 11 | 104/150 | **S14M14-F18** |
| **S10M10** | B | 15.9 | 1.03 | 2 | 102/133 | **S10M10-B18** |
| | C | 17.8 | 1.04 | 9 | 101/150 | **S10M10-C18** |
| | D | 14.9 | 1.09 | 21 | 100/ - | **S10M10-D18** |
| | E | 19.5 | 1.02 | 3 | 102/139 | **S10M10-E18** |
| | F | 18.5 | 1.03 | 4 | 102/139 | **S10M10-F18** |

[a]Reaction condition: nitrogen atmosphere; solvent, DMSO/diglyme = 1/1; temperature, 120 °C; reaction time, 18 h. [b]Amines: A, ethanolamine; B, 2-methoxyethylamine; C, 2-(2-aminoethoxy)ethanol; D, *N*-methylethanolamine; E, benzylamine; F, *n*-hexylamine. [c]Determined by SEC in THF using PS standards. [d]Nitrogen content was determined by elemental analysis, measurement error, ±0.3 %. [e] Degree of substitution of ester group: calculated from the *N* composition. [f]Determined by DSC measurement during second heating (10 °C min$^{-1}$) after first heating (10 °C min$^{-1}$) and cooling (20 °C min$^{-1}$).

Microphase separation in the **S14M14**s modified with various amines was investigated by subjecting the thermally-annealed samples (200 °C for 24 h) to a SAXS analysis. The SAXS analysis of the **S14M14-C18** sample with a 2-(2-hydroxyethoxy)ethyl methacrylamide group indicated the formation of a microphase-separated structure with a lamellar phase (Figure 2.6a). It is likely that the strong polarity of the 2-(2-hydroxyethoxy)ethyl methacrylamide group led to a sharp increase in the incompatibility between the PS and modified PMMA blocks. Interestingly, the modified PS-*b*-PMMA bearing a 2-methoxyethyl methacrylamide group (**S14M14-B18**) also displayed a SAXS pattern attributable to a microphase-separated structure with a lamellar phase. This implied that the hydroxyl group is not an essential structural requirement for inducing microphase separation in this system, although hydroxyl group is effective to enhance the interaction parameter.[6,37,38] Indeed, **S14M14-E18** and **S14M14-F18**, which contained benzyl methacrylamide and *n*-hexyl methacrylamide groups, respectively, also microphase-separated into a lamellar phase, as evidenced by the presence of higher-ordered scattering peaks at the integer multiples of the position of the primary peak ($q^*$). Based on these SAXS results, it can be said that the primary factor responsible for inducement of the microphase separation in the modified PS-*b*-PMMAs is the presence of amide protons and

not the presence of hydroxyl groups. The fact that **S14M14-D18** without amide proton did not form a well-ordered microphase-separated structure supports this hypothesis. Similarly, **S10M10-D18** exhibited a broad peak while **S10M10-B18**, **S10M10-C18**, **S10M10-E18**, and **S10M10-F18** clearly displayed characteristic scattering patterns corresponding to a microphase-separated lamellar structure (Figure 2.6b). This significant contribution of the amide group to enhancing the microphase separation is attributable to the attractive self-interactions within the PMMA blocks. While the chemical incompatibility between the blocks affects the $\chi_{eff}$, the attractive self-interactions within blocks also lead to the increasing $\chi_{eff}$.[35] Nevertheless, the author demonstrated that a wide variety of amines can be used to modify PS-*b*-PMMA so that it exhibits a microphase separation even in the low-$N$ region. This should allow for the fine-tuning of the $\chi$ value, thus making the modified PS-*b*-PMMA system a promising candidate for use in nanofabrication with a sub-10 nm feature size.

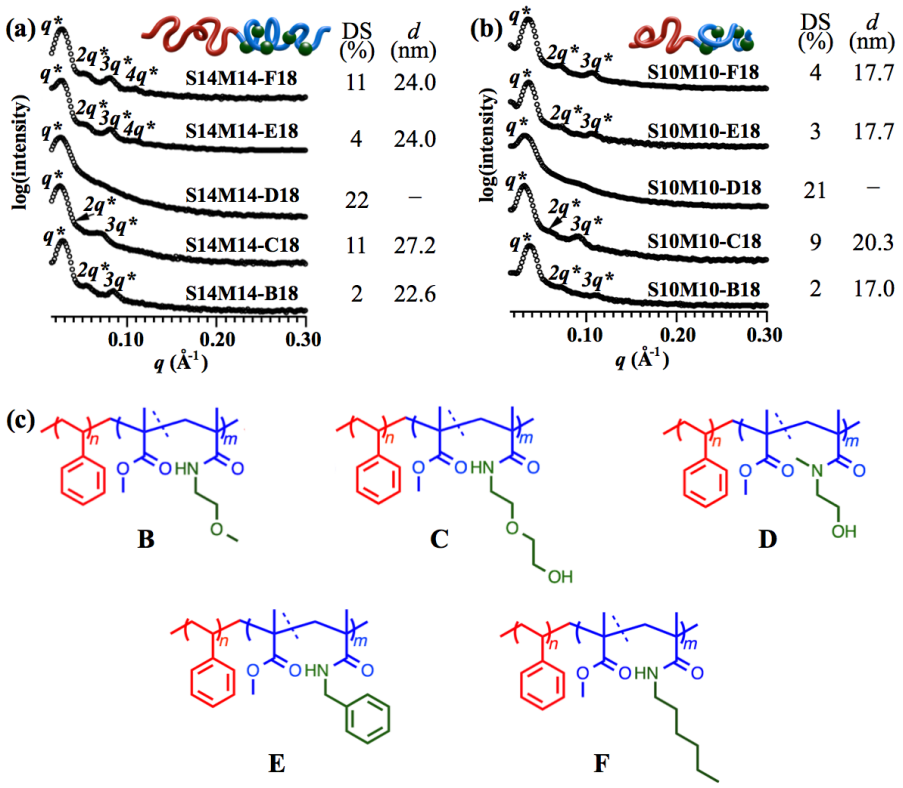


**Figure 2.6**. SAXS profiles of various amines-modified PS-*b*-PMMAs (a: **S14M14-X18** and b: **S10M10-X18**) after thermal annealing at 200 °C for 24 h. The degrees of substitution (DSs) were calculated from the nitrogen content as measured by elemental analysis. Domain spacings (*d* values) were determined from the position of the primary peak (*q**). (c) Structures of modified PS-*b*-PMMAs.

### *2.3.4 Effect of Side-Chain Structures on Incompatibility*

To further understand the influence of the DS value and the side-chain structure on the incompatibility between the PS and modified PMMA blocks, $d/N^{2/3}$ values of the modified PS-*b*-PMMAs were plotted as functions of the DS (Figure 2.7). Note that the $d/N^{2/3}$ value is the proportionality factor for the $\chi_{eff}$ value based on the rearrangement of the relationship "$d \sim \chi^{1/6}N^{2/3}$". The $d/N^{2/3}$ value for the ethanolamine-modified PS-*b*-PMMAs clearly increased with the increasing DS, suggesting that the $\chi_{eff}$ value also tended to increase with the increasing DS (Figure 2.7a). Such relationship between $\chi_{eff}$ and DS is in disagreement with the previous experimental results: some of diblock copolymer consisting of homopolymer

(A) and random copolymer (B-*r*-C), *i.e.*, A-*b*-(B-*r*-C), are known to show a minimum $\chi_{eff}$ at intermediate level of the composition of C (or DS).[32,33] Theoretically, the $\chi_{eff}$ of A-*b*-(B-*r*-C) type copolymer is described as

$$\chi_{\mathrm{eff}} = \frac{DS}{100}\chi_{\mathrm{A-C}} + \left(1 - \frac{DS}{100}\right)\chi_{\mathrm{A-B}} - \frac{DS}{100}\left(1 - \frac{DS}{100}\right)\chi_{\mathrm{B-C}}$$

where the subscripts of A, B, and C refer to each segment and C is the minor comonomer in the random copolymer B-*r*-C.[39–41] When $\chi_{A\text{-}C} > \chi_{A\text{-}B}$ and $(\chi_{A\text{-}C} - \chi_{A\text{-}B}) < \chi_{B\text{-}C}$, such as the case of polystyrene-*b*-poly(isoprene-*r*-epoxidized isoprene)[32] and polystyrene-*b*-poly(isoprene-*r*-fluorinated isoprene)[33], a minimum $\chi_{eff}$ is observed at an intermediate level of the random copolymer composition. In contrast, when $\chi_{A\text{-}C} > \chi_{A\text{-}B}$ and $(\chi_{A\text{-}C} - \chi_{A\text{-}B}) > \chi_{B\text{-}C}$, the $\chi_{eff}$ increases with the increasing DS. Our result and some literatures[35,42] are consistent with the latter case. This demonstrated that the $\chi_{eff}$ value can be simply controlled by adjusting the DS value. In addition, the author found that the side-chain structure also had a pronounced effect on the $d/N^{2/3}$ value of the modified PS-*b*-PMMAs (Figure 2.7b). The fact that the modified PS-*b*-PMMAs prepared by the ester-amide exchange reaction with 2-methoxyethanolamine (**S14M14-B18** and **S10M10-B18**), 2-(2-aminoethoxy)ethanol (**S14M14-C18** and **S10M10-C18**), benzylamine (**S14M14-E18** and **S10M10-E18**), and *n*-hexylamine (**S14M14-F18** and **S10M10-F18**) microphase-separated into a lamellar structure demonstrated that these BCPs also have $\chi_{eff}N$ values higher than 10.5. Of these, **S14M14-C18** and **S10M10-C18** showed particularly higher $d/N^{2/3}$ values than the others. Therefore, the incorporation of amide units into the PMMA block can induce microphase separation even at a very small DS. Overall, the author confirmed that the $\chi_{eff}$ value of the modified PS-*b*-PMMAs can be controlled to the desirable level based on the DS as well as the choice of the introduced side chain.

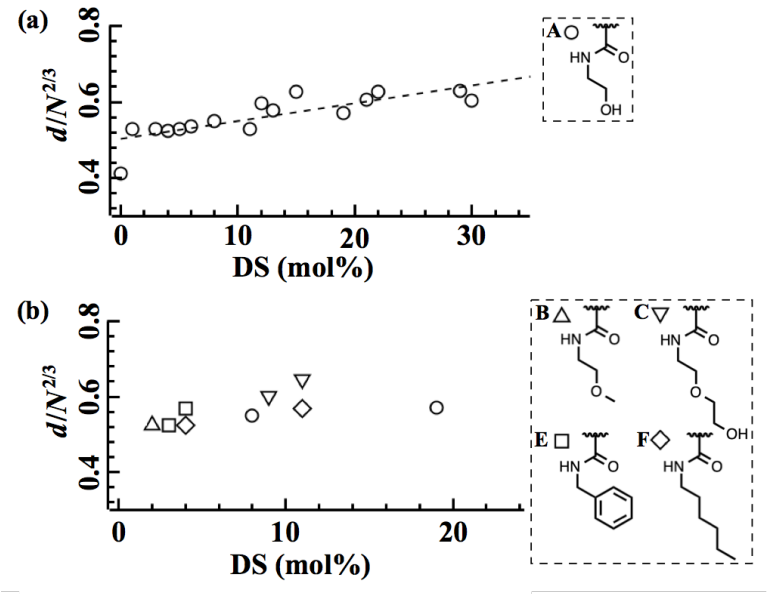


**Figure 2.7**. DS dependency of $d/N^{2/3}$ of (a) ethanolamine-modified PS-*b*-PMMAs having $M_n$ values of 42, 28, 20, 14, and 8.5 kg mol$^{-1}$ and (b) various amines-modified PS-*b*-PMMAs having $M_n$ values of 28 and 20 kg mol$^{-1}$. The plotted data were the averaged values of $d/N^{2/3}$ of each sample having same DS values.

### *2.3.5 Microphase Separation in Thin Film*

The author next investigated the microphase-separated structure of the modified PS-*b*-PMMAs thin films on silicon substrates to evaluate their practical applicability for nanofabrication applications. Therefore, the main purpose of this part of the study was to evaluate the morphology and microdomain orientation in the thin film state. The BCP thin films were prepared by spin-coating a 0.8 wt% propylene glycol methyl ether acetate (PGMEA) solution on silicon substrates modified with polystyrene-*random*-poly(methyl methacrylate) (PS-*r*-PMMA) brushes and subsequently thermally annealed at 140 °C for 10 min. The PS-*r*-PMMA brushes, which had the PS mole ratio ranging from 0 to 99% and thus would have different preferences for PS and PMMA, were used as the underlayer for the thin films to control the orientation of the microphase-separated structure.[43,44] Top-view SEM images of the thin films were acquired after oxygen plasma ashing to selectively remove the modified PMMA domain. As shown in Figure 2.8, **S14M14-A6**, **S14M14-A6**, and **S10M10-A12** showed a fingerprint-like pattern when the PS-*r*-PMMAs with styrene

contents of 60, 40, and 20 mol%, respectively, were used as the underlayer. The difference in the neutral range of the underlayer composition implies significant change in the surface energy of the modified block even at the low DS. The fast Fourier transformation images of the SEM images showed that the distances between the strips of the obtained fingerprint patterns were 20, 20, and 17 nm for **S14M14-A6**, **S14M14-A12**, and **S10M10-A12**, respectively. These values are in good agreement with the *d* values calculated from the SAXS results. The corresponding half-pitches were 10, 10, and 8.5 nm, respectively. In addition, **S14M14-E18** and **S14M14-F18**, which contained benzyl and *n*-hexyl methacrylamide moieties, respectively, also exhibited a fingerprint-like pattern (Figure 2.9). These morphological investigations of the modified PS-*b*-PMMA thin films further supported the SAXS analysis.

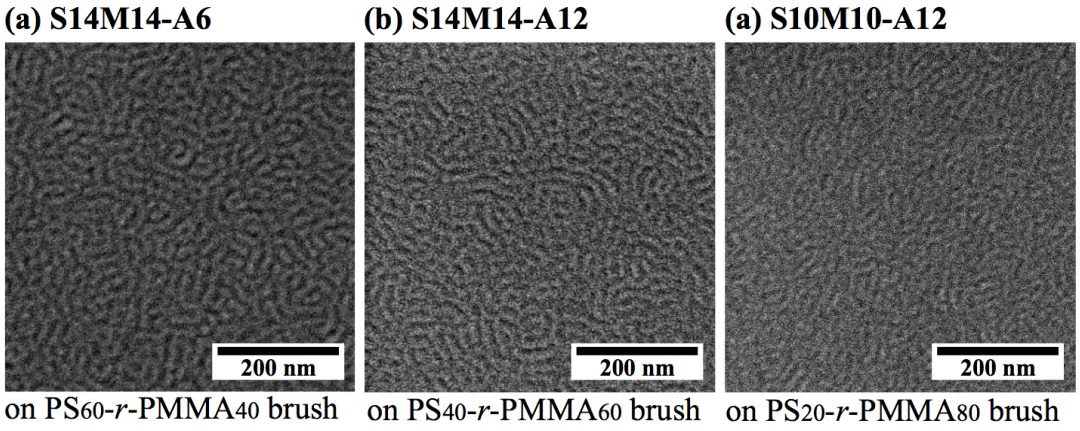


**Figure 2.8**. Top-view SEM images of (a) **S14M14-A6**, (b) **S14M14-A12**, and (c) **S10M10-A12** on PS-*r*-PMMA-grafted (styrene composition = 60, 40, and 20 mol%, respectively) silicon wafers. Oxygen plasma was used to selectively remove the PMMA block before the observations. Scale bars are 200 nm. The film thickness is 22 nm.

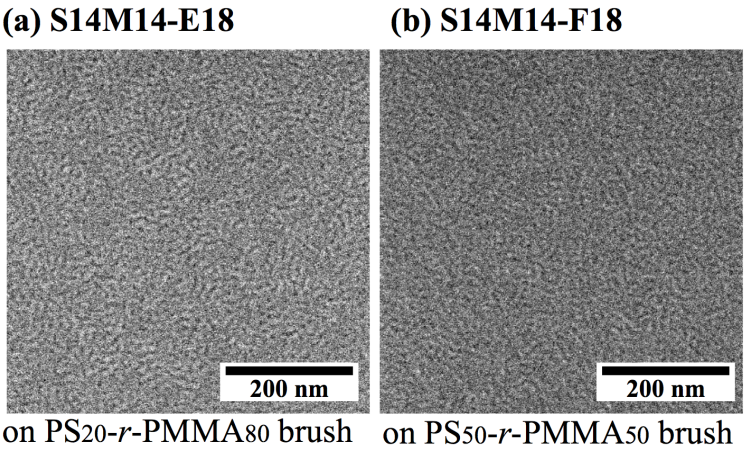


**Figure 2.9**. Top-down SEM images of (a) **S14M14-E18** and (b) **S14M14-F18** on PS-*r*-PMMA (styrene composition = 20 and 50 mol %, respectively)-coated silicon wafer after annealing at 140 °C for 10 min. An oxygen plasma was used to selectively remove the PMMA block. Scale bars are 200 nm. The domain distances of **S14M14-E18** and **S14M14-F18** were determined to be 20 and 18 nm, respectively, from FFT images.

### *2.3.6 Investigation of Surface Neutrality in Modified PS-b-PMMA Thin Film*

In the thin film state, the surface neutrality of BCP at both the substrate and free surfaces is one of important factors to control the orientation of the microdomain. Therefore, the author first evaluated the surface free energy (SFE) of the modified PMMA *via* contact angle (CA) measurements. A PMMA homopolymer with an $M_n$ value of 20 kg mol$^{-1}$ (**M20**) was treated with ethanolamine to produce the modified **M20**s with DS values of 1–10% (Figure S2.17−S2.19 and Table 2.3). The contact angle measurements were performed on the thin films of these modified PMMAs, which were prepared by spin-coating a 1% 1-methoxy-2-propanol (PGME) solution of them. The test liquids were water and diiodomethane. The SFE of **M20** and the modified **M20**s with DS values of 2, 8, and 10% (**M20-A6**, **M20-A12**, and **M20-A24**, respectively) were determined to be 48.4 (which was in agreement with the literature data[45]), 48.8, 51.0, and 50.9, respectively. It is noteworthy that the SFE values of the modified PMMAs with a DS lower than 10% were comparable to that of **M20**, even though the incorporation of the hydroxyethyl methacrylamide groups

increased the incompatibility of the PMMA with PS in the BCPs. This contradictory result can be attributed to the enhanced intrablock attraction in the modified PMMA block.[35] The author then studied the thickness of the island and hole relief structures for the **S14M14-6A** and **S10M10-6A** thin films on the PS-*r*-PMMA underlayers with the different compositions to understand the interfacial neutrality of both blocks at the substrate and free surfaces.[46,47] The test results suggested that these samples have the preferential surface at the free surface, while they exhibited a neutral surface to the PS-*r*-PMMA underlayer at certain compositions. Therefore, the perpendicular lamellae formation in the modified PS-*b*-PMMAs seem not to be driven by the surface neutrality. To determine the other possibilities, the author investigated the as-cast thin films of **S14M14-A6** and **S14M14-A12**. Interestingly, perpendicular lamellae were observed in both of the as-cast thin films. This observation implied that the solvent vapor created a neutral environment at the free surface during the spin-coating process, so that the perpendicular lamellae was observed in the modified PS-*b*-PMMA thin films.

**Table 2.3**. Statistical contact angles and surface free energies of the ethanolamine-modified PMMAs[a]

| polymer name | reaction time (h) | $M_{n,SEC}$[b] (kg mol$^{-1}$) | $Đ$[b] | DS[c] (%) | $CA_w$[d] (deg) | $CA_I$[d] (deg) | SFE[e] (J m$^{-2}$) |
|---|---|---|---|---|---|---|---|
| **M10** | - | 20.3 | 1.02 | - | 65.1 | 35.5 | 48.4 |
| **M10-A6** | 6 | 20.4 | 1.02 | 2 | 63.4 | 36.7 | 48.8 |
| **M10-A12** | 12 | 20.4 | 1.03 | 8 | 58.4 | 37.8 | 51.0 |
| **M10-A24** | 24 | 20.5 | 1.03 | 10 | 58.4 | 37.9 | 50.9 |

[a]Reaction condition: nitrogen atmosphere; solvent, DMSO/diglyme = 1/1 (v/v); temperature, 120 °C. [b]Determined by SEC in THF using PS standards. [c]Degree of substitution of ester group was calculated from the nitrogen content. [d]Static contact angles of water ($CA_w$) and diiodomethane ($CA_w$). [e]Surface free energy was calculated from $CA_w$ and $CA_I$ using Wu's equation.

### *2.3.7 Directed-Self Assembly*

Finally, the author examined the compatibility of the modified PS-*b*-PMMAs with the directed self-assembly (DSA) process. With respect to the nanofabrication applications, DSA using chemical or topographical guide patterns is necessary for producing the device-relevant nanostructures. In this study, the author employed the graphoepitaxy technique while using topographically prepatterned silicon substrates with PS brush underlayers (Figure 2.9a). After optimizing the various parameters, including the film thickness

(FT), guide pattern width, and brush underlayer, the author finally succeeded in obtaining the desired line-and-space pattern using several samples of the modified PS-*b*-PMMAs. Figure 2.9b shows top-view SEM images of an **S10M10-A6** thin film (FT = 18 nm) prepared by spin-coating and subsequent thermal annealing at 200 °C for 10 min (after the $O_2$ plasma ashing process). It can be seen that a well-aligned line-and-space pattern was formed by PS along the guide pattern. The half-pitch of the line patterns was 10 nm, which is almost equal to half the *d*-spacing value calculated from the SAXS results. In addition, line-and-space patterns with a half-pitch of 9 nm could also be produced with the **S10M10-E18** and **S10M10-F18** thin films using the same process (Figure 2.9c and d). These thin film experiments revealed that the modified PS-*b*-PMMA system is amenable to the existing DSA process and can be a suitable candidate for nanofabrication materials that allow for the realization of the sub-10-nm patterning.

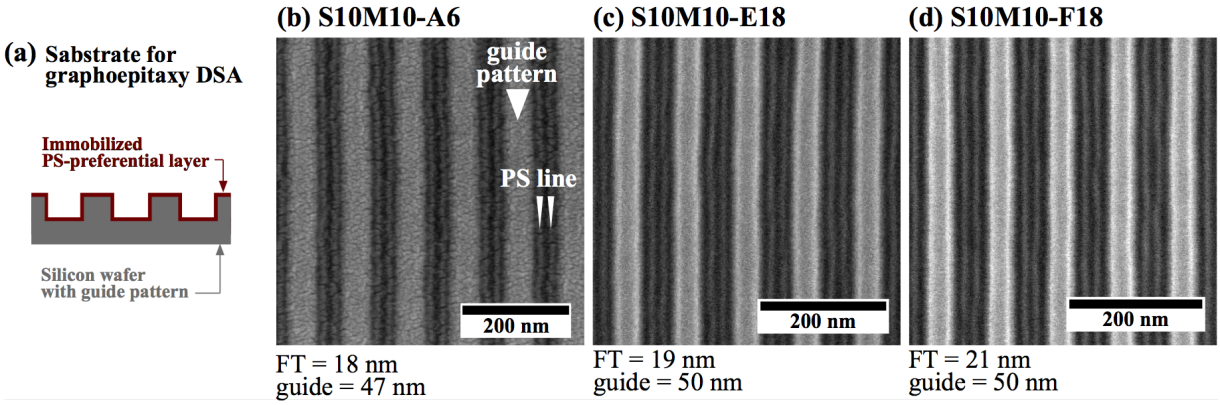


**Figure 2.9**. Demonstration of graphoepitaxy DSA. (a) Illustration of the substrate for DSA. Top-view SEM images of (b) **S10M10-A6**, (c) **S10M10-E18**, and (d) **S10M10-F18** aligned by graphoepitaxy DSA process on the PS-preferential layer. The film thicknesses (FT) and widths of the guide patterns were 18, 19, and 21 nm and 47, 50, and 50 nm, respectively. Oxygen plasma was used to selectively remove the PMMA block before the observations. Scale bars are 200 nm.

## 2.4. Conclusion

In this chapter, the author demonstrated that the ester-amide exchange reaction of PS-*b*-PMMA with various amines is a facile and efficient modification technique for controlling the incompatibility between the PS and PMMA blocks. The methacrylamide groups incorporated in the PMMA block resulted in a high incompatibility between the blocks and allowed for the microphase separation even at low *N* values. The modified PS-*b*-PMMA with an *N* value of 83 and DS of 21%, namely, **S4M4-A18**, produced a lamellar phase with the smallest size features (half-pitch) of 5.6 nm. This is markedly smaller than the lower limit of the pattern size obtainable using the bare PS-*b*-PMMA. More importantly, the author found that the modified PS-*b*-PMMAs form fingerprint-like nanopatterns in the thin film state *via* a simple thermal annealing process. Furthermore, the modified PS-*b*-PMMAs were compatible with the graphoepitaxy DSA process, which allowed the formation of a line-and-space pattern along the prepattern, thus confirming their possible application in nanofabrication processes. Hence, the proposed technique is an easy way of achieving a high-$\chi$/low-*N* BCP system from the industrially-useful BCP, PS-*b*-PMMA.

## 2.5. Reference


1. Bates, F. S.; Fredrickson, G. H. Block Copolymer Thermodynamics: Theory and Experiment. *Annu. Rev. Phys. Chem.* **1990**, *41*, 525−557.

2. Jiang, C.; Qiang, Y.; Li, W.; Qiu, F.; Shi, A. Effects of Chain Topology on the Self-Assembly of AB-Type Block Copolymers. *Macromolecules* **2018**, *51*, 1529−1538.

3. Semenov, A. N. Theory of Block-Copolymer Interface in the Strong Segregation Limit. *Macromolecules* **1993**, *26*, 6617−6621.

4. Matsen, M. W.; Bates, F. S. Unifying Weak- and Strong- Segregation Block Copolymer Theories. *Macromolecules* **1996**, *29*, 1091−1098.

5. Sinturel, C.; Bates, F. S.; Hillmyer, M. A. High χ−Low N Block Polymers: How Far Can We Go? *ACS Macro Lett.* **2015**, *4*, 1044− 1050.

6. Kwak, J.; Mishra, A. K.; Lee, J.; Lee, K. S.; Choi, C.; Maiti, S.; Kim, M.; Kim, J. K. Fabrication of Sub-3 nm Feature Size Based on Block Copolymer Self-Assembly for Next-Generation Nanolithography. *Macromolecules* **2017**, *50*, 6813−6818.

7. Nowak, S. R.; Hwang, W.; Sita, L. R. Dynamic Sub-10-nm Nanostructured Ultrathin Films of Sugar-Polyolefin Conjugates Thermoresponsive at Physiological Temperatures. *J. Am. Chem. Soc.* **2017**, *139*, 5281−5284.

8. Togashi, D.; Otsuka, I.; Borsali, R.; Takeda, K.; Enomoto, K.; Kawaguchi, S.; Narumi, A. Maltopentaose-Conjugated CTA for RAFT Polymerization Generating Nanostructured Bioresource-Block Copolymer. *Biomacromolecules* **2014**, *15*, 4509−4519.

9. Cushen, J. D.; Otsuka, I.; Bates, C. M.; Halila, S.; Fort, S. B.; Rochas, C.; Easley, J. A.; Rausch, E. L.; Thio, A.; Borsali, R.; et al. Oligosaccharide/Silicon-Containing Block Copolymers with 5 nm Features for Lithographic Applications. *ACS Nano* **2012**, *6*, 3424− 3433.

10. Ahn, H.; Ryu, D. Y.; Kim, Y. Kwon, K. W.; Lee, J.; Cho, J. Phase Behavior of Polystyrene-*b*-Poly(methyl methacrylate) Diblock Copolymer. *Macromolecules* **2009**, *42*, 7897–7902.

11. Aimi, J.; Komura, M.; Iyoda, T.; Saeki, A.; Seki, S.; Takeuchi, M.; Nakanishi, T. Synthesis and Self-Assembly of Phthalocyanine-tethered Block Copolymers. *J. Mater. Chem. C* **2015**, *3*, 2484–2490.

12. Kim, K.; Park, S.; Kim, Y.; Bang, J.; Park, C.; Ryu, D. Y. Optimized Solvent Vapor Annealing for Long-Range Perpendicular Lamellae in PS-*b*-PMMA Films. *Macromolecules* **2016**, *49*, 1722−1730.

13. Tremblay, J.-F. AZ Readies for Chip Self-Assembly. *Chem. Eng. News* **2013**, *91*, 10.

14. Wan, L.; Ruiz, R.; Gao, H.; Patel, K. C.; Albrecht, T. R.; Yin, J.; Kim, J.; Cao, Y.; Li, G. The Limits of Lamellae-Forming PS-*b*-PMMA Block Copolymers for Lithography. *ACS Nano* **2015**, *9*, 7506−7514.

15. Kim, B. H.; Shin, D. O.; Jeong, S. J.; Koo, C. M.; Jeon, S. C.; Hwang, W. J.; Lee, S.; Lee, M. G.; Kim, S. O.; Hierarchical Self-Assembly of Block Copolymers for Lithography-Free Nanopatterning. *Adv. Mater.* **2008**, *20*, 2303–2307.

16. Jin, H. M.; Lee, S. H.; Kim, J. Y.; Son, S. W.; Kim, B. H.; Lee, H. K.; Mun, J. H.; Cha, S. K.; Kim, J. S.; Nealey, P. F.; Lee, K. J.; Kim, S. O. Laser Writing Block Copolymer Self-Assembly on Graphene Light-Absorbing Layer. *ACS Nano* **2016**, *10*, 3435−3442.

17. Jin, H. M.; Park, D. Y.; Jeong, S. J.; Lee, G. Y.; Kim, J. Y.; Mun, J. H.; Cha, S. K.; Lim, J.; Kim, J. S.; Kim, K. H.; Lee, K. J.; Kim, S. O. Flash Light Millisecond Self-Assembly of High $\chi$ Block Copolymers for Wafer-Scale Sub-10 nm Nanopatterning. *Adv. Mater.* **2017**, *29*, 1700595.

18. Kim, B. H.; Lee, D. H.; Kim, J. Y.; Shin, D. O.; Jeong, H. Y.; Hong, S.; Yun, J. M.; Koo, C. M.; Lee, H.; Kim, S. O. Mussel-Inspired Block Copolymer Lithography for Low Surface Energy Materials of Teflon, Graphene, and Gold. *Adv. Mater.* **2011**, *23*, 5618–5622.

19. Fleischmann, C.; Anastasaki, A.; Gutekunst, W. R.; McGrath, A. J.; Hustad, P. D.; Clark, P. G.; Laitar, D. S.; Hawker, C. J. Direct Access to Functional (Meth)Acrylate Copolymers Through Transesterification with Lithium Alkoxides. *J. Polym. Sci. Part A: Polym. Chem.* **2017**, *55*, 1566–1574.

20. Kakuchi, R.; Wongsanoh, K.; Hoven, V. P.; Theato, P. Activation of Stable Polymeric Esters by Using Organo-Activated Acyl Transfer Reactions. *J. Polym. Sci. Part A: Polym. Chem.* **2014**, *52*, 1353–1358.

21. Legay, R.; Roussel, J.; Boutevin, B.; Synthesis of Polyglutarimides from P(methyl methacrylate) and Cyclohexylamine. I. Influence of Working Conditions on Imidization Reaction. *J. Appl. Polym. Sci.* **2000**, *76*, 1876–1888.

22. Fixe, F.; Dufva, M.; Telleman, P.; Christensen, C. B. V. Functionalization of poly(methyl methacrylate) (PMMA) as a substrate for DNA microarrays. *Nucl. Acids Res.* **2004**, *32*, e9.

23. Brown, L.; Koerner, T.; Horton, J. H.; Oleschuk, R. D. Fabrication and characterization of poly(methylmethacrylate) microfluidic devices bonded using surface modifications and solvents. *Lab Chip* **2006**, *6*, 66–73.

24. Wu, S.; Brzozowski, K. J. Surface Free Energy and Polarity of Organic Pigments. *J. Coll. Int. Sci.* **1971**, *37*, 686−690.

25. Note that the slight increase in peak intensity with the increasing reaction time at 1700 $cm^{-1}$ should be attributed to formation of the small quantity of glutarimide from the ester group of neighboring two MMA units.

26. Legay, R.; Roussel, J.; Boutevin, B. Synthesis of Polyglutarimides from P(methyl methacrylate) and Cyclohexylamine. I. Influence of Working Conditions on Imidization Reaction. *J. Appl. Polym. Sci.* **2000**, *76*, 1876−1888.

27. Legay, R.; Roussel, J.; Boutevin, B. Synthèse de Polyglutarimides à Partir de PMMA, et de la II Méthylamine Influence des Conditions Opératoires sur la Réaction D'imidification. *Eur. Polym. J.* **2000**, *36*, 1365−1371.

28. Sivaniah, E.; Matsubara, S.; Zhao, Y.; Hashimoto, T.; Fukunaga, K.; Kramer, E. J.; Mates, T. E. Symmetric Diblock Copolymer Thin Films on Rough Substrates: Microdomain Periodicity in Pure and Blended Films. *Macromolecules* **2008**, *41*, 2584−2592.

29. Russell, T. P.; Hjelm Jr., R. P.; Seeger, P. A. Temperature Dependence of the Interaction Parameter of Polystyrene and Poly(methyl methacrylate). *Macromolecules* **1990**, *23*, 890−893.

30. Zalusky, A. S.; Olayo-Valles, R.; Wolf, J. H.; Hillmyer, M. A. Ordered Nanoporous Polymers from Polystyrene-Polylactide Block Copolymers. *J. Am. Chem. Soc.* **2002**, *124*, 12761−12773.

31. In general, the volume-averaged degree of polymerization based on a reference volume is used to calculate the $\chi$ value. However, in this study, the chemical degree of polymerization was employed for simplification.

32. Kim, S.; Nealey, P. F.; Bates, F. S. Decoupling Bulk Thermodynamics and Wetting Characteristics of Block Copolymer Thin Films. *ACS Macro Lett.*, **2012**, *1*, 11–14.

33. Ren, Y.; Lodge, T. P.; Hillmyer, M. A. *Macromolecules* **2000**, *33*, 866–876.

34. Almdal, K.; Rosedale, J. H.; Bates, F. S.; Wignall, G. D.; Fredrickson, G. H. *Phys. Rev. Lett.* **1990**, *65*, 1112–1115.

35. Zhou, S. X.; Janes, D. W.; Kim, C. B.; Willson, C. G.; Ellison, C. J. Designing Intrablock Attractions To Increase the $\chi$ Parameter of a Symmetric Diblock Copolymer. *Macromolecules*, **2016**, *49*, 8332–8340.

36. Gehlsen, M.; Weimann, P. Synthesis and Characterization of Poly(Vinylcyclohexane) Derivatives. *J. Polym. Sci.: Part B: Polym. Phys.* **2003**, *33*, 1527-1536.

37. Seshimo, T.; Maeda, R.; Odashima, R.; Takenaka, Y.; Kawana, D.; Ohmori, K.; Hayakawa, T. Perpendicularly oriented sub-10-nm block copolymer lamellae by atmospheric thermal annealing for one minute. *Scientific Reports* **2016**, *6*, 19481−19488.

38. Yu, D. M.; Mapas, J. K. D.; Kim, H.; Choi, J.; Ribbe, A. E.; Rzayev, J.; Russell, T. P. Evaluation of the Interaction Parameter for Poly(solketal methacrylate)-*block*-polystyrene Copolymers. *Macromolecules*, **2018**, *51*, 1031−1040.

39. Kambour, R. P.; Bendler, J. T.: Bopp, R. C. Phase Behavior of Polystyrene, Poly(2,6-dimethyl-l,4-phenylene oxide), and Their Brominated Derivatives. *Macromolecules* **1983**, *16*, 753−757.

40. Brinke, G. T.; Karasz, F. E.; MacKnight. W. J. Phase Behavior in Copolymer Blends: Poly(2,6-dimethyl-l,4-phenylene oxide) and Halogen-Substituted Styrene Copolymers. *Macromolecules* **1983**, *16*, 1827−1832.

41. Roe, R. J.; Zin, W. C. Determination of the Polymer-Polymer Interaction Parameter for the Polystyrene-Polybutadiene Pair. *Macromolecules* **1980**, *13*, 1221−1228.

42. Park, M. J.; Balsara, N. P. Phase Behavior of Symmetric Sulfonated Block Copolymers. *Macromolecules*, **2008**, *41*, 3678–3687.

43. Mansky, P.; Liu, Y.; Huang, E.; Russell, T. P.; Hawker, C. Controlling Polymer-Surface Interactions with Random Copolymer Brushes. *Science* **1997**, *275*, 1458−1460.

44. Chen, X.; Zhou, C.; Chen, S. J.; Craig, G. S. W.; Rincon-Delgadillo, P.; Dazai, T.; Miyagi, K.; Maehashi, T.; Yamazaki, A.; Gronheid, R.; Stoykovich, M. P.; Nealey, P. F. Ionic Liquids as Additives to Polystyrene-*Block*-Poly(Methyl Methacrylate) Enabling Directed Self-Assembly of Patterns with Sub-10 nm Features *ACS Appl. Mater. Interfaces*, **2018**, *10*, 16747–16759.

45. Mangipudi, V. S.; Huang, E.; Tirrell, M Measurement of Interfacial Adhesion Between Glassy Polymers Using The JKR Method. *Macromol. Symp.* **1996**, *102*, 131−143.

46. Kim, S.; Bates, C. M.; Thio, A.; Cushen, J. D.; Ellison, C. J.; Willson, C. G.; Bates, F. S. Consequences of Surface Neutralization in Diblock Copolymer Thin Films. *ACS Nano* **2013**, *7*, 9905–9919.

47. Maher, M. J.; Self, J. L.; Stasiak, P.; Blachut, G.; Ellison, C. J.; Matsen, M. W.; Bates, C. M.; Willson, C. G. Structure, Stability, and Reorganization of 0.5 $L_0$ Topography in Block Copolymer Thin Films. *ACS Nano* **2016**, *10*, 10152−10160.

## 2.6 Appendix

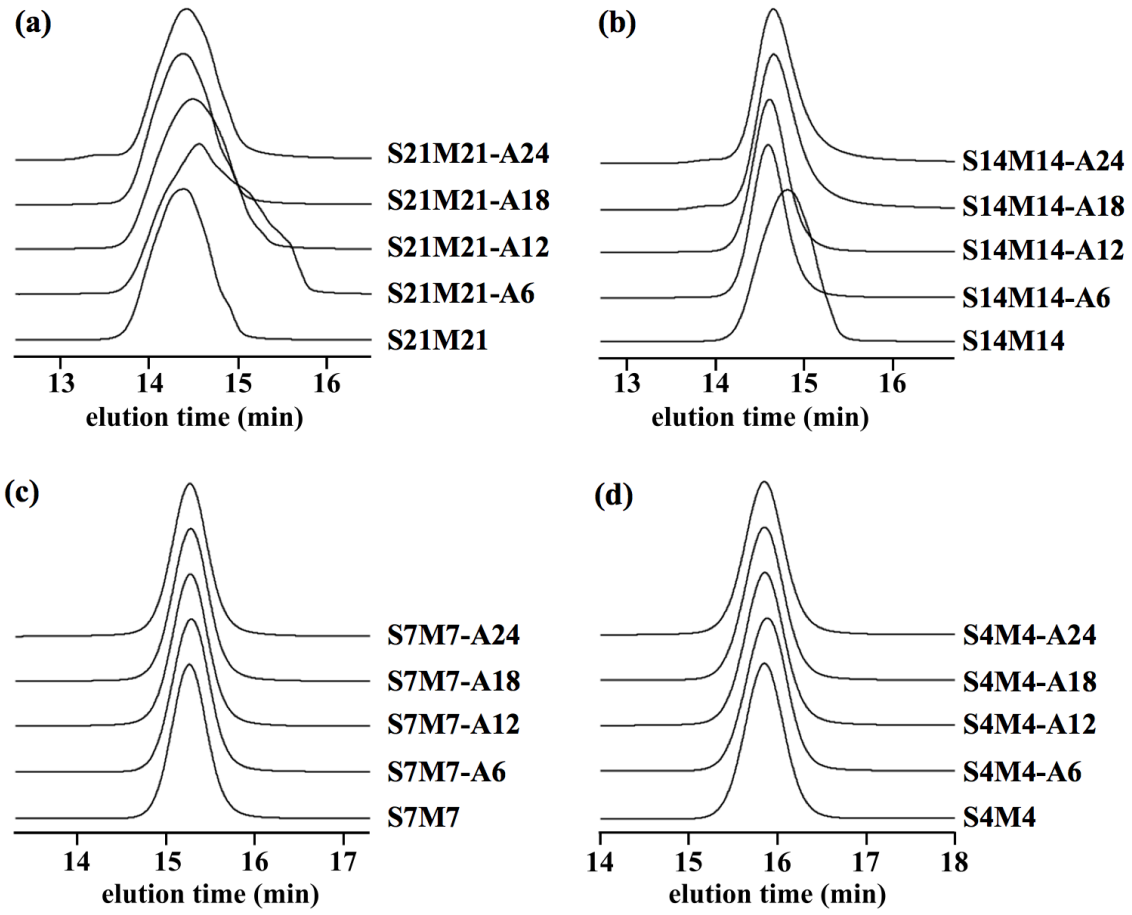


**Figure S2.1**. SEC traces of the ethanolamine-modified PS-*b*-PMMAs (a: **S21M21-AY**, b: **S14M14-AY**, c: **S7M7-AY**, and d: **S4M4-AY**) and the corresponding parent PS-*b*-PMMAs (eluent, THF; flow rate, 1.0 mL $min^{-1}$).

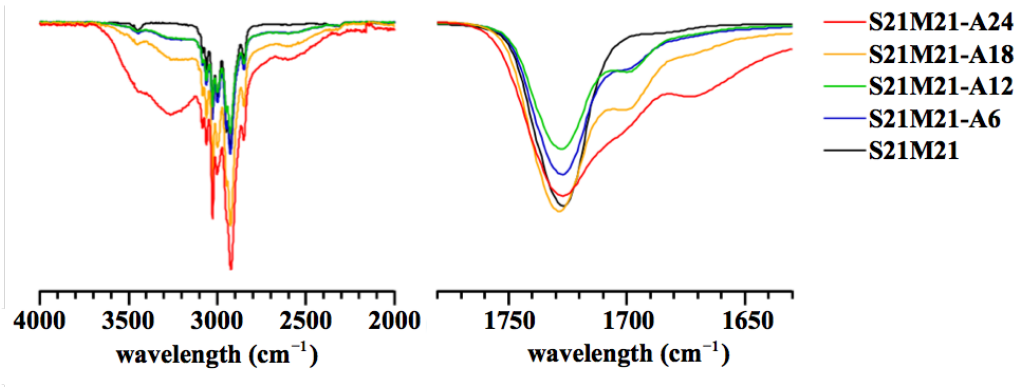


**Figure S2.2**. FT-IR spectra of **S21M21** (black), **S21M21-A6** (blue), **S21M21-A12** (green), **S21M21-A18** (yellow), and **S21M21-A24** (red).

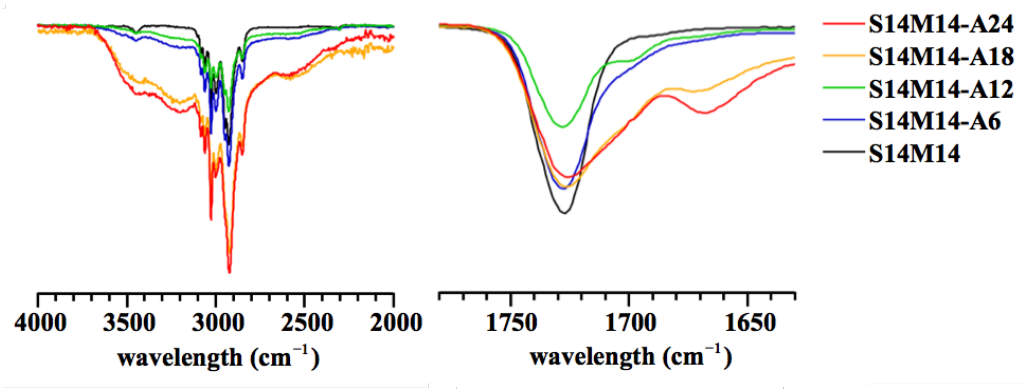


**Figure S2.3**. FT-IR spectra of **S14M14** (black), **S14M14-A6** (blue), **S14M14-A12** (green), **S14M14-A18** (yellow), and **S14M14-A24** (red).

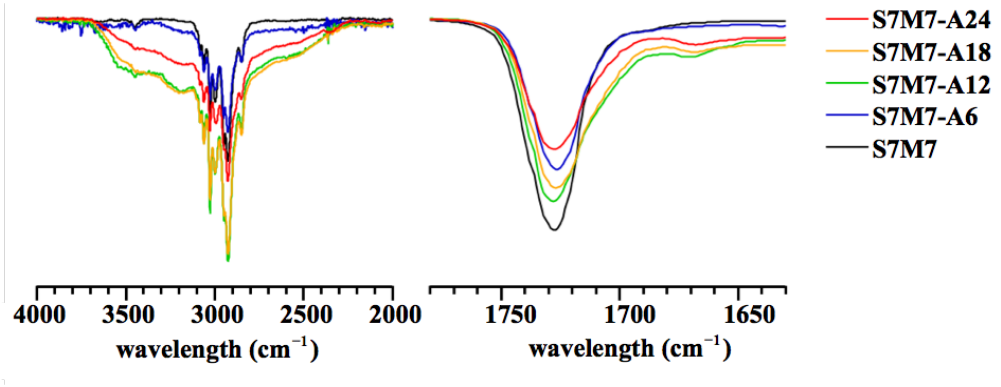


**Figure S2.4**. FT-IR spectra of **S7M7** (black), **S7M7-A6** (blue), **S7M7-A12** (green), **S7M7-A18** (yellow), and **S7M7-A24** (red).

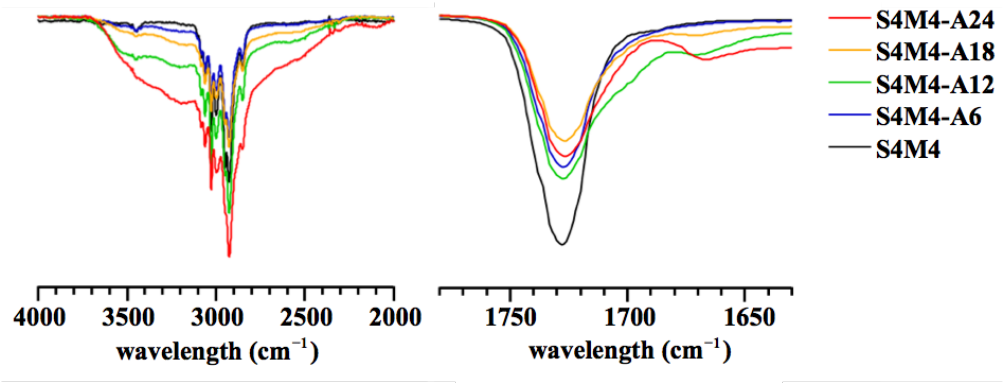


**Figure S2.5**. FT-IR spectra of **S4M4** (black), **S4M4-A6** (blue), **S4M4-A12** (green), **S4M4-A18** (yellow), and **S4M4-A24** (red).

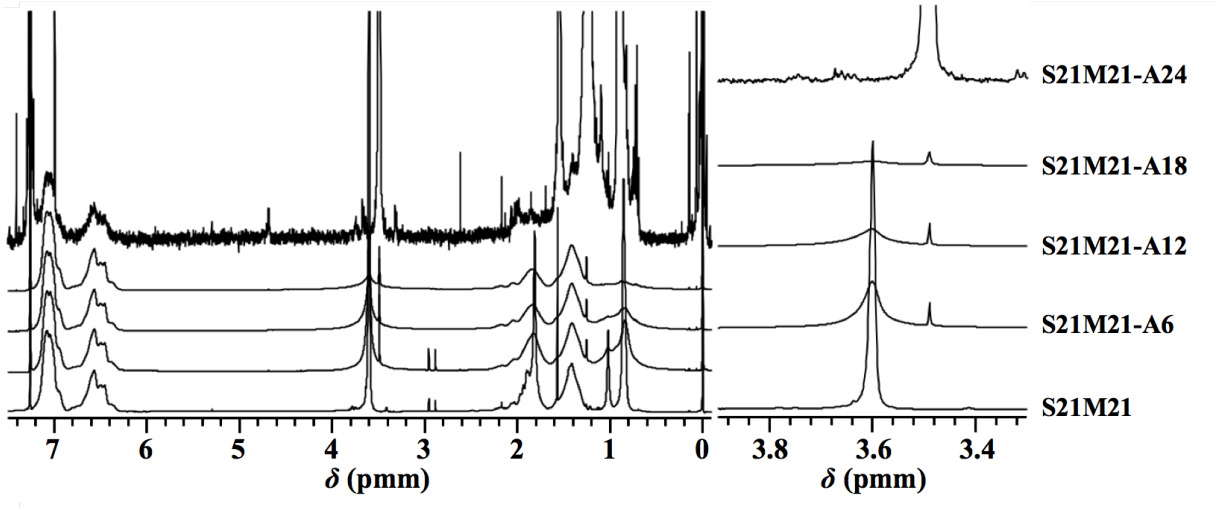


**Figure S2.6**. $^{1}$H NMR spectra of **S21M21**, **S21M21-A6**, **S21M21-A12**, **S21M21-A18**, and **S21M21-A24** in $CDCl_3$ (400 MHz).

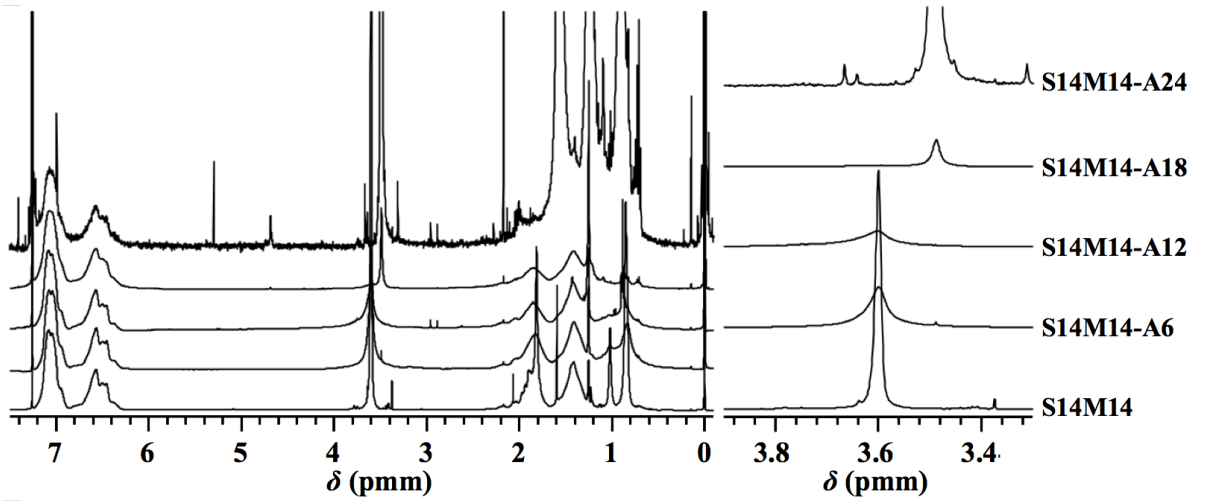


**Figure S2.7**. $^{1}$H NMR spectra of **S14M14**, **S14M14-A6**, **S14M14-A12**, **S14M14-A18**, and **S14M14-A24** in $CDCl_3$ (400 MHz).

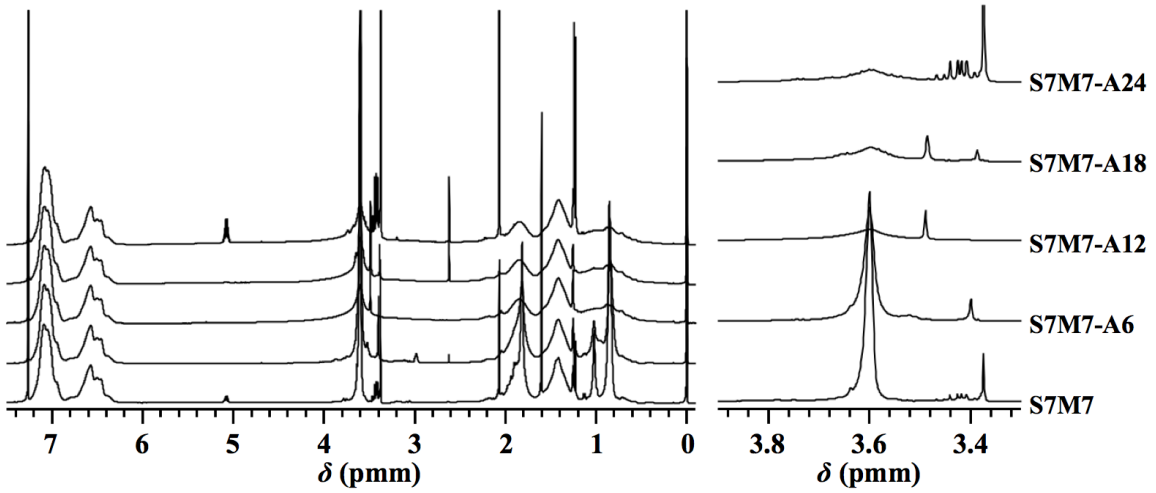


**Figure S2.8**. $^{1}$H NMR spectra of **S7M7**, **S7M7-A6**, **S7M7-A12**, **S7M7-A18**, and **S7M7-A24** in $CDCl_3$ (400 MHz).

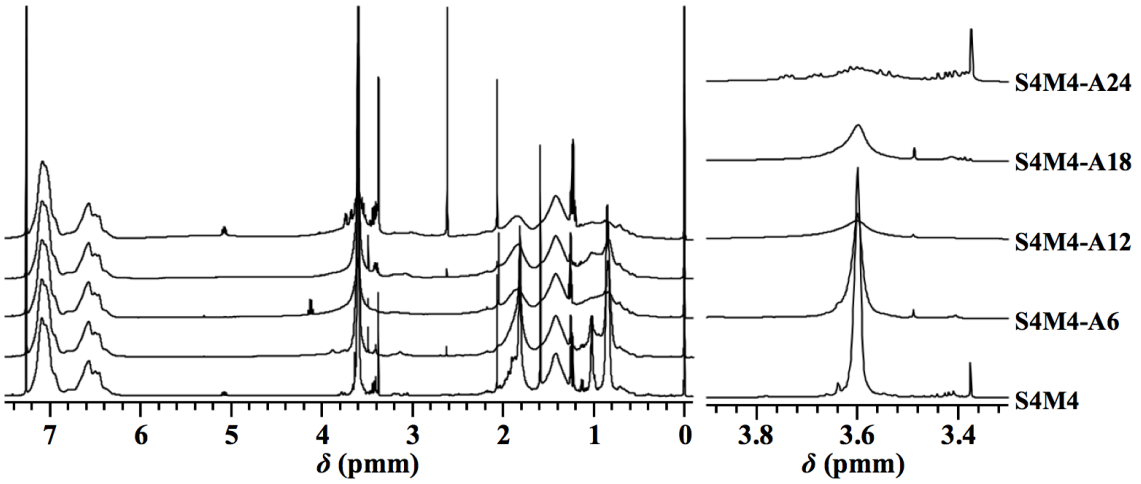


**Figure S2.9**. $^{1}$H NMR spectra of **S4M4**, **S4M4-A6**, **S4M4-A12**, **S4M4-A18**, and **S4M4-A24** in $CDCl_3$ (400 MHz).

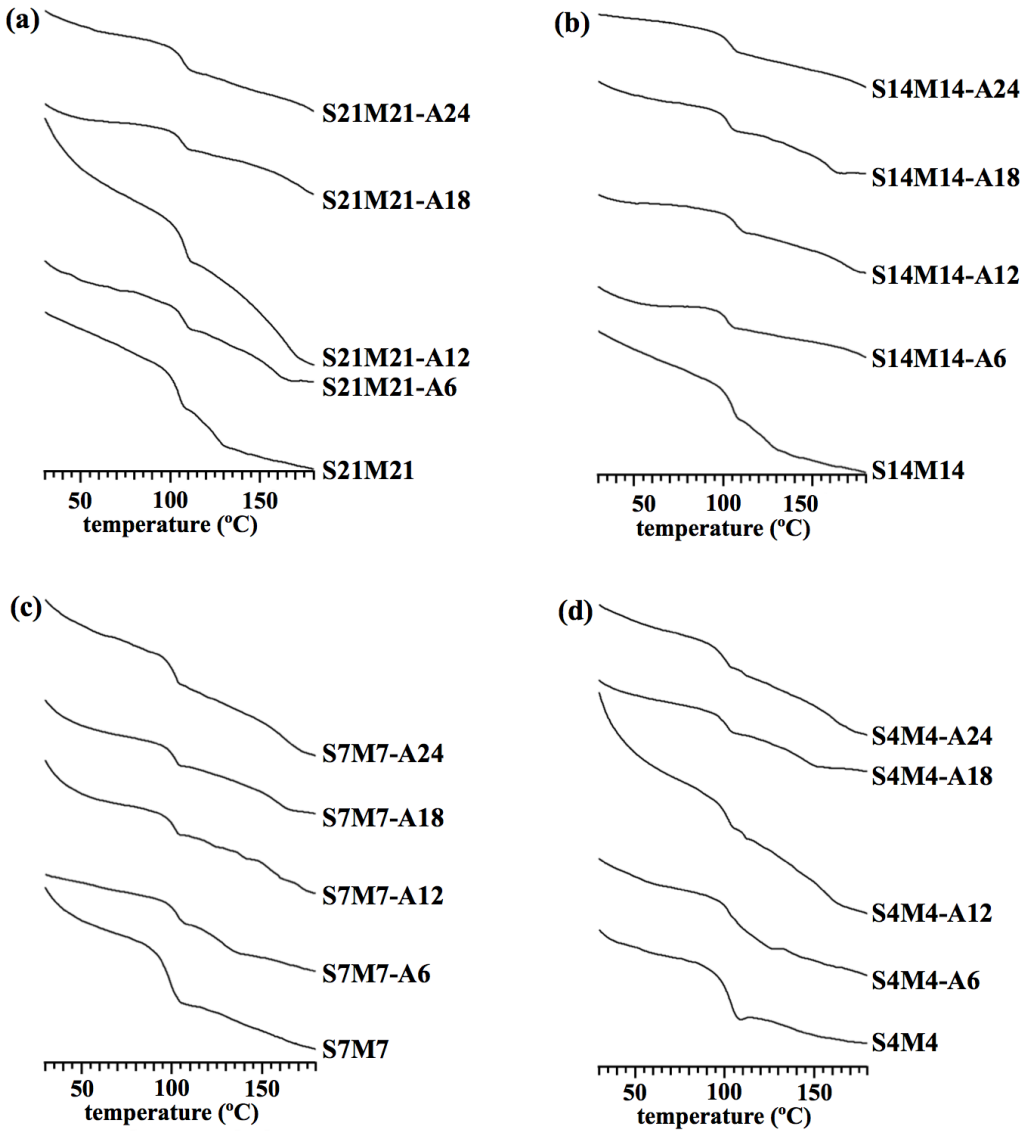


**Figure S2.10**. DSC curves of the ethanolamine-modified PS-*b*-PMMAs (a: **S21M21-AY**, b: **S14M14-AY**, c: **S7M7-AY**, and d: **S4M4-AY**) during second heating under a nitrogen atmosphere at heating rate of 10 °C $min^{-1}$.

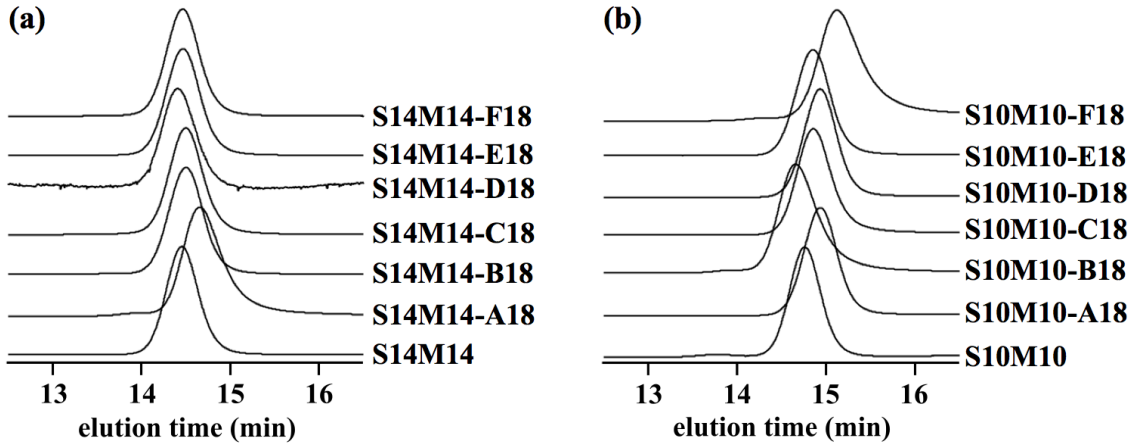


**Figure S2.11**. SEC traces of the various amine-modified PS-*b*-PMMAs (a: **S14M14-X18** and b: **S10M10-X18**) and the corresponding parent PS-*b*-PMMAs (eluent, THF; flow rate, 1.0 mL $min^{-1}$).

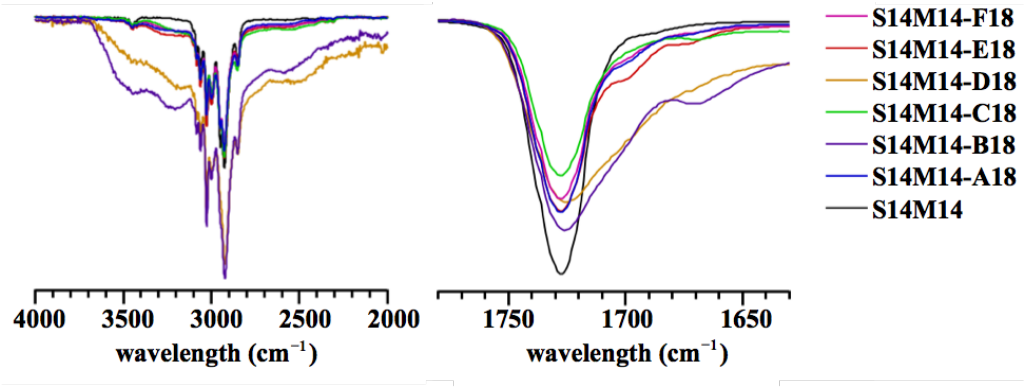


**Figure S2.12**. FT-IR spectra of **S14M14** (black), **S14M14-A18** (blue), **S14M14-B18** (purple), **S14M14-C18** (green), **S14M14-D18** (yellow), **S14M14-E18** (orange), and **S14M14-F18** (red).

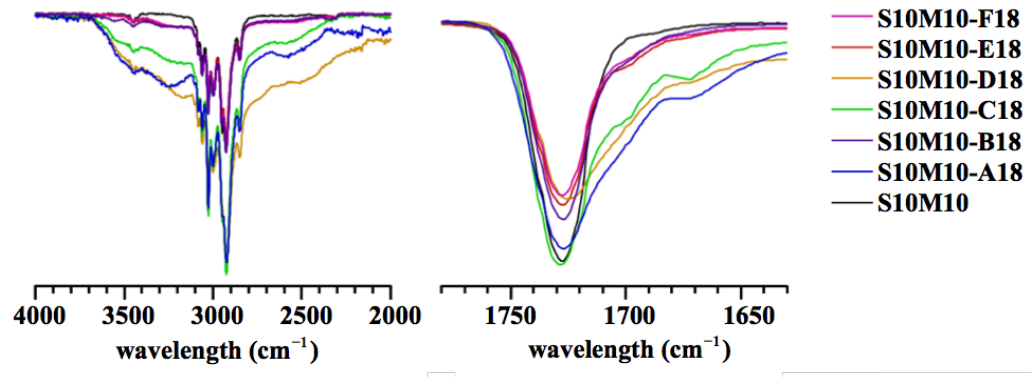


**Figure S2.13** FT-IR spectra of **S10M10** (black), **S10M10-A18** (blue), **S10M10-B18** (purple), **S10M10-C18** (green), **S10M10-D18** (yellow), **S10M10-E18** (orange), and **S10M10-F18** (red).

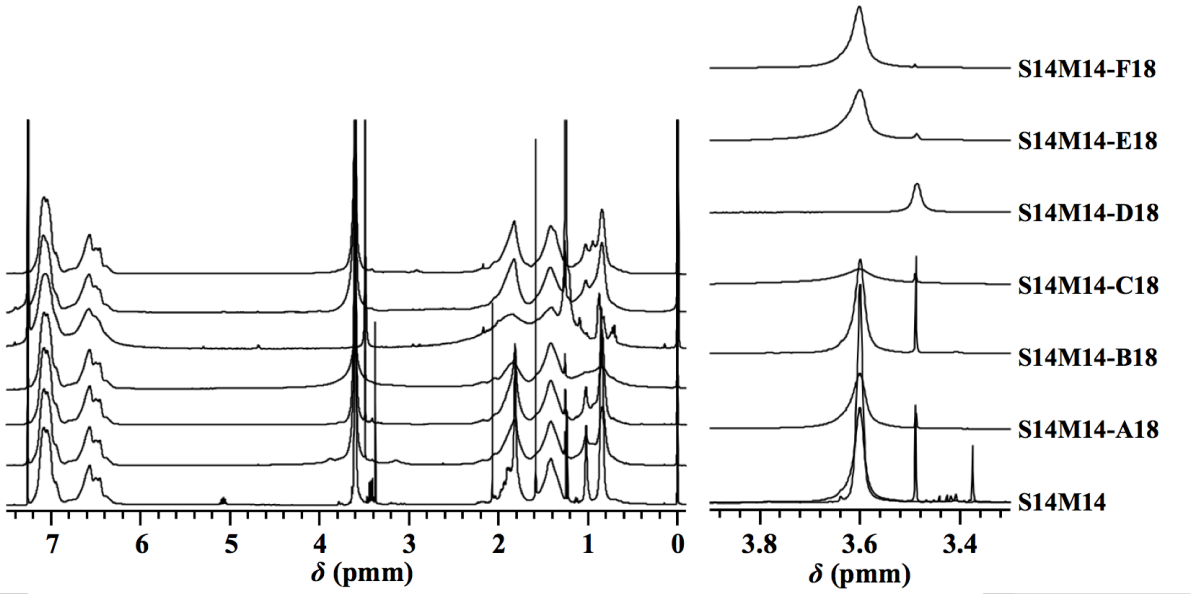


**Figure S2.14**. $^{1}$H NMR spectra of **S14M14**, **S14M14-A18**, **S14M14-B18**, **S14M14-C18**, **S14M14-D18**, **S14M14-E18**, and **S14M14-F18** in $CDCl_3$ (400 MHz).

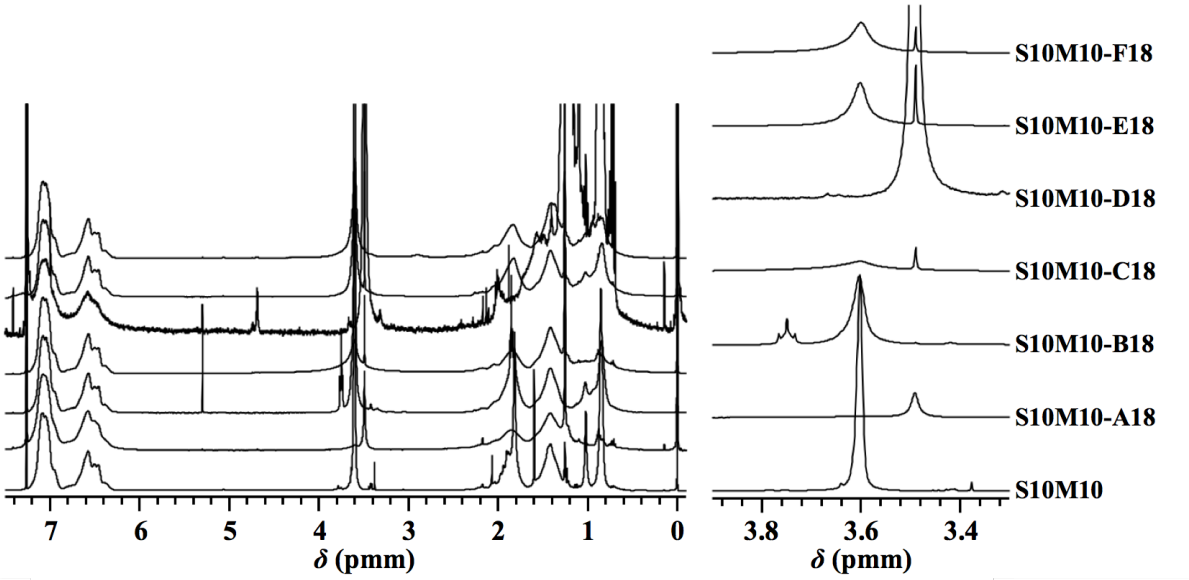


**Figure S2.15**. $^{1}$H NMR spectra of **S10M10**, **S10M10-A18**, **S10M10-B18**, **S10M10-C18**, **S10M10-D18**, **S10M10-E18**, and **S10M10-F18** in $CDCl_3$ (400 MHz).

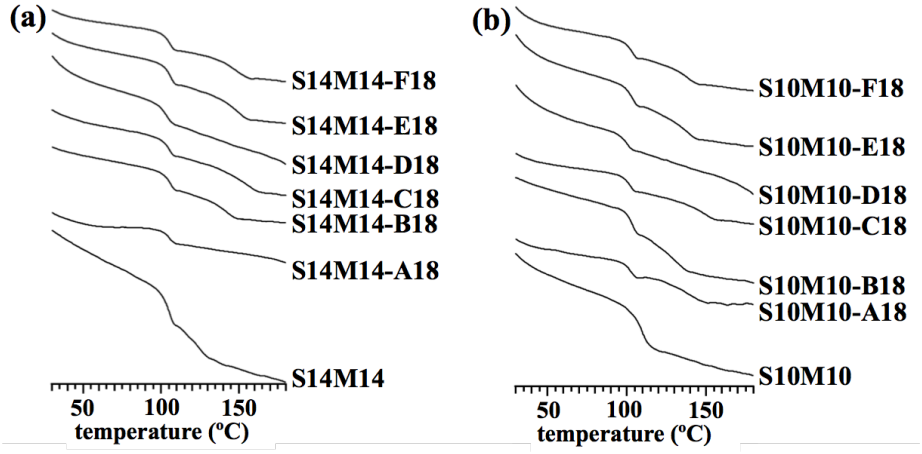


**Figure S2.16**. DSC curves of the various amine-modified PS-*b*-PMMAs (a: **S14M14-X18** and b: **S10M10-X18**) during second heating under a nitrogen atmosphere at heating rate of 10 °C min$^{-1}$.

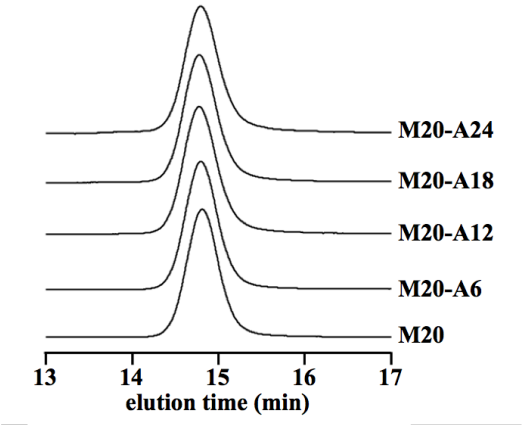


**Figure S2.17**. SEC traces of the **M20**, **M20-A6**, **M20-A12**, **M20-A18**, and **M20-A24** (eluent, THF; flow rate, 1.0 mL $min^{-1}$).

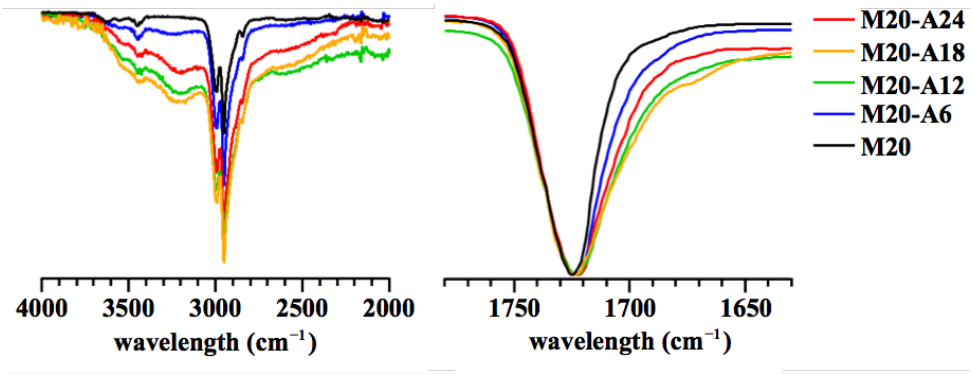


**Figure S2.18**. FT-IR spectra of **M20** (black), **M20-A6** (blue), **M20-A12** (green), **M20-A18** (orange), and **M20-A24** (red).

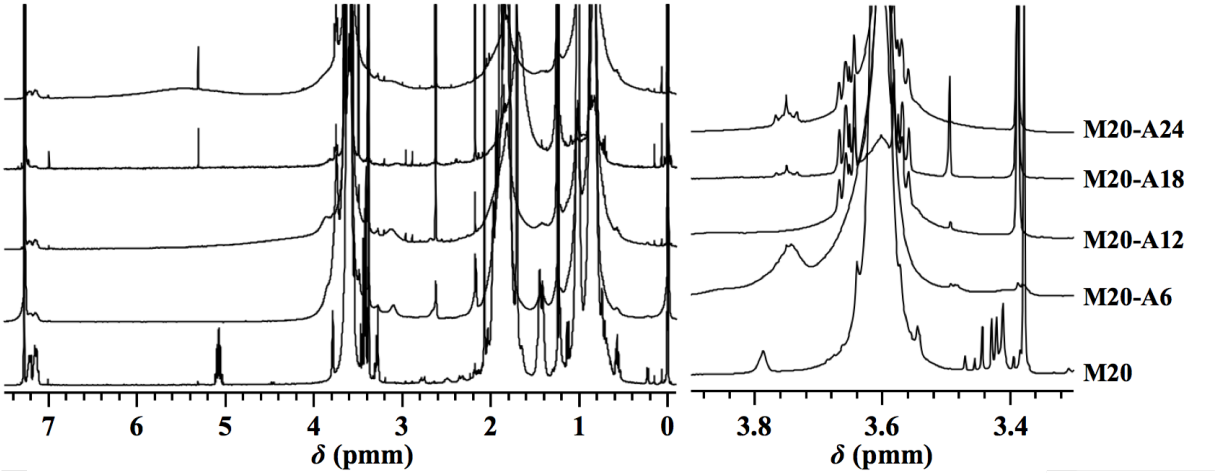


**Figure S2.19**. $^{1}$H NMR spectra of **M20**, **M20-A6**, **M20-A12**, **M20-A18**, and **M20-A24** in $CDCl_3$ (400 MHz).

# *Chapter 3*

## *Terminal-selective Transesterification of Polystyrene-block-Poly(methyl methacrylate) for Chain End Modification*

## 3.1 Introduction

The fine-tuning of the morphology and size of the microphase-separated structures is of great importance for further advancements in the block copolymer (BCP) nanofabrication technologies. While significant efforts have been made to control the BCP microphase separation by various molecular designs including the degree of polymerization ($N$), Flory-Huggins interaction parameter ($\chi$), volume fraction ($f$) related to the monomer composition, dispersity ($Đ$), polymer chain conformation, and polymer architecture, several recent reports have revealed that the modification of the polymer-chain ends as well as the junction points between the two blocks has significant impacts on the BCP self-assembly behaviors.[1–4] For example, Bang's group showed that the incorporation of a short self-attracting units at the junction point between the blocks in the PS-*b*-PMMA enhanced the incompatibility between the blocks.[5] In the study by Park, the three types of polystyrene-*block*-poly(ethylene oxide) (PS-*b*-PEO)-based BCPs having a dissimilar structure at the PEO-chain end showed the microphase separation with the different morphologies, as described in Section 1.2.[6,7] Most importantly, even though the conventional PS-*b*-PEO having a low $N$ showed a less-ordered structure, the incorporation of the highly-polar chain end enabled it to microphase-separate into the ordered structures, suggesting that suitable adjustments of the chain-end structure enhance the incompatibility between the blocks of the BCP. Hence, the author expected that the chain-end modification can be a facile and efficient strategy for fine-tuning the microphase-separated structures of PS-*b*-PMMA. To establish such a morphological control, systematic investigation of the relationship between the various chain-end structures and morphologies in the PS-*b*-PMMA is required.

The chain-end functionalization of PMMA by anionic polymerization relies on the termination reaction at the end of the polymerization.[8–11] The termination reaction using suitable terminators is a powerful tool to give PMMAs and PS-*b*-PMMAs possessing the targeted chain-end group with sufficient fidelity due to the high reactivity of the living chain end. However, it is necessary to conduct a polymerization each time to synthesize the PS-*b*-PMMAs having different chain ends, which causes variations in the $N$ and $Đ$ values among the samples. It would be difficult to extract the pure effect of the chain-end structure on the microphase-separation behaviors. Therefore, the postpolymerization modification strategy should be a

suitable method to obtain a series of PS-*b*-PMMAs with various chain-end structures while retaining the original parameters including $N$ and $Đ$.

Recently, Sawamoto's group reported a novel end-functionalization strategy for PMMA, which is termed "terminal-selective transesterification".[12] In this reaction, a chlorine-terminated PMMA is transesterified only at the terminal MMA units in the presence of the alcohol and the corresponding titanium alkoxide, thereby yielding the chain-end-functionalized PMMA. Importantly, such a terminal selectivity is mainly caused by the lower steric hindrance of the terminal ester than that of the pendant ester in the polymer chain. This suggested that the terminal-selective transesterification can be expandable to the proton-terminated PMMAs and BCP systems bearing PMMA $\omega$-chain ends. Titanium alkoxide is widely used as a catalyst for the transesterification reactions on an industrial scale because of its practical advantages, such as commercial availability, low cost, tolerance to a small amount of water, and the fact that it is easily removed from the system by water addition followed by filtration. In addition, for the transesterification reaction, a broad range of alcohols can be used due to the neutrality of the reaction. Therefore, the terminal-selective transesterification using titanium alkoxides should be a good candidate for the chain-end modifications of PMMA and PS-*b*-PMMA even in industrial areas.

In this chapter, the author aims to establish the terminal-selective transesterification as a platform approach for the facile and efficient chain-end modification of PMMA and PS-*b*-PMMA. A broad range of applicable alcohols for this reaction system enables the incorporation of various functional groups and even polymer segments into the PMMA-chain end. The screening of the chain-end structures of PS-*b*-PMMAs having the same $N$, $f$, and $Đ$ values provides insights into the pure effect of the chain-end structures on the microphase-separation behavior. The PMMA having a molecular weight of 3,300 g mol$^{-1}$ and PS-*b*-PMMA having a molecular weight of 42,000 g mol$^{-1}$ and PS volume fraction of ~0.5 were treated with various alcohols, such as 2-propanol, 1-pentanol, benzyl alcohol, 1-naphthalenemethanol, 1-pyrenemethanol, 1,1,1,3,3,3,-hexafluoro-2-propanol, 4,4,5,5,5-pentafluoropentanol, pentafluorobenzyl alcohol, 6-azido-1-hexanol, ethylene glycol, triethylene glycol monomethyl ether, and poly(ethylene glycol) monomethyl ether. Importantly, the functionalization by the azido-functionalized alcohol endowed the non-living and inactive PMMA-chain ends with a click reactivity leading to the further chain-end modifications. Furthermore, the

transesterification of PS-*b*-PMMA using poly(ethylene glycol) monomethyl ether yielded the triblock terpolymer, i.e., PS-*block*-PMMA-*block*-poly(ethylene glycol) (PS-*b*-PMMA-*b*-PEG), which is a novel methodology for the synthesis of BCPs. A small-angle X-ray scattering (SAXS) analysis revealed the slight difference in the *d* values depending on the chain-end structures even though the ratios of the chain ends to the whole PS-*b*-PMMAs are extremely small (0.31−13wt%).

**Scheme 3.1**. Terminal-selective transesterification of PMMA and PS-*b*-PMMA using titanium alkoxide

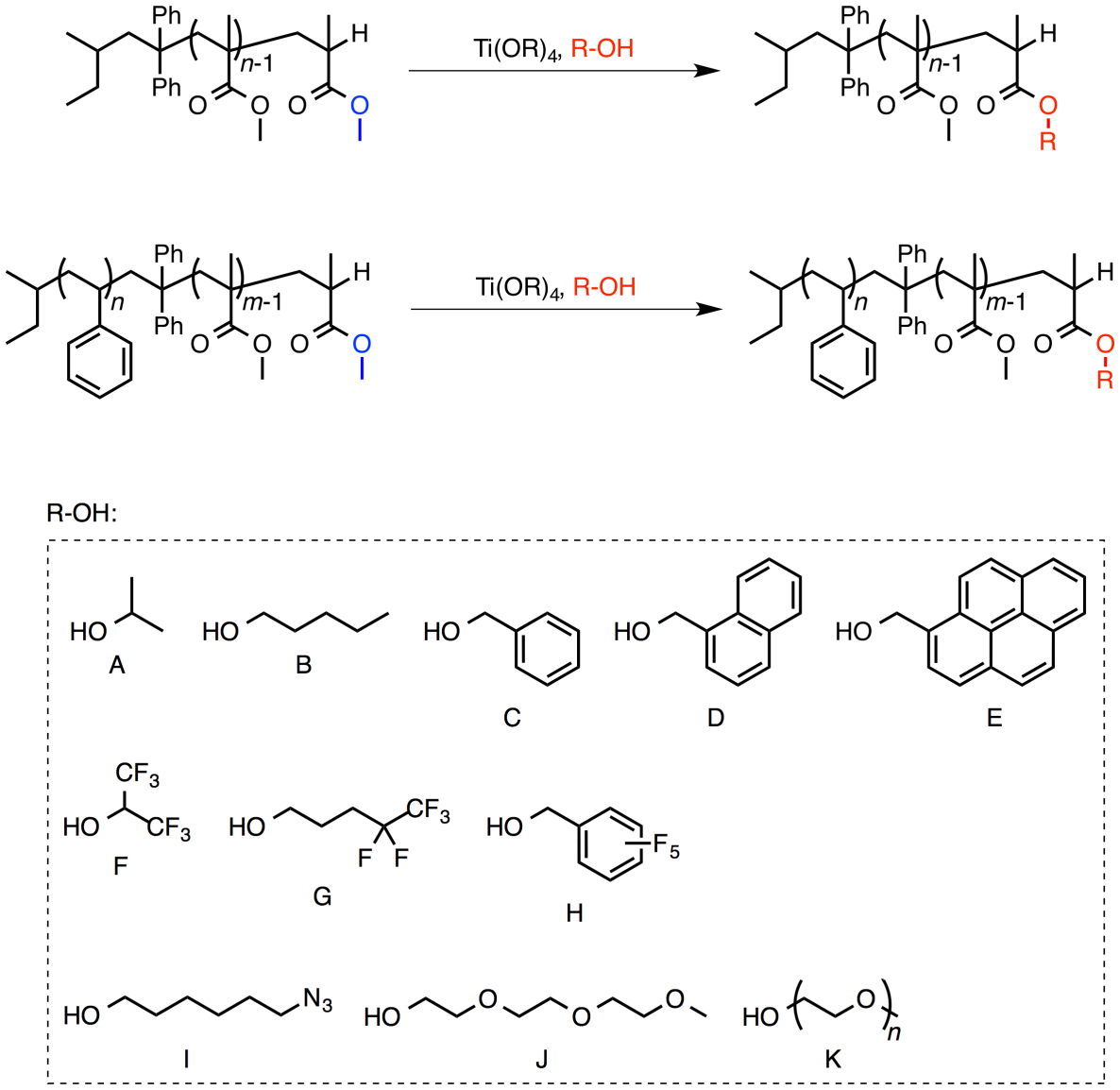

## 3.2 Experimental Section

### *3.2.1 Material*

Titanium isopropoxide (Ti(O*i*Pr)$_4$), 1-pentanol (>99.0%), benzyl alcohol (>99.0%), 1-naphthalenemethanol (>95.0%), 1-pyrenemethanol (>98.0%), 1,1,1,3,3,3-hexafluoro-2-propanol (HFIP; >99.0%), 4,4,5,5,5-pentafluoro-1-pentanol (>93.0%), pentafluorobenzyl alcohol (>96.0%), and triethylene glycol monomethyl ether (>98.0%) were purchased from Tokyo Chemical Industry Co., Ltd., and used as received. Poly(ethylene glycol) monomethyl ether ($M_{n,NMR}$ = 5,450 g mol$^{-1}$, $M_{n,SEC}$ = 8,650, $Đ$ = 1.02) was purchased from Sigma-Aldrich Chemicals Co., and used as received. Ethylene glycol (>99.5%) was purchased from FUJIFILM Wako Pure Chemical Corp., and used as received. Methyl methacrylate (stabilized with 6-*tert*-butyl-2,4-xylenol; >99.8%) was purchased from Tokyo Chemical Industry Co., Ltd., and purified by distillation over calcium hydride. *sec*-Butyllithium (*sec*-BuLi; in cyclohexane and *n*-hexane, 1.0 mol L$^{-1}$) and 2-propanol (>99.5%) were purchased from Kanto Chemical Co., Inc., and used as received. 1,1-Diphenylethylene (DPE; stabilized with hydroquinone; >98.0%) were purchased from Tokyo Chemical Industry Co., Ltd., and purified by distillation over *sec*-BuLi. Lithium chloride (LiCl; >99.0%) was purchased from Kanto Chemical Co., Inc., and used after drying under reduced pressure at 180 °C for 24 h. PS-*b*-PMMA (**S21M21**, 42,000 g mol$^{-1}$, $f_{PS}$ = 0.54) was provided in the form of propylene glycol methyl ether acetate (PGMEA) solutions by Tokyo Ohka Kogyo Co., Ltd., and precipitated in methanol and dried prior to use. The cellophane tube (Spectra/por® 6 Membrane; MWCO: 1,000) was purchased from Spectrum Laboratories and washed with water and methanol before use. The cation-exchange resin (Dowex® 50WX2, hydrogen form, 50-100 mesh) was purchased from Sigma-Aldrich Chemicals Co., and washed with methanol before use.

### *3.2.2 Characterization*

The SEC experiments were performed at 40 °C using a Shodex GPC-101 gel-permeation chromatography system (Shodex DU-2130 dual pump, Shodex RI-71 reflective index detector, and Shodex ERC-3125SN degasser) equipped with a Shodex KF-G guard column (4.6 mm × 10 mm; particle size, 8 μm) and two Shodex KF-804L columns (linear, 8 mm × 300 mm linear; particle size, 5 μm; exclusion limit, 4 ×

$10^6$) in THF at a flow rate of 1.0 mL $min^{-1}$. The number-average molecular weight ($M_{n,SEC}$) and dispersity ($Đ$) values were calculated using PS standards for PS-*b*-PMMAs and PMMA standards for the PMMAs. $^1$H NMR (400 MHz) spectra were recorded using a JEOL JNM-ECS400 instrument. Matrix-assisted laser desorption ionization time-of-flight mass spectrometry (MALDI-TOF MS) of the polymers was performed using an Applied Biosystems ABSCIEX MALDI TOF/TOF 5800 instrument in reflector mode (for PMMA samples). The samples were prepared by depositing a mixture of the polymer, matrix, and cationic agent in THF onto a sample plate. A 5:5:1 (v/v) ratio of [PMMA (1.0 g $L^{-1}$ in THF)]/[dithranol (40 g $L^{-1}$ in THF)]/[sodium trifluoroacetate (5.0 g $L^{-1}$ in THF)] was used for the sample preparation.

### *3.2.3 Anionic Polymerization of Methyl Methacrylate*

*sec*-BuLi (0.98 mol $L^{-1}$, 2.57 mL, 2.52 mmol), DPE (664 μL, 3.78 mmol), and a solution of LiCl in THF (500 mmol $L^{-1}$, 7.55 mL, 3.78 mmol) were sequentially added to THF (132 mL) at −78 °C, and the mixture was stirred for 30 min. Methyl methacrylate (MMA; 8.00 mL, 75.5 mmol) was added to the mixture and polymerization was terminated after 1 h by the addition of a small amount of methanol. The mixture was diluted with THF and passed through a short column of alumina. After removal of the solvent, the crude product was dialyzed with a cellophane tube (Spectra/Por® 6 Membrane; MWCO: 1,000) in acetone and finally precipitated three times from THF solution into hexane to give PMMA (**M3**) as white powder (Yield: 38.6%; $M_{n,NMR}$ = 3,300 g $mol^{-1}$; $M_{n,SEC}$ = 3,760 g $mol^{-1}$, $Đ$ = 1.08 (THF)). $^1$H NMR ($CDCl_3$): $\delta$ 7.32−7.08 (br, 10H, aromatic), 3.82−3.38 (br, −OC$H_3$), 2.49 (br, $\omega$-terminal, −C$H$($CH_3$)COO−), 2.24−1.36 (br, main chain −C$H_2$C−), 0.59−0.52 (m, 6H, $\alpha$-terminal −C$H_3$, −$CH_2$C$H_3$).

### *3.2.4 Terminal-Selective Transesterification of PMMA and PS-b-PMMA using Titanium Alkoxides*

**Transesterification of M3 with 2-Propanol**

The following is a typical terminal-selective transesterification procedure (Procedure A): Ti(O*i*Pr)$_4$ (81.1 μL, 277 μmol), 2-propanol (137 μL, 3.69 mmol), **M3** (300 mg, 92.3 μmol) and toluene (5.43 mL) were added to a Schlenk flask under an argon atmosphere. The mixture was stirred at 100 °C for 24 h. After cooling to room temperature, a small amount of water was added. The mixture was further stirred for

30 min, then diluted with THF, and filtrated using a membrane filter (0.45 μm pore size) to remove the catalyst as titanium oxide. After evaporating the solvent, the residue was dialyzed using a cellophane tube (Spectra/Por® 6 Membrane; MWCO: 1,000) against acetone and finally reprecipitated from THF solution into hexane to give **M3-A** as a white powder. Yield: 47.7%. $M_{n,NMR}$ = 3,290 g mol$^{-1}$, $M_{n,SEC}$ = 4,080 g mol$^{-1}$, $Đ$ = 1.06 (THF). $^1$H NMR (400 MHz, $CDCl_3$): $\delta$ 7.25−7.08 (br, 10H, −C(*Ph*)$_2$), 4.94 (m, $J$ = 6.2 Hz, $\omega$-terminal, 1H, −OC*H*(CH$_3$)$_2$), 3.60 (−OC*H*$_3$, PMMA), 2.42 (br, $\omega$-terminal, 1H, −C*H*(CH$_3$)COO−), 0.60−2.12 (br, main chain −C*H*$_2$C−, −CC*H*$_3$), 0.59−0.52 (m, 6H, $\alpha$-terminal −C*H*$_3$, −CH$_2$C*H*$_3$).

**Transesterification of S21M21 with 2-Propanol**

By following the Procedure A, the transesterification of **S21M21** (500 mg, 11.9 μmol) with 2-propanol (17.7 μL, 476 mmol) was performed using Ti(O*i*Pr)$_4$ (10.5 μL, 35.7 μmol) in toluene (3.00 mL) to give **S21M21-A** as a white powder. Yield: 23.2%. $M_{n,SEC}$ = 35,200 g mol$^{-1}$, $Đ$ = 1.03 (THF). $^1$H NMR (400 MHz, $CDCl_3$): $\delta$ 7.32−6.26 (br, aromatic), 4.94 (m, $J$ = 6.4 Hz, $\omega$-terminal, 1H, −OC*H*(CH$_3$)$_2$), 3.82−3.38 (br, −OC*H*$_3$, PMMA), 2.42 (br, $\omega$-terminal, 1H, −C*H*(CH$_3$)COO−), 2.24−0.77 (br, main chain −C*H*$_2$C−, −CC*H*$_3$, −C*H*$_2$C*H*−, −C*H*$_2$C*H*−, PMMA, PS).

**Transesterification of M3 with 1-Pentanol**

The following is a typical terminal-selective transesterification procedure (Procedure B): Ti(O*i*Pr)$_4$ (81.1 μL, 277 μmol), 1-pentanol (200 μL, 1.85 mmol), and toluene (1.00 mL) were added to a Schlenk flask an under argon atmosphere. The mixture was stirred at 80 °C for 1 h and then cooled with liquid nitrogen. The solvent and the 2-propanol generated from Ti(O*i*Pr)$_4$ were removed by evaporation under high vacuum, to yield the titanium alkoxide of 1-propanol. A solution of **M3** (300 mg, 92.3 μmol) and 1-pentanol (200 μL, 1.85 mmol) in toluene (5.43 mL) was added to the Schlenk flask containing the titanium alkoxide. then the mixture was stirred at 100 °C for 24 h. After cooling to room temperature, a small amount of water was added. The mixture was stirred for 30 min, then diluted with THF, and filtrated using a membrane filter (0.45 μm pore size) to remove the catalyst as titanium oxide. After evaporating the solvent, the residue was dialyzed using a cellophane tube (Spectra/Por® 6 Membrane; MWCO: 1,000) against acetone and finally reprecipitated from THF solution into hexane to give **M3-B** as a white powder. Yield: 51.3%. $M_{n,NMR}$ = 3,290 g mol$^{-1}$, $M_{n,SEC}$ = 4,040 g mol$^{-1}$, $Đ$ = 1.06 (THF). $^1$H NMR (400 MHz, $CDCl_3$): $\delta$ 7.25−7.08 (br, 10H,

−C(*Ph*)$_2$−), 4.02 (m, *ω*-terminal, 2H, −OC*H*$_2$(CH$_2$)$_3$CH$_3$), 3.60 (−OC*H*$_3$, PMMA), 2.47 (br, *ω*-terminal, −C*H*(CH$_3$)COO−), 0.60−2.12 (br, main chain −C*H*$_2$C−, −CC*H*$_3$), 0.59−0.52 (m, 6H, *α*-terminal −C*H*$_3$, −CH$_2$C*H*$_3$).

**Transesterification of S21M21 with 1-Pentanol**

By following the Procedure B, the transesterification of **S21M21** (500 mg, 11.9 μmol) with 1-pentanol (25.8 μL, 238 mmol) was performed using the titanium alkoxide, which had been prepared from Ti(O*i*Pr)$_4$ (10.5 μL, 35.7 μmol) and 1-pentanol (25.8 μL, 238 mmol) in toluene (1.00 mL), in toluene (3.00 mL) to give **S21M21-B** as a white powder. Yield: 79.0%. $M_{n,SEC}$ = 36,700 g mol$^{-1}$, $Đ$ = 1.03 (THF). $^1$H NMR (400 MHz, CDCl$_3$): $\delta$ 7.32−6.26 (br, aromatic), 4.02 (m, *ω*-terminal, 2H, −OC*H*$_2$(CH$_2$)$_3$CH$_3$), 3.82−3.38 (br, −OC*H*$_3$, PMMA), 2.47 (br, *ω*-terminal, −C*H*(CH$_3$)COO−), 2.24−0.77 (br, main chain −C*H*$_2$C−, −CC*H*$_3$, −C*H*$_2$C*H*−, −C*H*$_2$C*H*−, PMMA, PS).

**Transesterification of M3 with Benzyl Alcohol**

By following the Procedure B, the transesterification of M3 (300 mg, 92.3 μmol) with benzyl alcohol (123 μL, 1.85 mmol) was performed using the titanium alkoxide, which had been prepared from Ti(O*i*Pr)$_4$ (81.1 μL, 277 μmol) and benzyl alcohol (123 μL, 1.85 mmol) in toluene (1.00 mL), in toluene (3.00 mL) to give **M3-C** as a white powder. Yield: 48.3%. $M_{n,NMR}$ = 3,340 g mol$^{-1}$, $M_{n,SEC}$ = 4,090 g mol$^{-1}$, $Đ$ = 1.06 (THF). $^1$H NMR (400 MHz, CDCl$_3$): $\delta$ 7.37 (br, *ω*-terminal, 5H, −OCH$_2$*Ph*), 7.25−7.08 (br, 10H, −C(*Ph*)$_2$−), 5.07 (m, *ω*-terminal, 2H, −OC*H*$_2$Ph), 3.60 (−OC*H*$_3$, PMMA), 2.53 (br, *ω*-terminal, −C*H*(CH$_3$)COO−), 0.60−2.12 (br, main chain −C*H*$_2$C−, −CC*H*$_3$), 0.59−0.52 (m, 6H, *α*-terminal −C*H*$_3$, −CH$_2$C*H*$_3$).

**Transesterification of S21M21 with Benzyl Alcohol**

By following the Procedure B, the transesterification of **S21M21** (500 mg, 11.9 μmol) with benzyl alcohol (15.9 μL, 238 mmol) was performed using the titanium alkoxide, which had been prepared from Ti(O*i*Pr)$_4$ (10.5 μL, 35.7 μmol) and benzyl alcohol (15.9 μL, 238 mmol) in toluene (1.00 mL), in toluene (3.00 mL) to give **S21M21-C** as a white powder. Yield: 62.2%. $M_{n,SEC}$ = 35,400 g mol$^{-1}$, $Đ$ = 1.03 (THF). $^1$H NMR (400 MHz, CDCl$_3$): $\delta$ 7.37 (br, *ω*-terminal, 5H, −OCH$_2$*Ph*), 7.32−6.26 (br, aromatic), 5.07 (m, *ω*-

terminal, 2H, −OC$H_2$Ph), 3.82−3.38 (br, −OC$H_3$, PMMA), 2.54 (br, $\omega$-terminal, −C$H$(CH$_3$)COO−), 2.24−0.77 (br, main chain −C$H_2$C−, −CC$H_3$, −C$H_2$C$H$−, −C$H_2$C$H$−, PMMA, PS).

**Transesterification of M3 with 1-Naphthalenemethanol**

The following is a typical terminal-selective transesterification procedure (Procedure C): Ti(O*i*Pr)$_4$ (81.1 μL, 277 μmol), 1-naphthalenemethanol (583 mL, 3.69 mmol), and toluene (1.00 mL) were added to a Schlenk flask under an argon atmosphere. The mixture was stirred at 80 °C for 1 h and then cooled with liquid nitrogen. The solvent and the 2-propanol generated from the Ti(O*i*Pr)$_4$ were removed by evaporation under high vacuum, to yield the corresponding titanium alkoxide. A solution of **M3** (300 mg, 92.3 μmol) in toluene (5.43 mL) was added to the Schlenk flask containing the titanium alkoxide, then the mixture was stirred at 100 °C for 24 h. After cooling to room temperature, a small amount of water was added. The mixture was stirred for 30 min, then diluted with THF and filtrated using a membrane filter (0.45 μm pore size) to remove the catalyst as titanium oxide. After evaporating the solvent, the residue was dialyzed using a cellophane tube (Spectra/Por® 6 Membrane; MWCO: 1,000) against acetone and finally reprecipitated from THF solution into hexane to give **M3-D** as a white powder. Yield: 40.0%. $M_{n,NMR}$ = 3,060 g mol$^{-1}$, $M_{n,SEC}$ = 3,890 g mol$^{-1}$, $Đ$ = 1.07 (THF). $^1$H NMR (400 MHz, CDCl$_3$): $\delta$ 7.91−7.70 (br, 3H, naphthalene), 7.55−7.40 (br, 3H, naphthalene), 7.25−7.08 (br, 10H, −C(*Ph*)$_2$−), 5.23 (m, $\omega$-terminal, 2H, −OC$H_2$−naphthalene), 3.60 (−OC$H_3$, PMMA), 2.56 (br, $\omega$-terminal, −C$H$(CH$_3$)COO−), 0.60−2.12 (br, main chain −C$H_2$C−, −CC$H_3$), 0.59−0.52 (m, $\alpha$-terminal −C$H_3$, −CH$_2$C$H_3$).

**Transesterification of S21M21 with 1-Naphthalenemethanol**

By following the Procedure C, the transesterification of **S21M21** (500 mg, 11.9 μmol) with 1-naphthalenemethanol (75.3 mg, 476 mmol) was performed using Ti(O*i*Pr)$_4$ (10.5 μL, 35.7 μmol) in toluene (3.00 mL) to give **S21M21-D** as a white powder. Yield: 66.2%. $M_{n,SEC}$ = 37,000 g mol$^{-1}$, $Đ$ = 1.03 (THF). $^1$H NMR (400 MHz, CDCl$_3$): $\delta$ 7.91−7.70 (br, 3H, naphthalene), 7.55−7.40 (br, 3H, naphthalene), 7.32−6.26 (br, aromatic), 5.23 (m, $\omega$-terminal, 2H, −OC$H_2$−naphthalene), 3.82−3.38 (br, −OC$H_3$, PMMA), 2.57 (br, $\omega$-terminal, −C$H$(CH$_3$)COO−), 2.24−0.77 (br, main chain −C$H_2$C−, −CC$H_3$, −C$H_2$C$H$−, −C$H_2$C$H$−, PMMA, PS).

**Transesterification of M3 with 1-Pyrenemethanol**

By following the Procedure C, the transesterification of **M3** (300 mg, 92.3 μmol) with 1-pyrenemethanol (81.1 μL, 277 μmol) was performed using Ti(O*i*Pr)$_4$ (10.5 μL, 35.7 μmol) in toluene (5.43mL) to give **M3-E** as a white powder. Yield: 67.0%. $M_{n,NMR}$ = 3,410 g mol$^{-1}$, $M_{n,SEC}$ = 3,770 g mol$^{-1}$, $Đ$ = 1.07 (THF). $^1$H NMR (400 MHz, $CDCl_3$): $\delta$ 8.43−8.00 (br, 9H, pyrene), 7.25−7.08 (br, 10H, −C(*Ph*)$_2$−), 5.80 (m, $\omega$-terminal, 2H, −OC*H*$_2$−pyrene), 3.60 (−OC*H*$_3$, PMMA), 2.55 (br, $\omega$-terminal, −C*H*(CH$_3$)COO−), 0.60−2.12 (br, main chain −C*H*$_2$C−, −CC*H*$_3$), 0.59−0.52 (m, 6H, $\alpha$-terminal −C*H*$_3$, −CH$_2$C*H*$_3$).

**Transesterification of S21M21 with 1-Pyrenemethanol**

By following the Procedure C, the transesterification of **S21M21** (500 mg, 11.9 μmol) with 1-pyrenemethanol (75.3 mg, 476 mmol) was performed using Ti(O*i*Pr)$_4$ (10.5 μL, 35.7 μmol) in toluene (3.00 mL) to give **S21M21-E** as a white powder. Yield: 76.2%. $M_{n,SEC}$ = 36,300 g mol$^{-1}$, $Đ$ = 1.03 (THF). $^1$H NMR (400 MHz, $CDCl_3$): $\delta$ 7.32−6.26 (br, aromatic), 3.82−3.38 (br, −OC*H*$_3$, PMMA), 2.24−0.77 (br, main chain −C*H*$_2$C−, −CC*H*$_3$, −C*H*$_2$C*H*−, −C*H*$_2$C*H*−, PMMA, PS).

**Transesterification of M3 with HFIP**

By following the Procedure B, the transesterification of **M3** (300 mg, 92.3 μmol) with HFIP (192 μL, 1.85 mmol) was performed using the titanium alkoxide, which had been prepared from Ti(O*i*Pr)$_4$ (81.1 μL, 277 μmol) and HFIP (192 μL, 1.85 mmol) in toluene (1.00 mL), in toluene (5.43 mL) to give **M3-F**. The reaction progress was monitored by MALDI-TOF mass analysis.

**Transesterification of M3 with 4,4,5,5,5-Pentafluoro-1-pentanol**

By following the Procedure B, the transesterification of **M3** (300 mg, 92.3 μmol) with 4,4,5,5,5-pentafluoro-1-pentanol (244 μL, 1.85 mmol) was performed using the titanium alkoxide, which had been prepared from Ti(O*i*Pr)$_4$ (81.1 μL, 277 μmol) and 4,4,5,5,5-pentafluoro-1-pentanol (244 μL, 1.85 mmol) in toluene (1.00 mL), in toluene (5.43 mL) to give **M3-G** as a white powder. Yield: 19.7%. $M_{n,NMR}$ = 3,430 g mol$^{-1}$, $M_{n,SEC}$ = 4,280 g mol$^{-1}$, $Đ$ = 1.05 (THF). $^1$H NMR (400 MHz, $CDCl_3$): $\delta$ 7.25−7.08 (br, 10H, −C(*Ph*)$_2$−), 4.10 (m, $\omega$-terminal, 2H, −OC*H*$_2$(CH$_2$)$_2$CF$_2$CF$_3$), 3.60 (−OC*H*$_3$, PMMA), 2.50 (br, $\omega$-terminal, −C*H*(CH$_3$)COO−), 2.16 (m, $\omega$-terminal, 2H, −O (CH$_2$)$_2$C*H*$_2$CF$_2$CF$_3$), 0.60−2.12 (br, main chain −C*H*$_2$C−, −CC*H*$_3$), 0.59−0.52 (m, 6H, $\alpha$-terminal −C*H*$_3$, −CH$_2$C*H*$_3$).

**Transesterification of S21M21 with 4,4,5,5,5-Pentafluoro-1-pentanol**

By following the Procedure B, the transesterification of **S21M21** (500 mg, 11.9 μmol) with 4,4,5,5,5-pentafluoro-1-pentanol (31.4 μL, 238 mmol) was performed using the titanium alkoxide, which had been prepared from Ti(O*i*Pr)$_4$ (10.5 μL, 35.7 μmol) and 4,4,5,5,5-pentafluoro-1-pentanol (31.4 μL, 238 mmol) in toluene (1.00 mL), in toluene (5.43 mL) to give **S21M21-G** as a white powder. Yield: 47.4%. $M_{n,SEC}$ = 36,000 g mol$^{-1}$, $Đ$ = 1.03 (THF). $^1$H NMR (400 MHz, $CDCl_3$): $\delta$ 7.32−6.26 (br, aromatic), 4.10 (m, $\omega$-terminal, 2H, −OC*H*$_2$(CH$_2$)$_2$CF$_2$CF$_3$), 3.82−3.38 (br, −OC*H*$_3$, PMMA), 2.50 (br, $\omega$-terminal, −C*H*(CH$_3$)COO−), 2.24−0.77 (br, main chain −C*H*$_2$C−, −CC*H*$_3$, −C*H*$_2$C*H*−, −C*H*$_2$C*H*−, PMMA, PS).

**Transesterification of M3 with Pentafluorobenzyl Alcohol**

By following the Procedure C, the transesterification of **M3** (300 mg, 92.3 μmol) with pentafluorobenzyl alcohol (731 mg, 3.69 mmol) was performed using Ti(O*i*Pr)$_4$ (81.1 μL, 277 μmol) in toluene (5.43 mL) to give **M3-H** as a white powder. Yield: 47.7%. $M_{n,NMR}$ = 3,370 g mol$^{-1}$, $M_{n,SEC}$ = 4,040 g mol$^{-1}$, $Đ$ = 1.06 (THF). $^1$H NMR (400 MHz, $CDCl_3$): $\delta$ 7.25−7.08 (br, 10H, −C(*Ph*)$_2$−), 5.15 (m, $\omega$-terminal, 2H, −OC*H*$_2$C$_5$F$_5$), 3.60 (−OC*H*$_3$, PMMA), 2.50 (br, $\omega$-terminal, −C*H*(CH$_3$)COO−), 0.60−2.12 (br, main chain −C*H*$_2$C−, −CC*H*$_3$), 0.59−0.52 (m, 6H, $\alpha$-terminal −C*H*$_3$, −CH$_2$C*H*$_3$).

**Transesterification of S21M21 with Pentafluorobenzyl Alcohol**

By following the Procedure C, the transesterification of **S21M21** (500 mg, 11.9 μmol) with pentafluorobenzyl alcohol (94.3 mg, 476 mmol) was performed using Ti(O*i*Pr)$_4$ (10.5 μL, 35.7 μmol) in toluene (3.00 mL) to give **S21M21-H** as a white powder. Yield: 39.8%. $M_{n,SEC}$ = 37,500 g mol$^{-1}$, $Đ$ = 1.03 (THF). $^1$H NMR (400 MHz, $CDCl_3$): $\delta$ 7.32−6.26 (br, aromatic), 5.07 (m, $\omega$-terminal, 2H, −OC*H*$_2$C$_5$F$_5$), 3.82−3.38 (br, −OC*H*$_3$, PMMA), 2.54 (br, $\omega$-terminal, −C*H*(CH$_3$)COO−), 2.24−0.77 (br, main chain −C*H*$_2$C−, −CC*H*$_3$, −C*H*$_2$C*H*−,−C*H*$_2$C*H*−, PMMA, PS).

**Transesterification of M3 with 6-Azido-1-hexanol**

By following the Procedure C, the transesterification of **M3** (300 mg, 92.3 μmol) with 6-azido-1-hexanol (513 μg, 3.69 mmol) was performed using Ti(O*i*Pr)$_4$ (81.1 μL, 277 μmol) in toluene (5.43 mL) to give **M3-I** as a white powder. Yield: 47.7%. $M_{n,NMR}$ = 3,310 g mol$^{-1}$, $M_{n,SEC}$ = 3,890 g mol$^{-1}$, $Đ$ = 1.07 (THF). $^1$H NMR (400 MHz, $CDCl_3$): $\delta$ 7.25−7.08 (br, 10H, −C(*Ph*)$_2$−), 4.02 (m, $\omega$-terminal, 2H, −C*H*$_2$(CH$_2$)$_5$N$_3$),

3.60 (−OC$H_3$, PMMA), 3.29 (t, $\omega$-terminal, 2H, −C$H_2$N$_3$), 2.47 (br, $\omega$-terminal, −C$H$(CH$_3$)COO−), 0.60−2.12 (br, main chain −C$H_2$C−, −CC$H_3$), 0.59−0.52 (m, 6H, $\alpha$-terminal −C$H_3$, −CH$_2$C$H_3$).

**Transesterification of S21M21 with 6-Azido-1-hexanol**

By following the Procedure C, the transesterification of **S21M21** (300 mg, 7.14 μmol) with 6-azido-1-hexanol (12.6 mg, 143 mmol) was performed using Ti(O*i*Pr)$_4$ (6.28 μL, 12.4 μmol) in toluene (2.00 mL) to give **S21M21-I** as a white powder. Yield: 86.3%. $M_{n,SEC}$ = 35,200 g mol$^{-1}$, $Đ$ = 1.03 (THF). $^1$H NMR (400 MHz, CDCl$_3$): $\delta$ 7.32−6.26 (br, aromatic), 4.02 (m, $\omega$-terminal, 2H, −C$H_2$(CH$_2$)$_5$N$_3$), 3.82−3.38 (br, −OC$H_3$, PMMA), 3.29 (t, $J$ = 6.6 Hz, $\omega$-terminal, 2H, −C$H_2$N$_3$), 2.47 (br, $\omega$-terminal, −C$H$(CH$_3$)COO−), 2.24−0.77 (br, main chain −C$H_2$C−, −CC$H_3$, −C$H_2$C$H$−, −C$H_2$C$H$−, PMMA, PS).

**Transesterification of M3 with Ethylene glycol**

By following the Procedure B, the transesterification of **M3** (300 mg, 92.3 μmol) with ethylene glycol (35.4 μL, 1.85 mmol) was performed using the titanium alkoxide, which had been prepared from Ti(O*i*Pr)$_4$ (81.1 μL, 277 μmol) and ethylene glycol (35.4 μL, 1.85 mmol) in toluene (5.43 mL), in toluene (5.43 mL) to give **M3-J**. The reaction progress was monitored by MALDI-TOF mass analysis.

**Transesterification of M3 with Triethylene Glycol Monomethyl Ether**

By following the Procedure B, the transesterification of **M3** (300 mg, 92.3 μmol) with triethylene glycol monomethyl ether (289 μL, 1.85 mmol) was performed using the titanium alkoxide, which had been prepared from Ti(O*i*Pr)$_4$ (81.1 μL, 277 μmol) and triethylene glycol monomethyl ether (289 μL, 1.85 mmol) in toluene (1.00 mL), in toluene (5.43 mL) to give **M3-K** as a white powder. Yield: 56.0%. $M_{n,NMR}$ = 3,150 g mol$^{-1}$, $M_{n,SEC}$ = 4,030 g mol$^{-1}$, $Đ$ = 1.06 (THF). $^1$H NMR (400 MHz, CDCl$_3$): $\delta$ 7.25−7.08 (br, 10H, −C(*Ph*)$_2$−), 4.20 (m, $\omega$-terminal, 2H, −C$H_2$CH$_2$(O(CH$_2$)$_2$)$_2$OCH$_3$), 3.60 (−OC$H_3$, PMMA), 3.34 (s, $\omega$-terminal, 3H, −(O(CH$_2$)$_2$)$_3$OC$H_3$), 2.50 (br, $\omega$-terminal, −C$H$(CH$_3$)COO−), 0.60−2.12 (br, main chain −C$H_2$C−, −CC$H_3$), 0.59−0.52 (m, 6H, $\alpha$-terminal −C$H_3$, −CH$_2$C$H_3$).

**Transesterification of S21M21 with Triethylene Glycol Monomethyl Ether**

By following the Procedure B, the transesterification of **S21M21** (500 mg, 11.9 μmol) with triethylene glycol monomethyl ether (37.2 μL, 238 mmol) was performed using the titanium alkoxide, which had been prepared from Ti(O*i*Pr)$_4$ (10.5 μL, 35.7 μmol) and triethylene glycol monomethyl ether (37.2 μL,

238 mmol) in toluene (1.00 mL), in toluene (3.00 mL) to give **S21M21-K** as a white powder. Yield: 78.2%. $M_{n,SEC}$ = 36,800 g mol$^{-1}$, $Đ$ = 1.03 (THF). $^1$H NMR (400 MHz, $CDCl_3$): $\delta$ 7.32−6.26 (br, aromatic), 4.20 (m, $\omega$-terminal, 2H, −C$H_2$CH$_2$(O(CH$_2$)$_2$)$_2$OCH$_3$), 3.82−3.38 (br, −OC$H_3$, PMMA), 3.39 (s, $\omega$-terminal, 3H, −(O(CH$_2$)$_2$)$_3$OC$H_3$), 2.50 (br, $\omega$-terminal, −C$H$(CH$_3$)COO−), 2.24−0.77 (br, main chain −C$H_2$C−, −CC$H_3$, −C$H_2$C$H$−, −C$H_2$C$H$−, PMMA, PS).

**Transesterification of M3 with Poly(ethylene Glycol) Monomethyl Ether**

By following the Procedure C, the transesterification of **M3** (150 mg, 46.2 μmol) with poly(ethylene glycol) monomethyl ether (5.04 g, 923 mmol) was performed using Ti(O*i*Pr)$_4$ (40.6 μL, 139 μmol) in toluene (2.71 mL) to give **M3-L**. The reaction progress was monitored by SEC and $^1$H NMR mass analysis.

**Transesterification of S21M21 with Poly(ethylene Glycol) Monomethyl Ether**

By following the Procedure C, the transesterification of **S21M21** (300 mg, 7.14 μmol) with poly(ethylene glycol) monomethyl ether (780 mg, 143 mmol) was performed using Ti(O*i*Pr)$_4$ (6.28 μL, 12.4 μmol) in toluene (2.00 mL). The obtained crude product was precipitated three times from THF solution into hot water to give **S21M21-L** as a white powder. Yield: 32.9%. $M_{n,SEC}$ = 42,000 g mol$^{-1}$, $Đ$ = 1.04 (THF). $^1$H NMR (400 MHz, $CDCl_3$): $\delta$ 7.32−6.26 (br, aromatic), 4.20 (m, $\omega$-terminal, 2H, −C$H_2$CH$_2$(O(CH$_2$)$_2$)$_n$OCH$_3$), 3.82−3.38 (br, −OC$H_3$, PMMA), 3.38 (s, $\omega$-terminal, 3H, −(O(CH$_2$)$_2$)$_n$OC$H_3$), 2.50 (br, $\omega$-terminal, −C$H$(CH$_3$)COO−), 2.24−0.77 (br, main chain −C$H_2$C−, −CC$H_3$, −C$H_2$C$H$−, −C$H_2$C$H$−, PMMA, PS).

### *3.2.5 Small-Angle X-ray Scattering Experiments*

Small-angle X-ray scattering (SAXS) experiments for the bulk samples were performed on BL-6A beamline of the Photon Factory at High Energy Accelerator Research Organization (KEK, Tsukuba, Japan). The X-ray wavelength and exposure time were 1.50 Å (8.27 keV) and 60 s, respectively. A PILATUS 1M (Dectris Ltd., Switzerland) detector, with 981 × 1043 pixels at a pixel size of 172 × 172 μm, and a counter depth of 20 bits (1,048,576 counts), was used for data acquisition. The sample-to-detector distance was calibrated using the scattering patterns of silver behenate (Nagara Science Co., Ltd., Japan). Bulk samples for SAXS experiments were placed in 1.5-mm-diameter soda glass capillaries (Hilgenderg, Germany) and

annealed under vacuum at 200 °C for 24 h. The SAXS data were acquired under ambient conditions, and 1D profiles were obtained as plots of scattering intensity as functions of scattering vector ($q$), where $q = (4\pi/\lambda)\sin(\theta/2)$ ($\lambda$, wave length; $\theta$, scattering angle).

## 3.3 Results and Discussion

### *3.3.1 Terminal-Selective Transesterification of PMMA using Titanium Alkoxides*

The titanium alkoxide-catalyzed transesterification of the PMMA homopolymer with 2-propanol was initially investigated to identify its terminal-selectivity and quantitativeness. An anionically-synthesized PMMA having a $M_{n,NMR}$ of 3,300 g mol$^{-1}$ (**M3**) was used as the starting material. The transesterification of **M3** was conducted in the presence of a catalytic amount of Ti(O*i*Pr)$_4$ and large excess of 2-propanol (A) in toluene at 100 °C for 24 h to yield the PMMA having an isopropyl methacrylate unit at the $\omega$-end (**M3-A**). The SEC trace of the product showed a monomodal elution peak with the narrow dispersity ($Đ$) of 1.06, suggesting the absence of any unexpected side reactions, such as degradation and intermolecular coupling (Figure 3.1a and entry 1 in Table 3.1). The $^1$H NMR spectrum of the product displayed a new signal at 4.94 ppm due to the methine proton of the isopropyl ester (proton *d* in Figure 3.2). Importantly, the minor signal due to the $\omega$-terminal proton of the main chain clearly shifted from 2.49 to 2.42 ppm upon the reaction, which strongly indicated that the methyl ester of the $\omega$-terminal MMA unit had been substituted with the isopropyl ester (proton $c^A$ in Figure 3.2). The extent of transesterification ($f_\omega$) was calculated to be 94% by comparing the peak areas of the proton *d* due to the isopropyl group and proton *a* due to the $\alpha$-terminal aromatic protons. In the MALDI-TOF MS spectrum of the product, only one series of peaks was observed with a regular interval of *m/z* 100 corresponding to the molar mass of the MMA unit (Figure 3.3). The mass change from **M3** to the product was 27.99, which is in good agreement with the theoretical difference in the molar mass between MMA and isopropyl methacrylate (28.03). These data confirmed that the obtained product has the expected structure of **M3-A**, demonstrating that Ti(O*i*Pr)$_4$ promoted the transesterification of the $\omega$-terminal MMA ester with 2-propanol in a quantitative manner.

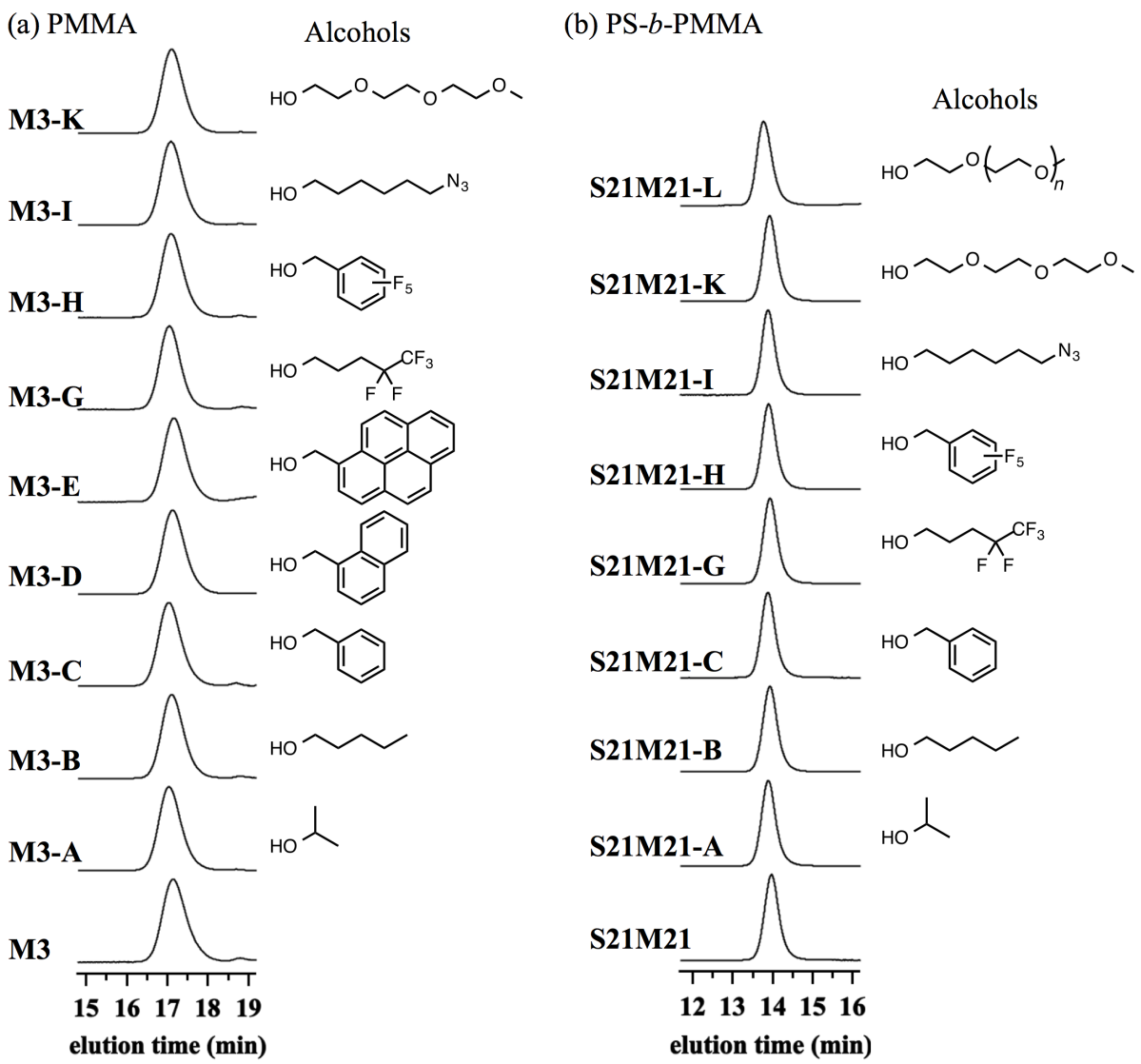


**Figure 3.1**. SEC traces of the modified (a) PMMAs and (b) PS-*b*-PMMAs and the corresponding parent polymers (eluent, THF; flow rate, 1.0 mL $min^{-1}$).

**Table 3.1**. Terminal-selective transesterification of PMMA using titanium alkoxides[a]

| entry | alcohol[b] | reaction time (h) | $M_{n,NMR}$[c] (g mol$^{-1}$) | $f_\omega$[d] (%) | $M_{n,SEC}$[e] (g mol$^{-1}$) | $Đ$[e] | yield (%) | sample name |
|---|---|---|---|---|---|---|---|---|
| - | (parent PMMA) | - | 3,300 | - | 3,760 | 1.08 | - | **M3** |
| 1 | 2-propanol (A) | 24 | 3,290 | 94 | 4,080 | 1.06 | 47.7 | **M3-A** |
| 2 | 1-pentanol (B) | 24 | 3,260 | >99 | 4,040 | 1.06 | 51.3 | **M3-B** |
| 3 | benzyl alcohol (C) | 24 | 3,340 | 96 | 4,090 | 1.06 | 48.3 | **M3-C** |
| 4 | 1-naphthalene-methanol (D) | 30 | 3,060 | 71 | 3,890 | 1.07 | 40.0 | **M3-D** |
| 5 | 1-pyrene-methanol (E) | 168 | 3,410 | 10 | 3,770 | 1.07 | 67.0 | **M3-E** |
| 6 | HFIP (F) | 24 | n.d. | 0 | n.d. | n.d. | n.d. | **M3-F** |
| 7 | 4,4,5,5,5-pentafluoro-pentanol (G) | 24 | 3,430 | >99 | 4,280 | 1.05 | 19.7 | **M3-G** |
| 8 | pentafluorobenzyl alcohol (H) | 24 | 3,370 | 76 | 4,040 | 1.06 | 47.7 | **M3-H** |
| 9 | 6-azido-1-hexanol (I) | 24 | 3,310 | >99 | 3,890 | 1.07 | 40.0 | **M3-I** |
| 10 | ethylene glycol (J) | 24 | n.d. | 0 | n.d. | n.d. | n.d. | **M3-J** |
| 11 | TEG (K) | 24 | 3,150 | 98 | 4,030 | 1.06 | 56.0 | **M3-K** |
| 12 | PEG (L) | 30 | n.d. | 88 | n.d. | n.d. | n.d. | **M3-L** |

[a]Argon atmosphere; solvent, toluene; temperature, 100 °C; $[Ti(OR)_4]_0/[PMMA]_0$ = 3/1. [b]Alcohols: HFIP, 1,1,1,3,3,3-hexafluoro-2-propanol; PFP, 4,4,5,5,5-pentafluoropentanol; TEG, triethylene glycol monomethyl ether; PEG, poly(ethylene glycol) monomethyl ether. [c]Determined by $^1$H NMR in $CDCl_3$. [d]Chain-end functionality is determined by $^1$H NMR on the presumption that only one MMA unit was transesterified. [e]Determined by SEC in THF using PMMA standards.

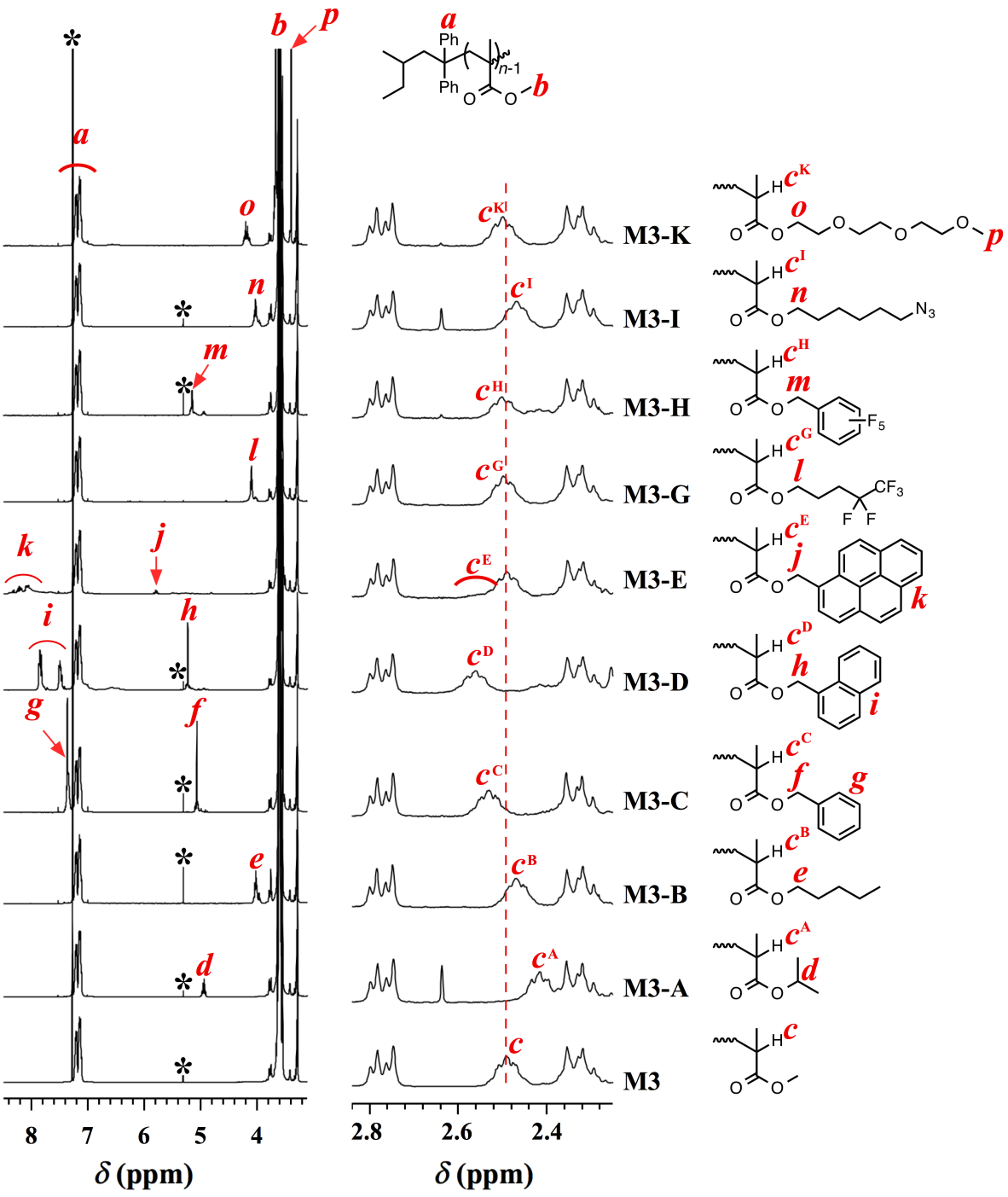


**Figure 3.2**. $^{1}$H NMR spectra of the modified PMMAs and the corresponding parent polymer in $CDCl_3$ (400 MHz).

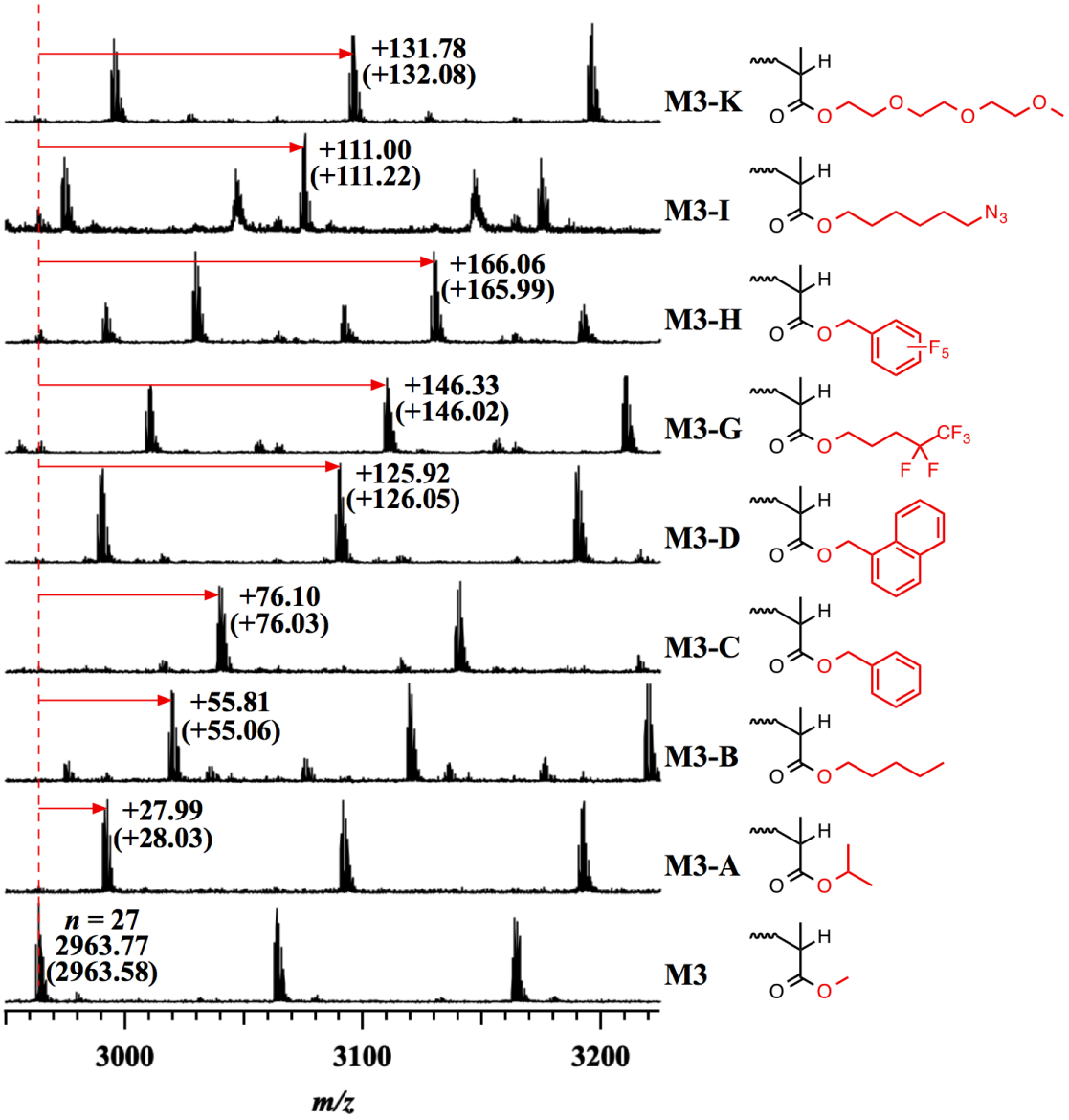


**Figure 3.3**. MALDI-TOF mass spectra of the modified PMMAs and the corresponding parent polymer. The found and theoretical *m/z* values of 27-mer are shown without and with brackets, respectively.

To extend the applicable range, the terminal-selective transesterifications of **M3** were further performed using various alcohols, such as 1-pentanol (B), benzyl alcohol (C), 1-naphthalenemethanol (D), 1-pyrenemethanol (E), 1,1,1,3,3,3-hexafluoro-2-propanol (HFIP, F), 4,4,5,5,5-pentafluoropentanol (G), pentafluorobenzyl alcohol (H), 6-azido-1-hexanol (I), ethylene glycol (J), triethylene glycol monomethyl ether (TEG, K), and poly(ethylene glycol) monomethyl ether (PEG, L). Prior to the transesterification reactions, Ti(O*i*Pr)$_4$ was treated with the alcohols to form the corresponding titanium alkoxides (Ti(OR)$_4$), which were then directly subjected to the transesterification reaction. The SEC traces of all the products displayed a monomodal elution peak with a narrow *Đ*, suggesting the absence of any unexpected side reactions (Figure 3.1a). The $^1$H NMR spectra of **M3-B** with a pentyl ester, **M3-C** with a benzyl ester, and **M3-D** with a naphthalenemethyl ester showed the appearances of new signals due to the methylene protons adjacent to the newly formed ester unit (proton *e*, *f*, and *h* in Figure 3.2, respectively). In addition, the *ω*-terminal proton signals clearly shifted after the reaction, indicating the high terminal-selectivity (protons $c^B$, $c^C$, and $c^D$ in Figure 3.2, respectively). Although the MALDI-TOF MS spectra of **M3-B**, **M3-C**, and **M3-D** revealed the presence of a small amount of byproducts whose two MMA units were transesterified, the major products were found to be the target products (Figure 3.3). In the $^1$H NMR spectrum of **M3-E**, whereas new signals due to methylene and aromatic protons of the incorporated pyrenemethyl group were observed, the small peak areas indicated a low $f_\omega$ value (Figure 3.2). Unfortunately, the author failed to quantify the extent of the reaction in **M3-E** by the MALDI-TOF MS analysis because the molar mass of the reaction product is overlapped with that of the starting material. The low reactivity of the 1-pyrenemethanol is attributed to the low solubility of the corresponding titanium alkoxide in toluene. The transesterification reactions using 4,4,5,5,5-pentafluoropentanol and pentafluorobenzyl alcohol efficiently provided the corresponding products, *i.e.*, **M3-G** and **M3-H**, respectively, as characterized by $^1$H NMR and MALDI-TOF MS. On the other hand, the reaction product of **M3** and HFIP (**M3-F**) revealed that no reaction occurred. The high acidity of HFIP is responsible for this result.

The incorporation of reactive functional groups into the polymer chain end is significantly important from the polymer synthesis point of view because it allows polymers to undergo a further chain-end modification. To incorporate the reactive functional group into the PMMA-chain end, 6-azido-1-hexanol

was used for the terminal-selective transesterification. In FT-IR spectrum of the product, an absorption peak was newly observed at 2098 $cm^{-1}$, which indicated the incorporation of the azido group into the PMMA (Figure 3.4). The $^1H$ NMR spectrum of the product (**M3-I**) showed a new signal assignable to the methylene protons adjacent to the ester group of the 6-azidohexyl methacrylate, suggesting the progress of the transesterification (proton *n* in Figure 3.2). The MALDI-TOF MS spectrum of the product showed two series of peaks regularly separated by *m/z* 100 corresponding to the molar mass of an MMA unit (Figure 3.3). A series of peaks with higher intensities was assigned to the structure of the target **M3-I** with a 6-azidohexyl ester. Another series of peaks with lower intensities was assigned to the fragmentation product of **M3-I** formed during the MALDI-TOF MS measurement by the decomposition of the azido group.[13] These results confirmed the successful synthesis of **M3-I** possessing an azido group. The azido group at the chain end enables further chain-end modifications with ethynyl-functionalized low-molecular-weight compounds and polymers via the click chemistry.

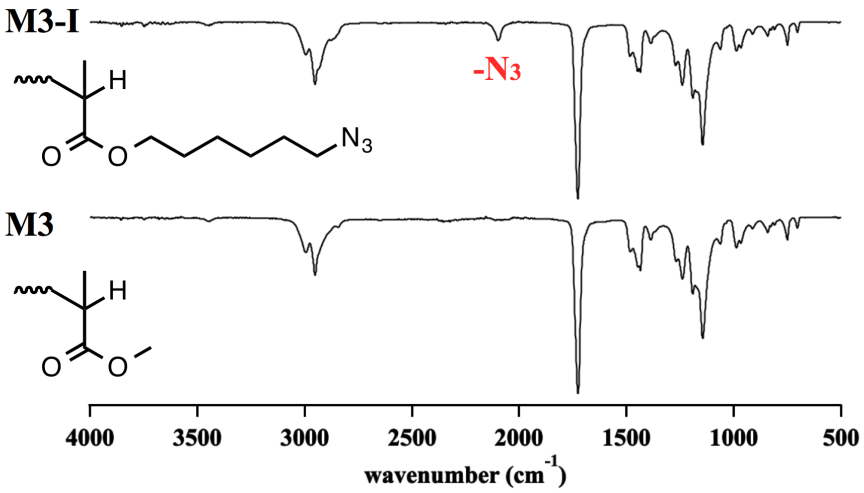


**Figure 3.4**. FT-IR spectra of the **M3-I** and **M3**.

The incorporation of a hydroxyl group at the polymer chain end is also highly beneficial. Although the author tried the transesterification of **M3** with ethylene glycol aiming at providing **M3-J**, no reaction

occurred because the titanium catalyst was deactivated by its polycondensation with ethylene glycol. To avoid such an issue, the terminal-selective transesterification should be performed with diols having a longer spacer.[12]

The terminal-selective transesterification of **M3** with triethylene glycol monomethyl ether (TEG) effectively yielded the target product, i.e., **M3-K**, as evidenced by the $^{1}$H NMR and MALDI-TOF MS analyses (Figures 3.2 and 3.3). To further extend the utility of the terminal-selective transesterification, a hydroxy-functionalized polymer was then employed as an alcohol. The SEC trace of the crude reaction product of **M3** with a PEG having the $M_{n,NMR}$ of 5,450 g mol$^{-1}$ clearly showed a new elution peak in the higher molecular weight region as compared to the starting materials, suggesting the formation of a BCP consisting of PMMA and PEG (PMMA-*b*-PEG, *i.e.*, **M3-L**) (Figure 3.5). Although the removal of the excess PEG from the BCP failed, this result suggested that the terminal-selective transesterification system works even with hydroxy-functionalized polymers, thus leading to a novel synthetic method for the PMMA-based BCPs.

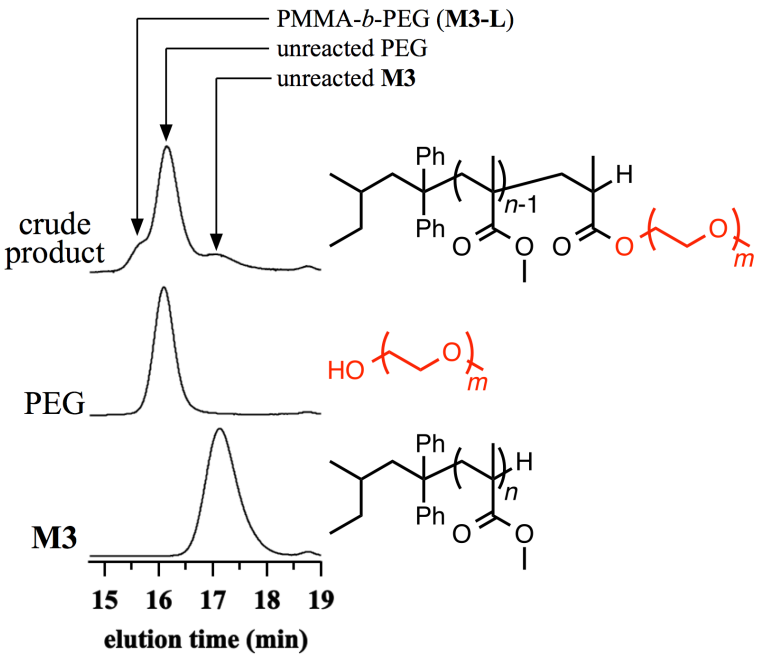


**Figure 3.5**. SEC traces of the crude product of **M3-L** (upper), PEG (middle), and **M3** (lower) (eluent, THF; flow rate, 1.0 mL min$^{-1}$).

### *3.3.2 Terminal-Selective Transesterification of PS-b-PMMA using Titanium Alkoxides*

The terminal-selective transesterification of PS-*b*-PMMA was then investigated to synthesize a series of end-functionalized PS-*b*-PMMAs. The transesterification reactions were performed under the same conditions as for PMMA. The PS-*b*-PMMA having the $M_n$ of 42,000 g mol$^{-1}$ (**S21M21**) was used as the starting material and 2-propanol (A), 1-pentanol (B), benzyl alcohol (C), 4,4,5,5,5-pentafluoropentanol (G), pentafluorobenzyl alcohol (H), 6-azido-1-hexanol (I), TEG (K), and PEG (L) were used as the alcohols to yield **S21M21-A**, **S21M21-B**, **S21M21-C**, **S21M21-G**, **S21M21-H**, **S21M21-I**, **S21M21-K**, and **S21M21-L**, respectively. In the SEC traces of all the products, the monomodal elution peak with a narrow $Đ$ was maintained even after the reaction (Figure 3.1b). Importantly, the SEC traces of **S21M21-L** shifted to the higher molecular weight region as compared to that of the original **S21M21**, suggesting the formation of the triblock terpolymer, *i.e.*, PS-*b*-PMMA-*b*-PEG. The $^1$H NMR spectra of the products showed that the signals due to the $\omega$-terminal protons of the main chains were shifted after the reaction, supporting the terminal-selectivity (Figure 3.6). In addition, the signals due to the newly-formed ester moieties were also observed. The $f_\omega$s value for the products was determined to be 62−99% based on the end group analysis of the $^1$H NMR spectra (Table 3.2). Thus, the transesterification using titanium alkoxides can be applied to the PS-*b*-PMMA systems with the various alcohols. Importantly, the transesterifications with 6-azido-1-hexanol endowed PS-*b*-PMMA with a clickable end group. The transesterifications with PEG also effectively incorporated the PEG segment into the PMMA-chain end of the PS-*b*-PMMA to yield the triblock terpolymer, which can be a novel synthetic methodology for the BCPs. The fact that the PS-*b*-PMMA-*b*-PEG triblock terpolymer is reported to form a highly-ordered PS nanopattern further supports the utility of this synthetic approach.[14,15] The present facile and efficient chain-end modification technique allows one to systematically investigate the relationship between the chain-end structures and polymer properties including the microphase-separation behavior.

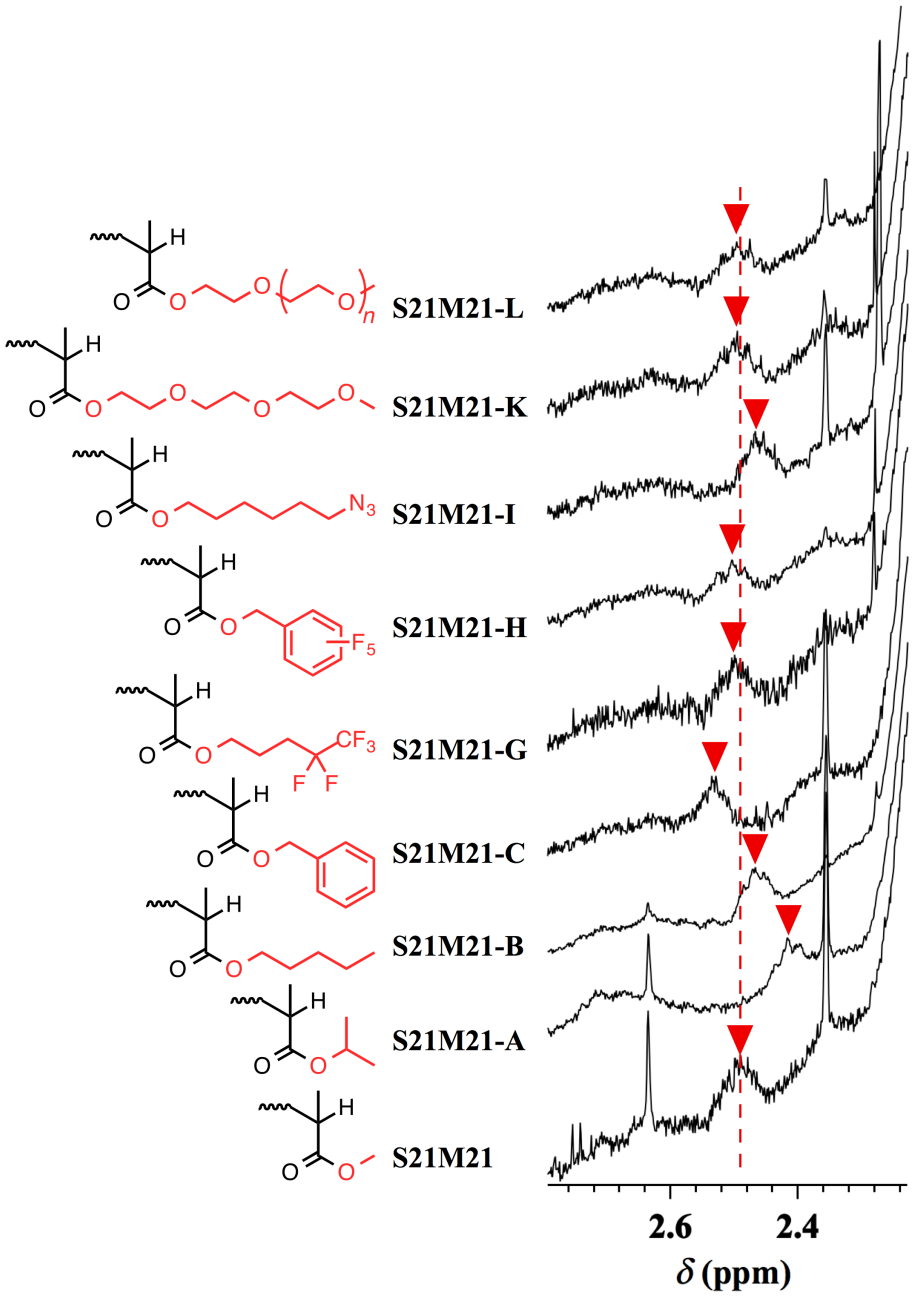


**Figure 3.6**. Partial $^{1}$H NMR spectra of the modified PS-*b*-PMMAs and the corresponding parent polymer in $CDCl_3$ (400 MHz).

**Table 3.2**. Molecular characteristics of the modified PS-*b*-PMMAs[a]

| polymer | alcohol[b] | $f_\omega$[c] (%) | $M_{n,SEC}$[d] (g mol$^{-1}$) | $Đ$[d] | $d$[e] (nm) |
|---|---|---|---|---|---|
| **S21M21** | (parent PS-*b*-PMMA) | - | 35,500 | 1.03 | 23.7 |
| **S21M21-A** | 2-propanol (A) | 77 | 35,200 | 1.03 | 23.2 |
| **S21M21-B** | 1-pentanol (B) | 96 | 36,700 | 1.03 | 23.2 |
| **S21M21-C** | benzyl alcohol (C) | 99 | 35,400 | 1.03 | 23.7 |
| **S21M21-G** | 4,4,5,5,5-pentafluoro-pentanol (G) | >99 | 36,000 | 1.03 | 24.1 |
| **S21M21-H** | pentafluorobenzyl alcohol (H) | 62 | 37,500 | 1.03 | 23.7 |
| **S21M21-I** | 6-azido-1-hexanol (I) | >99 | 35,200 | 1.03 | 25.1 |
| **S21M21-K** | TEG (K) | 94 | 36,800 | 1.03 | 23.6 |
| **S21M21-L** | PEG (L) | 85 | 42,000 | 1.04 | 26.2 |

[a]Argon atmosphere; solvent, toluene; temperature, 100 °C; $[Ti(OR)_4]_0/[PMMA]_0$ = 3/1. [b]Alcohols: TEG, triethylene glycol monomethyl ether; PEG, poly(ethylene glycol) monomethyl ether. [c]Determined by $^1$H NMR in $CDCl_3$. [d]Determined by SEC in THF using PMMA standards. [e]Calculated from primary peak position ($q^*$) in SAXS profile using equation $d = 2\pi/q^*$.

### *3.3.3 Microphase Separation of End-Functionalized PS-b-PMMAs*

A series of the chain-end functionalized PS-*b*-PMMAs as well as the corresponding starting materials were subjected to the small angle X-ray scattering (SAXS) experiments to investigate the effect of the chain-end structures on the microphase-separation behavior in the bulk. After the thermal annealing at 200 °C for 24 h and rapid quenching, the SAXS profiles were acquired at room temperature. The SAXS profile of **S21M21** showed the characteristic scattering pattern corresponding to the microphase separation (Figure 3.7). In addition to the principle scattering peak ($q^*$) observed at 0.265 $nm^{-1}$, higher-order scattering peaks appeared at the $q/q^* = 2$ and 3 positions, which indicated the lamellar structure with the domain spacing ($d$) of 23.7 nm (Table 3.2). The SAXS profiles of **S21M21-A**, **S21M21-B**, **S21M21-C**, **S21M21-G**, **S21M21-H**, and **S21M21-K** showed scattering patterns similar to **S21M21** without significant changes in the morphology and $d$ value. Although **S21M21-I** with an azido group also displayed the SAXS pattern associated with the lamellar structure, the principle scattering peak was observed in the lower $q$ region than that of **S21M21**, indicating that the $d$ value increased to 25.1 nm after incorporation of the azido group. This result suggested the remarkable effect of the chain-end structures on the microphase-separation behavior even though the weight fractions of the incorporated chain end are less than 1.0 wt%. Since the degrees of polymerization have not been changed after the transesterification, the increase in the $d$ value is due to the enhancement of the incompatibility between the blocks. It is believed that the polar character of the azido group contributed to increasing the incompatibility between the blocks. The SAXS profile of **S21M21-L** with a PEG segment indicated the clear increase in the $d$ value from 23.7 to 26.2 nm upon incorporation of a PEG segment into the PMMA-chain end. The increase in the $d$ value should be attributed to the following two factors: one is the increase in the total degree of polymerization (polymer volume) and the other is the enhancement of the effective $\chi$ because of the strong segregation strength between PS and PEO.[14,15]

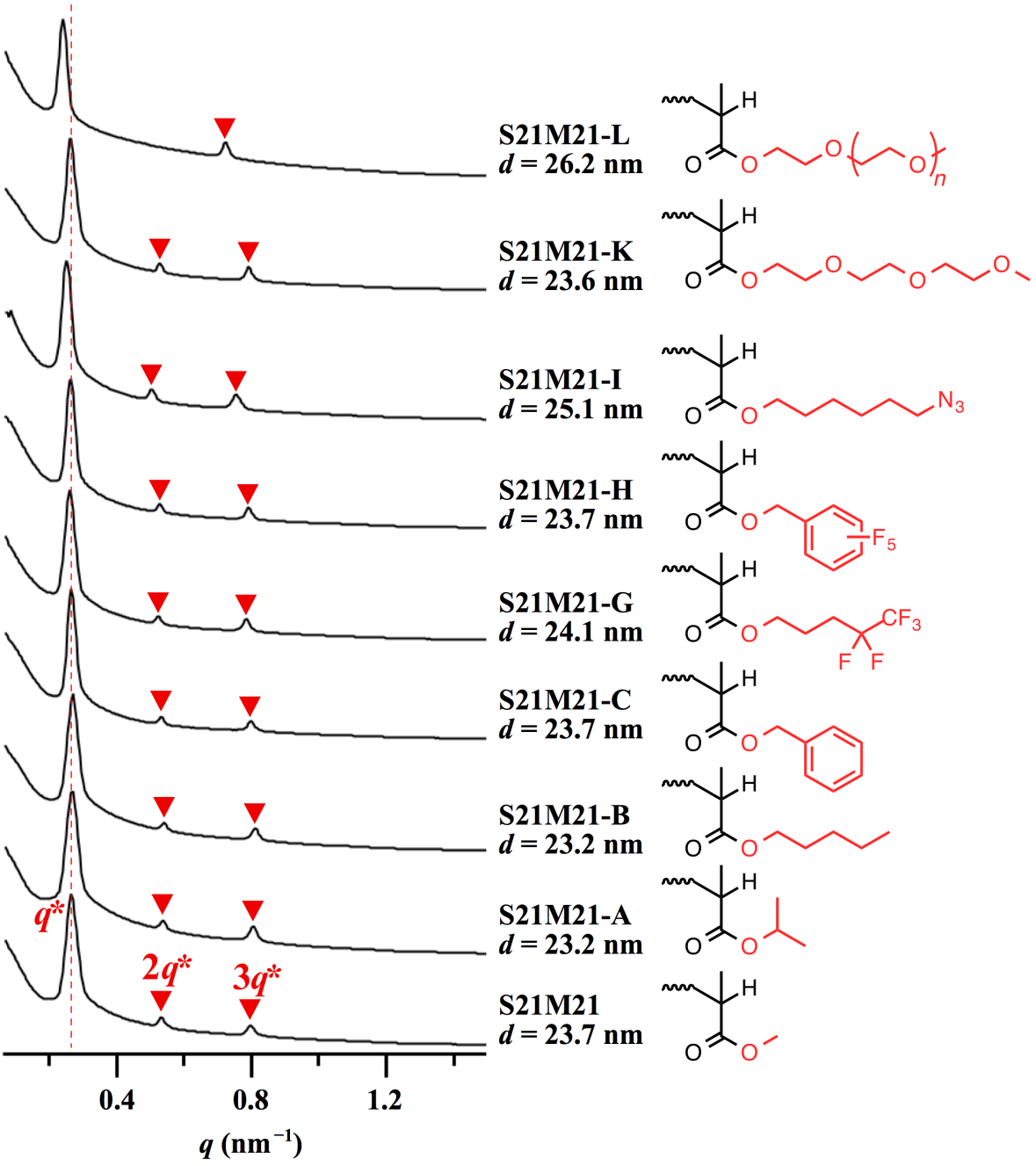


**Figure 3.7**. SAXS profiles of the modified PS-*b*-PMMAs and the corresponding parent polymer after thermal annealing at 200 °C for 24 h.

## 3.4 Conclusion

The author demonstrated the facile and efficient chain-end modification of PMMA and PS-*b*-PMMA by the terminal-selective transesterification with various alcohols in the presence of the corresponding titanium alkoxides. The reaction can be conducted by using various alcohols having alkyl, aromatic ring, fluoroalkyl, and azido groups, and even a polymer chain. The terminal-selective transesterification approach offers easy access to the end-functionalized PMMA and PS-*b*-PMMA as well as the PMMA-based diblock copolymers and PS-*b*-PMMA-based triblock terpolymers, which is of significant importance in view of the polymer synthesis. A screening of the chain-end structure by the postpolymerization modification without any change in the degree of polymerization and dispersity enables the systematic investigation of the chain-end effect on the microphase-separation behavior. The PS-*b*-PMMAs having an azido group and polyethylene glycol segment at the $\omega$-chain end presented in this chapter showed the clear increase in the domain spacing of the microphase-separated structures, suggesting the remarkable chain-end effects.

## 3.5 References

1. Choi, S.; Han, C. D. Phase Transition in End-Functionalized Polystyrene-*block*-polyisoprene-*block*-polystyrene Copolymers. *Macromolecules* **2003**, *36,* 6220–6228.

2. Jeong, U.; Ryu, D. Y.; Kim, J. K. Phase Behavior of Polystyrene-*block*-poly(*n*-butyl methacrylate) Copolymers with Various End-Functional Groups. *Macromolecules* **2003**, *36,* 8913–8918.

3. Kim, J. K.; Kim, M. I.; Kim, H. J.; Lee, D. H.; Jeong, U.; Jinnai, H.; Suda, K. Unusual Phase Behavior of End-Functionalized Polystyrene-*block*-poly(*n*-butyl methacrylate) Copolymer with Maleic Anhydride. *Macromolecules* **2007,** *40,* 7590–7593.

4. Lee, K. S.; Lee, J.; Kwak, J.; Moon, H. C.; Kim, J. K. Reduction of Line Edge Roughness of Polystyrene-*block*-Poly(methyl methacrylate) Copolymer Nanopatterns By Introducing Hydrogen Bonding at the Junction Point of Two Block Chains. *ACS Appl. Mater. Interfaces* **2017**, *9*, 31245−31251.

5. Woo, S.; Jo, S.; Ryu, D. Y.; Choi, S.; Choe, Y.; Huh, J.; Bang, J. Molecular Tailoring of Poly(styrene-*b*-methyl methacrylate) Block Copolymer Toward Perpendicularly Oriented Nanodomains with Sub-10 nm Features. *ACS Macro Lett.* **2017**, *6*, 1386−1391.

6. Jo, G.; Ahn, H.; Park, M. J. Simple Route for Tuning the Morphology and Conductivity of Polymer Electrolytes: One End Functional Group is Enough. *ACS Macro Lett.* **2013**, *2*, 990−995.

7. Jung, H. Y.; Mandal, P.; Jo, G.; Kim, O.; Kim, M.; Kwak, K.; Park, M. J. Modulating Ion Transport and Self-Assembly of Polymer Electrolytes via End-Group Chemistry. *Macromolecules* **2017**, *50*, 3224–3233.

8. Ho, C.; Dai, C.; Su, W. High Yield Synthesis of Diverse Well-Defined End-Functionalized Polymers by Combination of Anionic Polymerization and ‘‘Click’’ Chemistry. *J. Appl. Polym. Sci.* **2009**, *111*, 1571–1580.

9. Ho, C.; Lee, Y.; Dai, C.; Segalman, R. A.; Su, W. Synthesis and Self-Assembly of Poly-(diethylhexyloxy-*p*-phenylenevinylene)-*b*-poly(methyl methacrylate) Rod-Coil Block Copolymers. *Macromolecules* **2009**, *42*, 4208–4219.

10. Moon, H. C.; Anthonysamy, A.; Kim, J. K. Facile Synthetic Route for Well-Defined Poly(3-hexylthiophene)-*block*-poly(methyl methacrylate) Copolymer by Anionic Coupling Reaction. *Macromolecules* **2011**, *44*, 1894–1899.

11. Kohsaka, Y.; Kitayama, T. Precise anionic polymerization of methyl methacrylate: simultaneous control of molecular weight, stereoregularity and end-structure. *Nippon Gomu Kyokaishi* **2015**, *88*, 80–85.

12. Ogura, Y.; Terashima, T.; Sawamoto, M. Terminal-Selective Transesterification of Chlorine-Capped Poly(Methyl Methacrylate)s: A Modular Approach to Telechelic and Pinpoint-Functionalized Polymers. *J. Am. Chem. Soc.* **2016**, *138*, 5012−5015.

13. Isono, T.; Kamoshida, K.; Satoh, Y.; Takaoka, T.; Sato, S.; Satoh, T.; Kakuchi, T. Synthesis of Star- and Figure-Eight-Shaped Polyethers by *t*-Bu-$P_4$-Catalyzed Ring-Opening Polymerization of Butylene Oxide. *Macromolecules* **2013**, *46*, 3841−3849.

14. Bang, J.; Kim, S. H.; Drockenmuller, E.; Misner, M. J.; Russell, T. P.; Hawker, C. J. Defect-Free Nanoporous Thin Films from ABC Triblock Copolymers. *J. Am. Chem. Soc.* **2006**, *128*, 7622-7629.

15. Bang, J.; Kim, B. J.; Stein, G. E.; Russell, T. P.; Li, X.; Wang, J.; Kramer, E. J.; Hawker, C. J. Effect of Humidity on the Ordering of PEO-Based Copolymer Thin Films. *Macromolecules* **2007**, *40,* 7019-7025.

# *Chapter 4*

## Chain-End Functionalization with a Saccharide for 10 nm Microphase Separation: "Classical" PS-*b*-PMMA versus PS-*b*-PMMA-Saccharide

## 4.1 Introduction

The chain-end structure of the block copolymer (BCP) has a significant impact on the self-assembly behavior, as described in Chapter 3. However, induction of microphase separation from a classical BCP, which is completely disordered, by a simple chain-end modification has never been achieved. In this context, the author postulated that the introduction of a highly-hydrophilic component at the BCP chain end would be an efficient way of inducing microphase separation of classical BCPs having a low incompatibility between the blocks, thus leading to extremely small features.

Saccharides are useful building blocks for designing BCPs capable of microphase separation into extremely small features because the dense array of hydroxyl groups provides a strong hydrophilicity, leading to the strong segregation strength with the hydrophobic polymers. In fact, several polymer systems containing oligosaccharides have been reported as suitable BCP materials for fabricating the small microphase separation with a domain spacing ($d$) of <20 nm.[1–3] Borsali, Kakuchi, and Satoh's groups reported the preparation of oligosaccharide-containing polystyrenes, polycaprolactones, and poly($\delta$-decanolactone)s and showed that these BCP systems indeed formed microphase-separated structures with 10-nm-scale $d$ values.[4–9] Considering such a strong segregation between the saccharides and hydrophobic polymers, the saccharides at the chain end of the hydrophilic block in the low-$\chi$ BCP should promote the microphase separation with small size features. Therefore, in this study, the author aimed to install mono/oligosaccharide moieties at the chain ends of polystyrene-*block*-poly(methyl methacrylate) (PS-*b*-PMMA) to fabricate the 10-nm-scale microphase-separated structure. The strong hydrophilicity of the mono/oligosaccharide at the PMMA chain end increases the effective hydrophilicity of the overall PMMA block, which in turn, permits the saccharide-incorporated PS-*b*-PMMA to microphase-separate even at a low $N$ due to the enhanced incompatibility between the PS and mono/oligosaccharide-incorporated PMMA blocks.

The author now reports the efficient synthesis of a series of PS-*b*-PMMA having a mono/oligosaccharide at the PMMA chain end (PS-*b*-PMMA-mono/oligosaccharides). The synthesis involves two steps starting from the anionically-prepared PS-*b*-PMMAs, namely, the terminal-selective transesterification and click reaction (Scheme 4.1). The PS-*b*-PMMA-oligosaccharides were found to microphase-separate with a $d$ of *ca.* 10 nm in both the bulk and thin-film states, even though their unmodified

classical PS-*b*-PMMAs exist in miscible states due to their low-$\chi$ and low-$N$ values. The results of this study revealed that the installation of an oligosaccharide segment at the PMMA chain end of a PS-*b*-PMMA induces microphase separation. Hence, the author successfully produced extremely small patternings from PS-*b*-PMMA, which intrinsically exist in completely disordered states, by installing an oligosaccharide as a hydrophilic component.

**Scheme 4.1.** Synthesis of PS-*b*-PMMAs bearing mono/oligosaccharides at their PMMA chain ends by terminal-selective transesterification and click chemistry

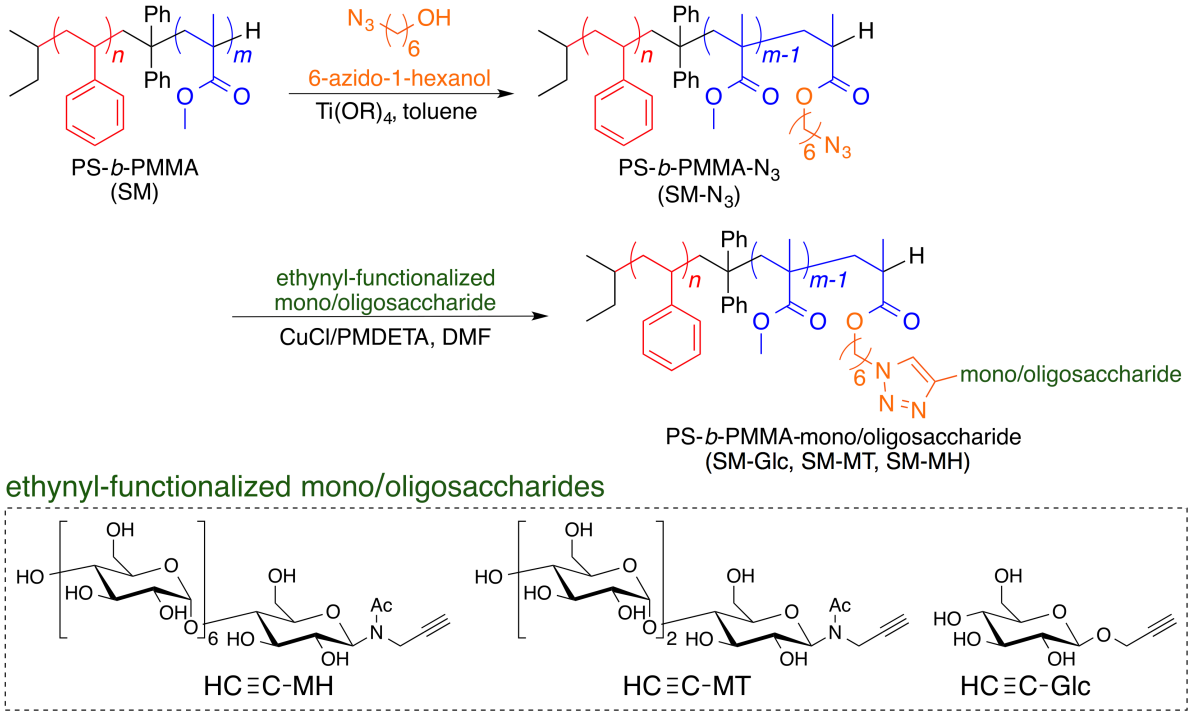

## 4.2 Experimental Section

### *4.2.1 Material*

Titanium isopropoxide (Ti(O*i*Pr)$_4$), *N*,*N*,*N*',*N*'',*N*''-pentamethyldiethylenetriamine (PMDETA; >99.0%), propargyl amine (>97.0%), and (1-bromoethyl)benzene (1-PEBr; >95.0%) were purchased from Tokyo Chemical Industry Co., Ltd., and used as received. Methyl methacrylate (stabilized with 6-*tert*-Butyl-2,4-xylenol; >99.8%) and styrene (stabilized with 4-*tert*-butylcatechol; >99.0%) were purchased from Tokyo Chemical Industry Co., Ltd., and purified by distillation over calcium hydride. *sec*-Butyllithium (*sec*-BuLi; in cyclohexane and *n*-hexane, 1.0 mol L$^{-1}$) and sodium azide ($NaN_3$; >97.0%) were purchased from Kanto Chemical Co., Inc., and used as received. 1,1-Diphenylethylene (DPE; stabilized with hydroquinone; >98.0 %) were purchased from Tokyo Chemical Industry Co., Ltd., and purified by distillation over *sec*-BuLi. Copper(I) chloride (CuCl; 99.995% trace metals basis) and copper(I) bromide (CuBr; 99.999% trace metals basis) were purchased from Sigma-Aldrich Chemicals Co., and used as received. Lithium chloride (LiCl; >99.0%) was purchased from Kanto Chemical Co., Inc., and used after drying under reduced pressure at 180 °C for 24 h. Maltotriose (MT; >97.0%) was purchased from Hayashibara Co., Ltd., and used as received. 6-Azido-1-hexanol[10], *N*-maltoheptaosyl-3-acetamido-1-propyne (**HC≡C-MH**)[11], and 1-propargyl-*β*-D-glucopyranoside (**HC≡C-Glc**)[12] were synthesized according to the literature. The PS-*b*-PMMAs (**S6M3**, 9.20 kg mol$^{-1}$, $f_{St}$ = 0.68; **S4M4**, 8.50 kg mol$^{-1}$, $f_{St}$ = 0.52; **S3M6**, 9.20 kg mol$^{-1}$, $f_{St}$ = 0.35) were provided in the forms of propylene glycol methyl ether acetate solutions by Tokyo Ohka Kogyo Co., Ltd., and precipitated in methanol and dried prior to use. The cellophane tube (Spectra/por® 6 Membrane; MWCO: 1,000) was purchased from Spectrum Laboratories and washed with water and methanol before use. The metal scavenger (QuadraSil™ AP) was purchased from FUJIFILM Wako Pure Chemical Corp., and used as received.

### *4.2.2 Characterization*

The SEC experiments were performed at 40 °C using a Shodex GPC-101 gel-permeation chromatography system (Shodex DU-2130 dual pump, Shodex RI-71 reflective index detector, and Shodex ERC-3125SN degasser) equipped with a Shodex KF-G guard column (4.6 mm × 10 mm; particle size, 8 μm) and two Shodex KF-804L columns (linear, 8 mm × 300 mm linear; particle size, 5 μm; exclusion limit, 4 ×

$10^6$) in THF at a flow rate of 1.0 mL $min^{-1}$, or an Agilent 1260 Infinity GPC/SEC system (Agilent quaternary pump, 1260-MDS refractive index detector) equipped with a Shodex Asahipak GF-310 HQ column (linear, 7.6 mm × 300 mm; pore size, 20 nm; bead size, 5 μm; exclusion limit, $4 \times 10^4$ g $mol^{-1}$) and a Shodex Asahipak GF-7 M HQ column (linear, 7.6 mm × 300 mm; pore size, 20 nm; bead size, 9 μm; exclusion limit, $4 \times 10^7$ g $mol^{-1}$) in DMF containing lithium chloride (0.01 mol $L^{-1}$) at a flow rate of 0.60 mL $min^{-1}$. The number-average molecular weight ($M_{n,SEC}$) and dispersity ($Đ$) values were calculated using PS standards for PS-*b*-PMMA- and PS-based polymers and PMMA standards for the PMMA-based polymers. $^1$H NMR (400 MHz) spectra were recorded using a JEOL JNM-ECS400 instrument, and FT-IR spectra were acquired using a PerkinElmer Frontier MIR spectrometer equipped with a single-reflection diamond universal attenuated total reflection attachment. Matrix-assisted laser desorption ionization time-of-flight mass spectrometry (MALDI-TOF MS) of the polymers was performed using an Applied Biosystems ABSCIEX MALDI TOF/TOF 5800 instrument in linear mode (for PMMA samples) and reflector mode (for PS samples). The MALDI-TOF MS samples were prepared by depositing a mixture of the polymer, matrix, and cationic agent in THF onto a sample plate. A 5:5:1 (v/v) ratio of [PMMA (1.0 g $L^{-1}$ in THF)]/[dithranol (40 g $L^{-1}$ in THF)]/[sodium trifluoroacetate (5.0 g $L^{-1}$ in THF)] was used, while a 1:5:1 (v/v) ratio of [PS (5.0 g $L^{-1}$ in THF)]/[dithranol (10 g $L^{-1}$ in THF)]/[silver trifluoroacetate (2.0 g $L^{-1}$ in THF)] was used.

### *4.2.3 Synthesis of N-Maltotriosyl-3-acetamido-1-propyne*

MT (5.0 g, 9.91 mmol) and propargyl amine (12.9 g, 234 mmol) were added to a round-bottom flask, and the mixture was stirred under a nitrogen atmosphere for 72 h. The excess of propargyl amine was removed by co-evaporation with a mixed solvent of toluene and methanol (9/1 (v/v)). The obtained residue was dissolved in a mixture of methanol (200 mL) and acetic anhydride (40 mL). After stirring at room temperature for 48 h, the solvent and excess of acetic anhydride was removed by co-evaporation with a mixed solvent of toluene and methanol (1/1 (v/v)). The obtained residue was freeze dried from its aqueous solution to give **HC≡C-MT** as a white solid (5.08 g). Yield: 90.2%. $[\alpha]_D$ = + 126.0 (*c* 1.0, $H_2O$). $^1$H NMR (400 MHz, $D_2O$): $\delta$ 5.54 and 5.09 (rotamers, 1H, H-1), 5.39-5.44 (m, 2H, H-1), 3.24-4.32 (m, 20H, H-2,-3,-4,-5,-6,-NC*H*2-), 2.74 and 2.58 (t, 1H, rotamers, *J* = 2.3 Hz, *J* = 2.3 Hz, -CC*H*), 2.32 and 2.25 (s, 3H, -C$H_3$). $^{13}$C

NMR (100 MHz, $D_2O$): $\delta$ (ppm) 177.2 (-*C*$OCH_3$), 102.4 and 102.1 (C-1), 89.0 (C-1), 79.7, 79.4, 79.3, 79.1, 78.5, 75.9, 75.5, 75.3, 74.3, 74.1, 73.8, 72.8, and 71.9 (C-2,-3,-4,-5,-6,-*C*CH,-C*C*H), 63.2 and 63.0 (C-6), 41.7 (-N*C*$H_2$-), 23.8 (-*C*$H_3$HH). HRMS (ESI-TOF) (*m/z*) Calcd. for $[M+Na]^+$: 606.2004. Found: 606.2003.

### *4.2.4 Synthesis of PS-b-PMMA bearing A Mono/oligosaccharide at the ω-Chain End.*

**Terminal-Selective Transesterification of PS-*b*-PMMA using 6-Azido-1-hexanol**

The following is a typical terminal-selective transesterification procedure. Titanium isopropoxide (Ti(O*i*Pr)$_4$; 155 μL, 529 μmol), 6-azido-1-hexanol (981 μL, 7.05 mmol), and toluene (1.0 mL) were added to a Schlenk flask under argon. The mixture was stirred at 80 °C for 1 h and then cooled with liquid nitrogen. The solvent and the isopropanol generated from the Ti(O*i*Pr)$_4$ were removed by evaporation. A solution of **S4M4** (1.50 g, 177 μmol) in toluene (10.4 mL) was added to the flask. The mixture was stirred at 100 °C for 1 week and cooled with liquid nitrogen. THF and QuadraSil™ AP were added to the mixture, which was subsequently stirred for 1 h. The mixture was passed through a short column with combined alumina and silica gel. After removal of the solvent, the residue was dialyzed with a cellophane tube (Spectra/Por® 6 Membrane; MWCO: 1,000) in acetone and finally reprecipitated from THF solution into hexane to give **S4M4-N$_3$** as a white powder. Yield: 63.0%. $M_{n,SEC}$ = 9,380 g mol$^{-1}$, $Đ$ = 1.03 (THF). $^1$H NMR (400 MHz, $CDCl_3$): $\delta$ 7.32−6.26 (br, aromatic), 4.02 (m, 2H, −C$H_2$(CH$_2$)$_5$N$_3$), 3.82−3.38 (br, −OC$H_3$, PMMA), 3.29 (t, $J$ = 6.6 Hz, 2H, −C$H_2$N$_3$), 2.47 (br, $\omega$-terminal proton), 2.24−0.77 (br, main chain −C$H_2$C−, −CC$H_3$, −CH$_2$C*H*−, −C$H_2$CH−, PMMA, PS), 1.13 (d, $J$ = 7.3 Hz, 2H, −C$H_2$CH(CH$_3$)(COO(CH$_2$)$_6$N$_3$)). **S6M3-N$_3$** (Yield: 65.8%; $M_{n,SEC}$ = 9,470 g mol$^{-1}$, $Đ$ = 1.03 (THF); $M_{n,SEC}$ = 8,780 g mol$^{-1}$, $Đ$ = 1.07 (DMF)) and **S3M6-N$_3$** (Yield: 45.0%; $M_{n,SEC}$ = 9,590 g mol$^{-1}$, $Đ$ = 1.03 (THF); $M_{n,SEC}$ = 8,640 g mol$^{-1}$, $Đ$ = 1.07 (DMF)) were prepared by following the above-described procedure.

**Click Reaction of Azido-Functionalized PS-*b*-PMMA and Ethynyl-Functionalized Mono/oligosaccharides**

The following is a typical click-reaction procedure (Procedure A). **S4M4-N$_3$** (300 mg, 35.3 μmol), **HC≡C-MT** (30.9 mg, 52.9 μmol), and CuCl (10.5 mg, 106 μmol) were added to a Schlenk flask, and purged with argon. PMDETA (44.3 μL, 212 μmol) and DMF (5.0 mL) were added to the flask. The reaction mixture

was stirred at room temperature for 24 h and then passed through a short column of silica gel with THF as the eluent. The solvent was removed to give **S4M4-MT** as a white powder. Yield: 66.7%; $M_{n,SEC}$ = 11,900 g mol$^{-1}$, $Đ$ = 1.14 (DMF). $^1$H NMR (DMF-$d_7$): $\delta$ 8.25 (br, triazole methine), 7.49−6.41 (br, aromatic), 6.08, 5.85, 5.72, 5.62, 5.21−5.11, 5.06, 5.00, 4.75, 4.66, 4.57−4.38 (sugar protons), 4.06 (br, −C$H_2$(CH$_2$)$_5$N$_3$), 3.60 (br, −OC$H_3$, PMMA), 2.28−0.80 (br, main chain −C$H_2$C−, −CC$H_3$, −CH$_2$C$H$−, −C$H_2$CH−, PMMA, PS). **S4M4-MH** (Yield: 64.6%; $M_{n,SEC}$ = 16,400 g mol$^{-1}$, $Đ$ = 1.16 (DMF)), **S4M4-Glc** (Yield: 48.5%; $M_{n,SEC}$ = 10,000 g mol$^{-1}$, $Đ$ = 1.12 (DMF)), **S6M3-MT** (Yield: 60.4%; $M_{n,SEC}$ = 12,500 g mol$^{-1}$, $Đ$ = 1.12 (DMF)), and **S3M6-MT** (Yield: 70.0%; $M_{n,SEC}$ = 12,300 g mol$^{-1}$, $Đ$ = 1.07 (DMF)) were prepared by following the above-described procedure.

### *4.2.5 Synthesis of Poly(methyl methacrylate) bearing A Maltotriose at the ω-Chain End*

**Anionic Polymerization of Methyl Methacrylate**

The following is a typical procedure for the anionic polymerization of methyl methacrylate. *sec*-Butyllithium (*sec*-BuLi; 0.98 mol L$^{-1}$, 771 μL, 755 μmol), 1.1-diphenylethylene (DPE; 199 μL, 1.13 mmol), and a solution of LiCl in hexane (1.0 mol L$^{-1}$, 1.51 mL, 1.51 mmol) were sequentially added to THF (69.0 mL) at −78 °C, and the mixture was stirred for 30 min. Methyl methacrylate (MMA; 4.00 mL, 37.8 mmol) was added to the mixture and polymerization was terminated after 1 h by the addition of a small amount of methanol. The mixture was diluted with THF and passed through a short column of alumina. After removal of the solvent, the crude product was dialyzed with a cellophane tube (Spectra/Por® 6 Membrane; MWCO: 1,000) in acetone and finally precipitated from THF solution into hexane to give **M4** as white powder (Yield: 86.9%; $M_{n,NMR}$ = 4,170 g mol$^{-1}$; $M_{n,SEC}$ = 4,860 g mol$^{-1}$, $Đ$ = 1.07 (THF)). $^1$H NMR (CDCl$_3$): $\delta$ 7.32−7.08 (br, 10H, aromatic), 3.82−3.38 (br, −OC$H_3$), 2.49 (br, −C$H$(CH$_3$)(COOCH$_3$), 2.24−1.36 (br, main chain −C$H_2$C−), 1.36−0.77 (br, $\alpha$−C$H_3$), 1.13 (d, $J$ = 6.7 Hz, 2H, −C$H_2$CH(CH$_3$)(COO(CH$_3$)). **M6** (Yield: 29.7%; $M_{n,NMR}$ = 6,340 g mol$^{-1}$; $M_{n,SEC}$ = 6,710 g mol$^{-1}$, $Đ$ = 1.06 (THF)) was prepared by following the above-described procedure.

**Terminal-Selective Transesterification of PMMA using 6-Azido-1-hexanol**

Titanium isopropoxide (Ti(O*i*Pr)$_4$) (211 µL, 719 µmol), 6-azido-1-hexanol (1.33 mL, 9.59 mmol), and toluene (1.0 mL) were added to a Schlenk flask under argon. The mixture was stirred at 80 °C for 1 h and then cooled with liquid nitrogen. The solvent and the isopropanol generated from the Ti(O*i*Pr)$_4$ were removed by evaporation during return to room temperature. A solution of **M4** (1.00 g, 240 µmol) in toluene (12.8 mL) was added and the mixture was stirred at 100 °C for 1 week and cooled with liquid nitrogen to terminate the reaction. THF and QuadraSil™ AP were added to the mixture after which it was stirred for 1 h. The mixture was passed through a short column with combined alumina and silica gel. After removal of the solvent, the residue was dialyzed with a cellophane tube (Spectra/Por® 6 Membrane; MWCO: 1,000) in acetone and finally reprecipitated from THF solution into hexane to give **M4-N$_3$** as white powder. Yield: 70.0%. $M_{n,NMR}$ = 4,350 g mol$^{-1}$, $M_{n,SEC}$ = 4,920 g mol$^{-1}$, $Đ$ = 1.06 (THF), $M_{n,SEC}$ = 4,480 g mol$^{-1}$, $Đ$ = 1.08 (DMF). $^1$H NMR (400 MHz, $CDCl_3$): $\delta$ 7.25−7.08 (br, 10H, −C(*Ph*)$_2$), 4.02 (m, 2H, −C*H*$_2$(CH$_2$)$_5$N$_3$), 3.60 (−OC*H*$_3$, PMMA) , 3.29 (t, $J$ = 6.6 Hz, 2H, −C*H*$_2$N$_3$), 0.60−2.12 (br, main chain −C*H*$_2$C−, −CC*H*$_3$), 0.59−0.52 (m, $\alpha$-terminal −C*H*$_3$, −CH$_2$C*H*$_3$). **M6-N$_3$** (Yield: 48.4%; $M_{n,NMR}$ = 6,290 g mol$^{-1}$; $M_{n,SEC}$ = 6,860 g mol$^{-1}$, $Đ$ = 1.04 (THF); ; $M_{n,SEC}$ = 5,910 g mol$^{-1}$, $Đ$ = 1.06 (DMF)) was prepared by following the above-described procedure.

**Click Reaction of Azido-Functionalized PMMA and Ethynyl-Functionalized Maltotriose**

The click reaction described in Procedure A was followed using **M4-N$_3$** (350 mg, 35.3 µmol), **HC≡C-MT** (30.9 mg, 52.9 µmol), CuCl (10.5 mg, 106 µmol), and PMDETA (44.3 µL, 212 µmol) in DMF (5.0 mL) to give **M4-MT** as white powder. Yield: 66.7 %; $M_{n,SEC}$ = 8,690 g mol$^{-1}$, $Đ$ = 1.19 (DMF). **M6-MT** (Yield: 33.3 %; $M_{n,SEC}$ = 10,500 g mol$^{-1}$, $Đ$ = 1.17 (DMF)) was prepared by following the above-described procedure.

### *4.2.6 Synthesis of Polystyrene bearing A Maltotriose at the ω-Chain End*

**Atom Transfer Radical Polymerization of Styrene**

CuBr (17.9 mg, 125 µmol) was added to a round-bottom flask. The flask was sealed with a septum and purged with argon. Degassed styrene (11.0 mL, 1.25 mmol), PMDETA (26.0 µL, 125 µmol), and 1-PEBr (169 µL, 125 µmol) were sequentially added to the flask, and the reaction mixture was stirred at 110 °C for

11 h. Polymerization was quenched by cooling with liquid nitrogen. The mixture was diluted with THF and passed through a short column of silica gel to remove the copper complex. After removal of the solvent by evaporation, the residue was reprecipitated three times from THF solution into methanol to give **S5** as a white powder. Yield: 27.3%. $M_{n,NMR}$ = 4,730 g mol$^{-1}$; $M_{n,SEC}$ = 3,930 g mol$^{-1}$, $Đ$ = 1.09 (THF). $^1$H NMR ($CDCl_3$) $\delta$ 7.32−6.26 (br, aromatic), 4.62−4.33 (br, 1H, −$CH_2CH$(Ph)Br), 2.15−1.69 (br, main chain −$CH_2CH$−, PS), 1.69−1.22 (br, main chain −$CH_2$CH−, PS), 1.12−0.94 (br, 1H, $CH_3$CH−). **S3** (Yield: 12.0%; $M_{n,NMR}$ = 3,430 g mol$^{-1}$; $M_{n,SEC}$ = 2,350 g mol$^{-1}$, $Đ$ = 1.14 (THF)) was prepared by following the above-described procedure.

**End-Functionalization of Polystyrene using Sodium Azide**

**S5** (2.00 g, 423 μmol), $NaN_3$ (137 mg, 2.11 mmol), and DMF (10.0 mL) were added to a round-bottom flask. The reaction mixture was stirred at room temperature for 24 h. After the addition of water, the mixture was extracted three times with diethyl ether. The combined organic layers were washed with water and dried over $MgSO_4$. The crude product was reprecipitated from THF solution into methanol to give **S5-N$_3$** as a white powder. Yield: 85.0%. $M_{n,NMR}$ = 4,940 g mol$^{-1}$; $M_{n,SEC}$ = 3,950 g mol$^{-1}$, $Đ$ = 1.07 (THF), $M_{n,SEC}$ = 3,490 g mol$^{-1}$, $Đ$ = 1.08 (DMF). $^1$H NMR ($CDCl_3$) $\delta$ 7.40−6.28 (br, aromatic), 4.05−3.82 (br, 1H, −$CH_2CH$(Ph)$N_3$), 2.50−1.15 (br, main chain −$CH_2CH$(Ph)−), 1.12−0.92 (br, 1H, $CH_3$CH(Ph)−). **S3-N$_3$** (Yield: 12.0%; $M_{n,NMR}$ = 3,430 g mol$^{-1}$; $M_{n,SEC}$ = 2,430 g mol$^{-1}$, $Đ$ = 1.14 (THF); $M_{n,SEC}$ = 2,710 g mol$^{-1}$, $Đ$ = 1.07 (DMF)) was prepared by following the above-described procedure.

**Click Reaction of Azido-Functionalized PMMA and Ethynyl-Functionalized Maltotriose**

The click reaction described in Procedure A was followed using **S5-N$_3$** (300 mg, 35.3 μmol), **HC≡C-MT** (30.9 mg, 52.9 μmol, CuCl (10.5 mg, 106 μmol), and PMDETA (44.3 μL, 212 μmol) in DMF (5.0 mL) to give **S5-MT** as white powder. Yield: 66.7%; $M_{n,SEC}$ = 5,160 g mol$^{-1}$, $Đ$ = 1.10 (DMF). **S3-MT** (Yield: 22.7%; $M_{n,SEC}$ = 4,760 g mol$^{-1}$, $Đ$ = 1.13 (DMF)) was prepared by following the above-described procedure.

### *4.2.7 Small-Angle X-ray Scattering Experiments*

Small-angle X-ray scattering (SAXS) experiments for bulk samples were performed on BL-6A beamline of the Photon Factory of High Energy Accelerator Research Organization (KEK, Tsukuba, Japan).

The X-ray wavelength and exposure time were 1.50 Å (8.27 keV) and 60 s, respectively. A PILATUS3 1M (Dectris Ltd., Switzerland) detector, with 981 × 1043 pixels at a pixel size of 172 × 172 μm, and a counter depth of 20 bits (1,048,576 counts), was used for data acquisition. The sample-to-detector distance was calibrated using the scattering patterns of silver behenate (Nagara Science Co., Ltd., Japan). Bulk samples for SAXS experiments were placed in 1.5-mm-diameter Lindemann glass capillaries (Hilgenderg, Germany) and annealed under vacuum at 180 °C for 3 h. The SAXS data were acquired under ambient conditions, and 1D profiles were obtained as plots of scattering intensity as functions of scattering vector ($q$), where $q = (4\pi/\lambda)\sin(\theta/2)$ ($\lambda$, wave length; $\theta$, scattering angle).

### *4.2.8 Thin-Film Preparation*

Polymer thin films for morphological analyses were prepared by spin-coating (2000 rpm, 60 s) a 2-wt% polymer solution in DMF onto Si (100) substrates with native oxide surfaces under ambient conditions. The thin-film samples were thermally annealed at 180 °C for 3 h under reduced pressure. The film thickness was measured by ellipsometry (JASCO M-500S).

### *4.2.9 Atomic Force Microscopy Experiments.*

Atomic force microscopy (AFM) was performed using a PicoPlus atomic force microscope and operated in tapping mode using a silicon cantilever (NANOSENSORS™ PPP-NCH, NanoWorld AG, Switzerland) with a resonance frequency of 330 kHz and a force constant of 42 N $m^{-1}$. Image data were processed with Gwyddion software.

### *4.2.10 Grazing-Incidence SAXS Experiments.*

Grazing incidence SAXS (GISAXS) experiments on the polymer thin films were performed at the BL-6A beamline of KEK using 1.50 Å (8.27 keV) X-ray radiation. The sample-to-detector distance was calibrated using the scattering patterns of silver behenate (Nagara Science Co., Ltd., Japan). The GISAXS profiles were acquired under ambient conditions for 20 s at a variety of incidence angles.

## 4.3 Results and Discussion

### *4.3.1 Synthesis*

PS-*b*-PMMAs bearing mono/oligosaccharides, *i.e.*, maltoheptaose (MH), maltotriose (MT), and glucose (Glc), at the PMMA chain ends (**SM-MH**, **SM-MT**, and **SM-Glc**, respectively) were synthesized by chain-end functionalization followed by click chemistry, as shown in Scheme 4.1. Recently, Sawamoto *et al.* reported a novel end-functionalization strategy for chlorine-terminated PMMA, which is referred to as "terminal-selective transesterification".[13] Titanium alkoxide transesterifies PMMA only at the $\omega$-terminal MMA unit to give the $\omega$-chain-end-functionalized PMMA. Importantly, since terminal selectivity is mainly due to differences in steric hindrance, the terminal-selective transesterification is expandable to BCP systems bearing PMMA $\omega$-chain ends.

Transesterification was carried out on a PS-*b*-PMMA with a molecular weight of 8.50 kg mol$^{-1}$ and a PS volume fraction ($f_{St}$) of 0.52 (**S4M4**) using the titanium alkoxide ($Ti(OR)_4$) of 6-azido-1-hexanol in toluene at 100 °C under an atmosphere of argon. Note that S, M, and the numbers in the polymer name refer to PS, PMMA, and the molecular weight (kg mol$^{-1}$) of each block, respectively. Size-exclusion chromatography (SEC) of the product revealed a narrow dispersity ($Đ$), even after the reaction, consistent with a lack of side reactions, such as degradation and intermolecular coupling (Figure 4.1a). The FT-IR spectrum of the product indicated that the azido group had been introduced into the PS-*b*-PMMA, as evidenced by the new absorption peak at 2098 cm$^{-1}$ that corresponds to the azido stretching vibration (Figure 4.2). The $^1$H NMR spectrum displays minor signals at 4.02 and 3.29 ppm due to the methylene protons adjacent to the ester and azido groups of the incorporated azidohexyl moiety, respectively (protons *D* and *E* in Figure 4.3). In addition, the integration ratio of these signals reveals that transesterification proceeded in almost quantitatively. Importantly, the minor signal due to the $\omega$-terminal proton of the main chain clearly shifted from 2.49 to 2.47 ppm following reaction (proton *C*' in Figures 4.3), which indicates that the methyl ester moiety of the $\omega$-terminal MMA unit had been replaced by the azidohexyl group. Additional investigations using a PMMA homopolymer provided further evidence in support of the quantitative and $\omega$-terminal-selective transesterification reaction (see Chapter 3). Importantly, matrix-assisted laser desorption/ionization-time-of-flight mass spectrometry (MALDI-TOF MS) revealed that the modified

PMMA does indeed possess an azidohexyl-ester group and that PMMA units with multiple azidohexyl-ester groups did not form (Figure 4.4). Therefore, the author confirmed that a well-defined $\omega$-azido-functionalized **S4M4** (**S4M4-N$_3$**) was produced.

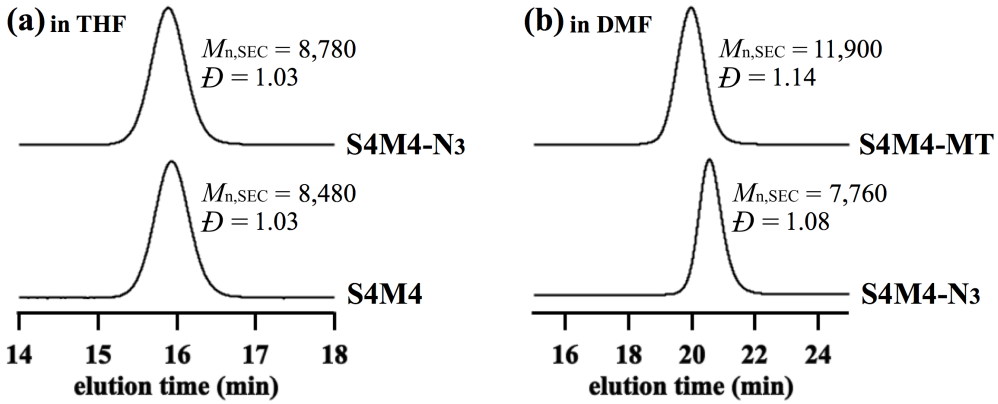


**Figure 4.1**. SEC traces of (a) **S4M4-N$_3$** (upper) and **S4M4** (lower) (eluent, THF; flow rate, 1.0 mL min$^{-1}$) and (b) **S4M4-MT** (upper) and **S4M4-N$_3$** (lower) (eluent, DMF containing 0.01 mol L$^{-1}$ LiCl; flow rate, 0.60 mL min$^{-1}$).

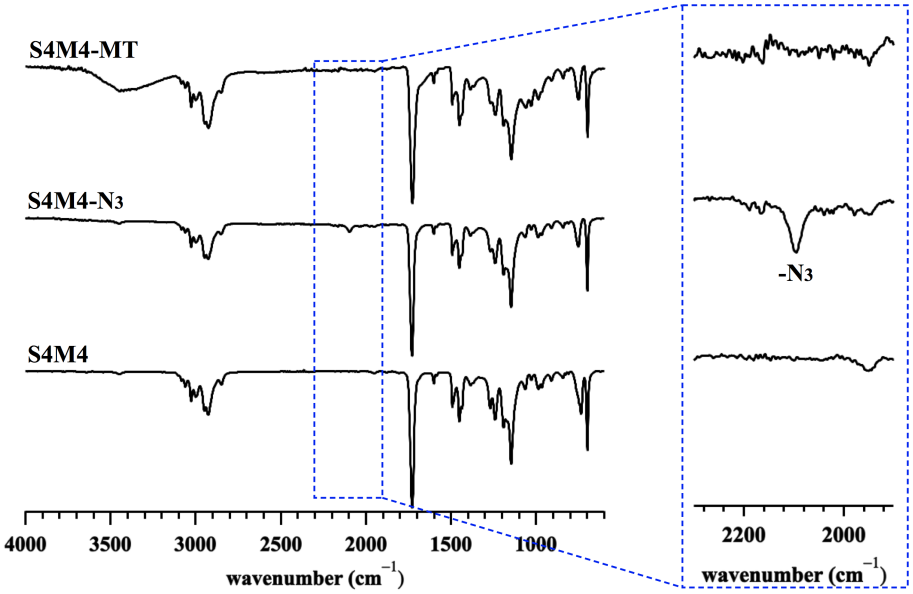


**Figure 4.2**. FT-IR spectra of **S4M4-MT** (upper), **S4M4-N$_3$** (middle), and **S4M4** (lower).

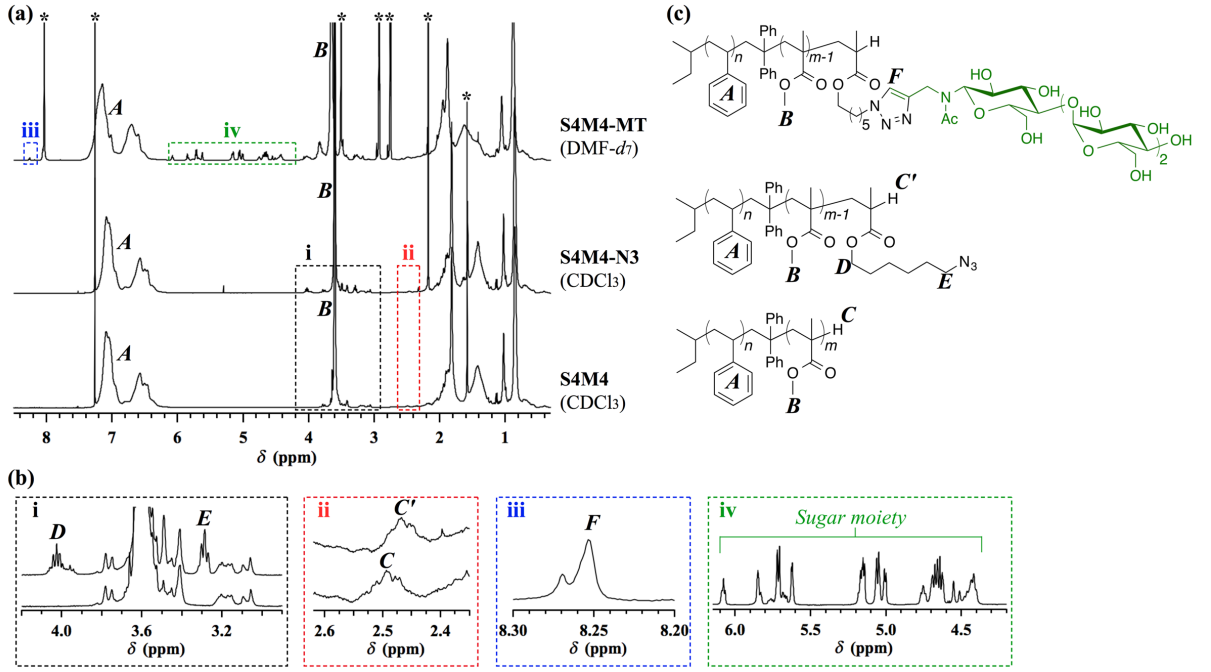


**Figure 4.3**. NMR analysis of **S4M4-MT**. (a) $^{1}$H NMR spectra of **S4M4-MT** in DMF-$d_7$ (upper), **S4M4-N$_3$** in $CDCl_3$ (middle), and **S4M4** in $CDCl_3$ (lower) (400 MHz). (b) Expanded spectra of **S4M4-N$_3$** and **S4M4** in the (i) 4.20−2.90 and (ii) 2.62−2.35 ppm region, and **S4M4-MT** in the (iii) 8.30−8.20 and (iv) 6.15−4.20 ppm region. (c) Expected chemical structures and peak assignments.

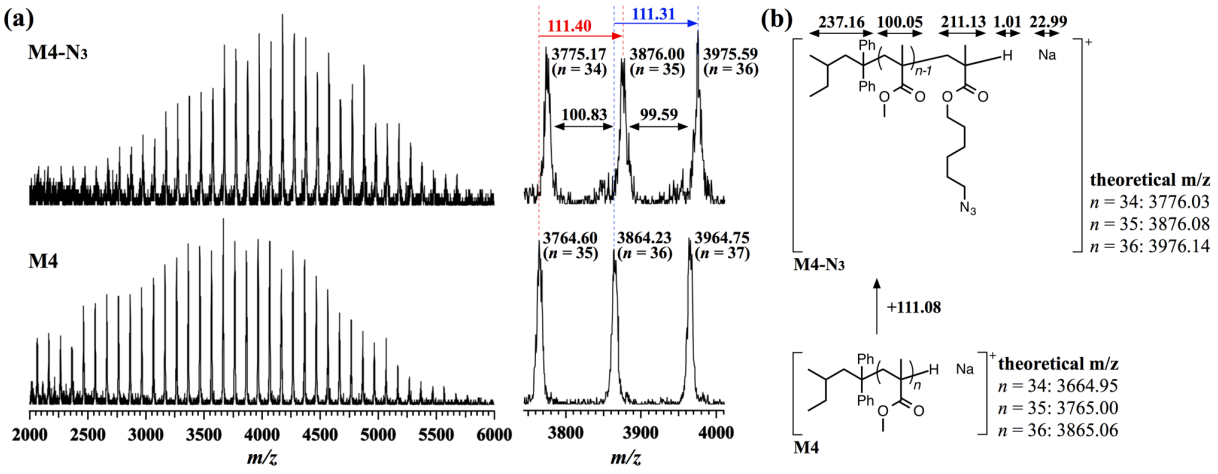


**Figure 4.4**. (a) MALDI-TOF mass spectra and (b) expected chemical structure of **M4-N$_3$** and **M4**.

**S4M4-$N_3$** was then click reacted with *N*-maltotriosyl-3-acetamido-1-propyne (**HC≡C-MT**) to produce an **S4M4** bearing an MT moiety at the PMMA chain end (**S4M4-MT**). The click reaction was performed in DMF at 40 °C under argon in the presence of the CuCl/PMDETA (*N*,*N*,*N'*,*N''*,*N''*-pentamethyldiethylenetriamine) catalyst, with a slight excess of **HC≡C-MT** with respect to the azido groups of **S4M4-$N_3$**. The SEC trace of the product following the reaction exhibited a peak that was shifted to higher molecular weight compared to the starting material, while maintaining a narrow *Đ* (Figure 4.1). The peak at 2098 $cm^{-1}$ in the initial FT-IR spectrum, which is due to the azido group, was completely absent in the spectrum of the product, while a new absorption peak at around 3400 $cm^{-1}$, due to O-H stretching vibrations of the MT moiety, appeared following the reaction (Figure 4.2). The $^1$H NMR spectrum of the product revealed the proton signals that correspond to the PS, PMMA, and MT moieties (Figure 4.3). More importantly, a signal attributable to the triazole proton was observed at 8.25 ppm (proton *F* in Figure 4.3), confirming the successful formation of the triazole linkage between the PMMA and MT blocks to afford the desired **S4M4-MT**. The click reactions of **S4M4-$N_3$** with *N*-maltoheptaosyl-3-acetamido-1-propyne (**HC≡C-MH**) and 1-propargyl-*β*-D-glucopyranoside (**HC≡C-Glc**) were also performed under the same conditions to yield **S4M4-MH** and **S4M4-Glc**, respectively.

**Table 4.1**. Properties of the synthesized polymers bearing mono/oligosaccharide at their *ω*-chain ends

| Polymer name | $M_{n,total}$[a] (g $mol^{-1}$) | $M_{n,SEC}$[b] (g $mol^{-1}$) | $Đ$[b] | $f_{St}$[c] | $f_{MMA}$[c] | $f_{sugar}$[c] |
|---|---|---|---|---|---|---|
| **S4M4-MH** | 10,000 | 16,400 | 1.16 | 0.46 | 0.43 | 0.11 |
| **S4M4-MT** | 9,360 | 11,900 | 1.14 | 0.49 | 0.46 | 0.05 |
| **S4M4-Glc** | 9,040 | 10,000 | 1.12 | 0.51 | 0.47 | 0.02 |
| **S6M3-MT** | 10,100 | 12,500 | 1.12 | 0.65 | 0.30 | 0.05 |
| **S3M6-MT** | 10,200 | 12,300 | 1.12 | 0.33 | 0.62 | 0.05 |
| **S5-MT** | 5,310 | 5,160 | 1.10 | 0.91 | 0.00 | 0.09 |
| **S3-MT** | 4,020 | 4,760 | 1.13 | 0.88 | 0.00 | 0.12 |
| **M6-MT** | 6,930 | 10,500 | 1.17 | 0.00 | 0.93 | 0.07 |
| **M4-MT** | 4,700 | 8,690 | 1.19 | 0.00 | 0.89 | 0.11 |

[a]Calculated as ($M_n$ of **SM-$N_3$**, **S-$N_3$**, and **M-$N_3$**) + (M.W. of **HC≡C-MT**). [b]Determined by SEC in DMF (containing 0.01 mol $L^{-1}$ LiCl) using PS standards for **SM-MT** and **S-MT**, and PMMA standards for **M-MT**. [c]Volume fractions (*f*) were calculated using $d_{PS}$ = 1.05 g $cm^{-3}$, $d_{PMMA}$ = 1.18 g $cm^{-3}$, and $d_{amylose}$ = 1.36 g $cm^{-3}$.

**SM-MT**s with different compositions, namely **S6M3-MT** and **S3M6-MT**, were also prepared in the same manner, starting from **S6M3** ($M_n$ of PS-*b*-PMMA = 9.20 kg mol$^{-1}$, $f_{St}$ = 0.68) and **S3M6** ($M_n$ of PS-*b*-PMMA = 9.20 kg mol$^{-1}$, $f_{St}$ = 0.35), respectively (Table 4.1). All prepared **SM-MT**s have comparable MT volume fractions ($f_{sugar}$ = 0.05). The author also synthesized PS and PMMA homopolymers bearing MT moieties at their $\omega$-chain ends (**S-MT**s and **M-MT**s, respectively; Table 4.1) to gain a better understanding of the microphase-separation behavior of the prepared BCP systems.

### *4.3.2 Microphase Separation in Bulk*

Mono/oligosaccharide-terminated polymers, as well as the corresponding starting materials, were investigated in their bulk states by the small angle X-ray scattering (SAXS) technique. The samples were thermally annealed at 180 °C for 3 h and then rapidly quenched, after which their SAXS profiles were acquired at room temperature. The author initially investigated the effect of the degree of polymerization of the mono/oligosaccharide moiety on microphase separation. Figure 4.5a displays the SAXS profiles of a series of **S4M4** polymers with various mono/oligosaccharides at their PMMA chain ends (**S4M4-MH**, **S4M4-MT**, and **S4M4-Glc**), as well as their precursors. The SAXS data for **S4M4** and **S4M4-N$_3$** reveal completely disordered states, as evidenced by a lack of characteristic scattering. However, the mono/oligosaccharide-terminated **S4M4**s clearly exhibited scattering patterns consistent with microphase separation, which indicates that the introduction of mono/oligosaccharide units significantly promotes microphase separation. Although the weak scattering peak observed in the SAXS profile of **S4M4-Glc** suggested a slight enhancement in segregation strength between the blocks for PS-*b*-PMMA with low *N*, Glc was unable to induce a well-ordered microphase-separated structure. On the other hand, **S4M4-MT** exhibits a principle scattering peak ($q^*$) together with higher-order scattering peaks that are related to a well-ordered microphase-separated structure, indicating that the MT component strongly assists **S4M4** microphase separation. Although **S4M4-MH** also exhibits a characteristic scattering pattern due to microphase separation, the broadness of the scattered peaks are suggestive of the lack of a long-range ordered structure. This unexpected **S4M4-MH** result should be attributable to the following reasons: the strong aggregation of MH component

decreased the whole chain mobility; the rigid nature of MH resulted in distorting the phase diagram; and **S4M4-MH** may locate near the order-disorder phase boundary due to the increased volume fraction of the PMMA-MH block.[2,14,15] As a result, the author conclude that MT has suitable characteristics for inducing the microphase separation of low-*N* PS-*b*-PMMA. To the best of the knowledge, this is the first experimental report of an intrinsically completely disordered BCP forming a well-ordered morphology solely as a result of the installation of a hydrophilic component at the chain end, and without any other chemical alterations. This result can be ascribable to several reasons, such as the improvement in the segregation strength between the PS and PMMA-saccharide blocks due to increased hydrophilicity of the PMMA-saccharide block, promotion of interchain aggregation to form core-shell type structure by the intermolecular hydrogen bonding between the saccharide segments, and enhancement of the self-attraction within the PMMA block via the hydrogen bonding with the saccharides.

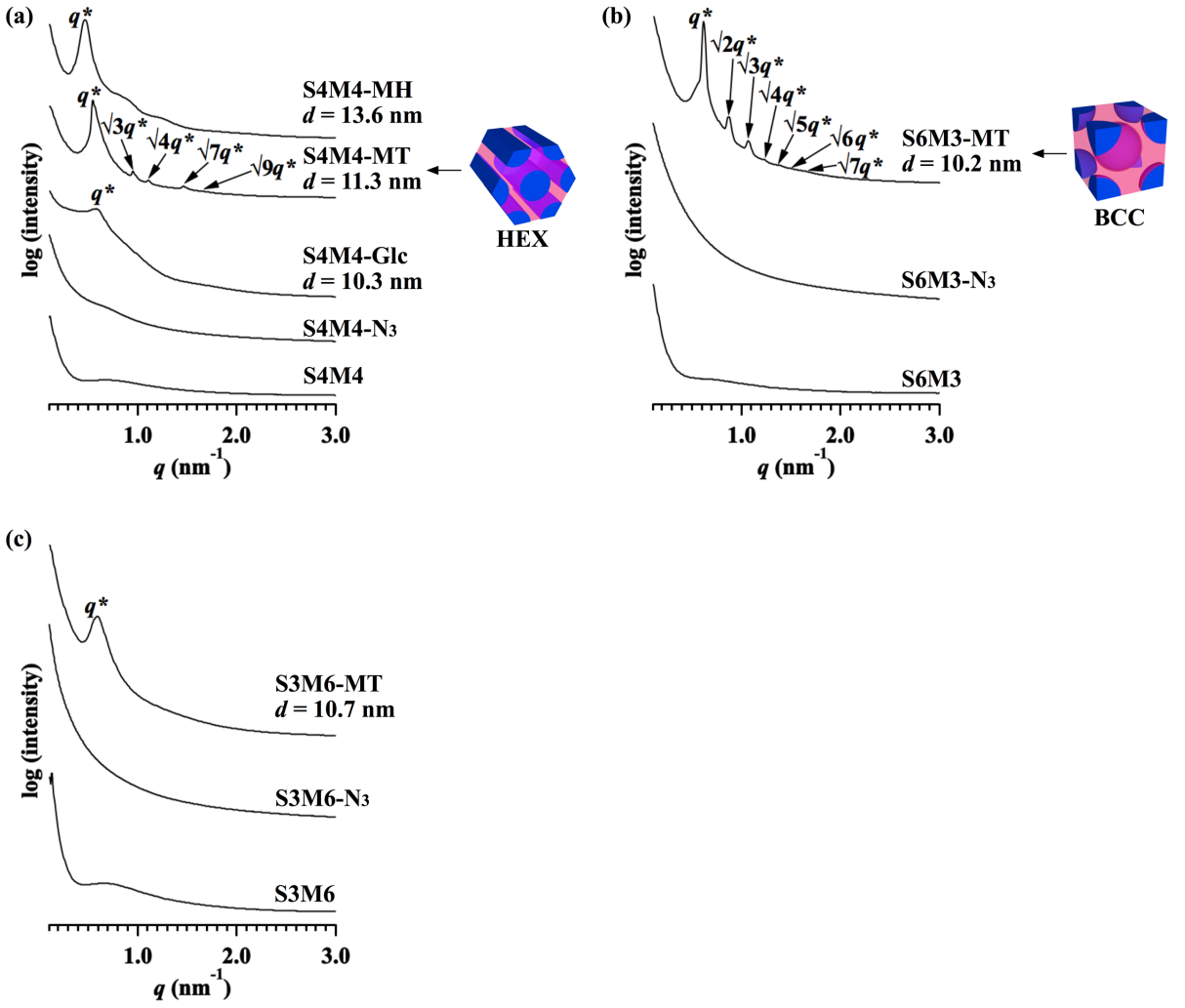


**Figure 4.5**. SAXS profiles of (a) **S4M4-MH**, **S4M4-MT**, **S4M4-Glc**, (b) **S6M3-MT**, and (c) **S3M6-MT**, and the corresponding **SM-N$_3$**s and PS-*b*-PMMAs. The profiles of all bulk samples were acquired at room temperature after thermal annealing at 180 °C for 3 h.

The author next further investigated the impact of the MT moiety on microphase separation by examining a series of **SM-MT**s of different composition (**S6M3-MT**, **S4M4-MT**, and **S3M6-MT**). The SAXS profile of **S6M3-MT** exhibits a characteristic scattering pattern attributable to microphase separation, while those of the corresponding precursors, **S6M3** and **S6M3-N$_3$**, reveal the absence of microphase-

separated structures (Figure 4.5b). In addition to the principal scattering peak ($q^*$) observed at a value of 0.616 $nm^{-1}$, higher-order scattering peaks appeared at $q/q^* = \sqrt{2}, \sqrt{3}, \sqrt{4}, \sqrt{5}, \sqrt{6}$, and $\sqrt{7}$, which correspond to a body-centered cubic (BCC) phase. The domain spacing ($d_{SAXS}$) was calculated to be 10.2 nm based on the relationship: $d_{SAXS} = 2\pi/q^*$, which corresponds to the (110) lattice spacing of BCC. The spherical microdomain should be a composite of PMMA and MT blocks because the PS blocks have significantly greater volumes than the remaining blocks, and the volume fraction of the MT ($f_{sugar}$) itself is insufficient for microdomain formation. The spherical radius ($R_S$) of the BCC was calculated to be 5.0 nm by the relationship: $R_S = [3(f_{PMMA}+f_{sugar})d_{SAXS}^3/(\sqrt{8}\pi)]^{1/3}$.

**S4M4-MT**, with a comparable $f_{sugar}$ to **S6M3-MT**, was expected to form a lamellar (LAM) structure because of the symmetric PS- and PMMA-MT-block volume fractions. However, contrary to our expectations, the SAXS profile of **S4M4-MT** exhibits a scattering pattern characterized by peak positions at $q/q^* = 1, \sqrt{3}, \sqrt{4}, \sqrt{7}$, and $\sqrt{9}$ that correspond to a hexagonally close-packed cylinder (HEX) (Figure 4.5a). Given that the microdomain shifted from BCC for **S6M3-MT** to HEX for **S4M4-MT** in response to an increase in the PMMA volume fraction ($f_{PMMA}$), the cylindrical microdomain of **S4M4-MT** should be composed of PMMA and MT segments. If the microphase-separation behavior of **S4M4-MT** is governed by the phase diagram of a typical diblock copolymer, a LAM structure should be generated because of the volume-fraction symmetries of the PS and MT-terminated PMMA blocks. The strong aggregation of MT results in an increase in the packing density of the PMMA-MT domain and a decrease in its effective volume fraction, which leads to the formation of HEX, but not LAM. The $d_{SAXS}$ was calculated to be 11.3 nm from the $q^*$ value of 0.555 $nm^{-1}$, where the $d_{SAXS}$ of HEX corresponds to the (100) lattice spacing. The cylinder radius ($R_C$) was calculated to be 4.9 nm using the relationship: $R_C = [(4/3)^{1/2}(f_{PMMA}+f_{MT})d_{SAXS}^2/\pi]^{1/2}$. Hence, the author successfully produced a markedly small periodic structure using PS-*b*-PMMA with only minor chain-end modifications.

A principal scattering peak due to microphase separation was observed in the SAXS profile of **S3M6-MT**; however, the morphology could not be determined owing to a lack of higher-order scattering peaks (Figure 4.5c), which is ascribable to the insufficient ability of MT to enhance the hydrophilicity of the relatively large PMMA block.

Overall, these results indicate that terminal MT moieties at the PMMA chain ends of **SM-MT**s lead to enhanced segregation strength between the PS and PMMA blocks, which contributes to microphase separation even in the low *N* region. It should be noted that microphase-separated structures with such small domain spacings are particularly beneficial for 10-nm-scale nanofabrication purposes using BCPs as nanotemplates.

To confirm the importance of installing an oligosaccharide at the chain end, the author studied blended samples of PS-*b*-PMMA and MT by SAXS. The blended samples were prepared by dissolving PS-*b*-PMMA and MT in DMF at the same weight ratio as the corresponding **SM-MT**s, followed by removal of the solvent and thermal annealing under the same conditions as described above. The SAXS profiles of the blended samples exhibited featureless scattering similar to those of the corresponding PS-*b*-PMMAs (Figure 4.6), which suggests that free oligosaccharide molecules segregate from the polymer phase to facilitate macrophase separation. Therefore, tethering the oligosaccharide and PMMA segments is an essential structural requirement for producing microphase-separated structures from low-*N* PS-*b*-PMMAs.

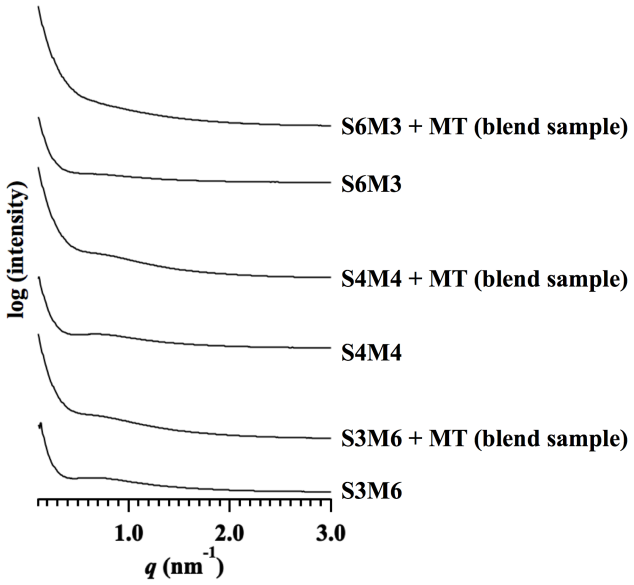


**Figure 4.6.** SAXS profiles of MT-blended PS-*b*-PMMAs and the corresponding PS-*b*-PMMAs. All blended samples were prepared by blending in DMF followed by drying under reduced pressure at 180 °C for 3 h. The SAXS profiles were acquired at room temperature.

In addition, the author investigated the bulk morphologies of PS and PMMA homopolymers with MT segments at their chain ends (**S-MT**s and **M-MT**s, respectively) by SAXS to gain further insight into the microphase-separation behavior of the **SM-MT**s. The bulk **S-MT** and **M-MT** samples were prepared using the same process described for the preparation of the **SM-MT**s. Interestingly, the SAXS profiles of **S-MTs** with PS molecular weights of 3.4 and 4.7 kg mol$^{-1}$ (**S3-MT** and **S5-MT**, respectively) clearly exhibit scattering patterns that correspond to BCC phases (Figure 4.7). Although **M-MT**s with PMMA molecular weights of 4.1 and 6.3 kg mol$^{-1}$ (**M4-MT** and **M6-MT**, respectively) exhibit scattering due to microphase separation, the broadness of the scattering peaks suggest a lack of well-ordered microphase-separated structures. These results reveal that the PS block is strongly incompatible with the MT moiety, and that the segregation strength between PMMA and MT is insufficient to drive well-ordered microphase separation. This further supports the hypothesis that the microdomains in the microphase-separated **S6M3-MT** and **S4M4-MT** are composed of PMMA and MT; the PMMA blocks and MT moieties are possibly weakly segregated in the microdomain (Figure 4.8).

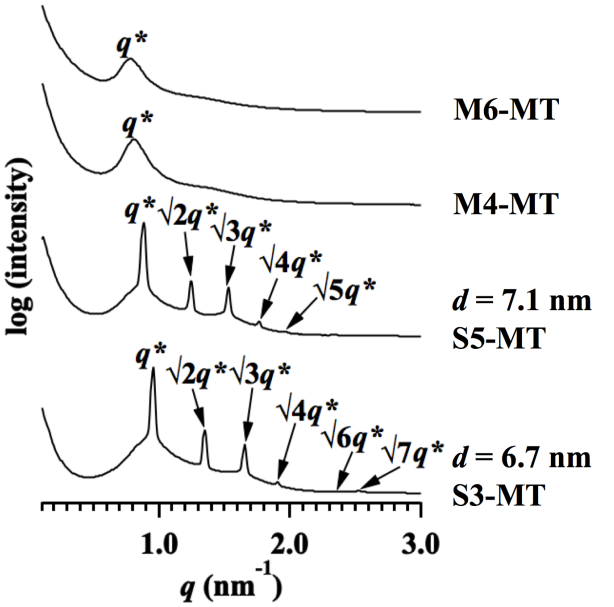


**Figure 4.7**. SAXS profiles of the **S-MT**s and **M-MT**s. Profiles of all bulk samples were acquired at room temperature after thermal annealing at 180 °C for 3 h.

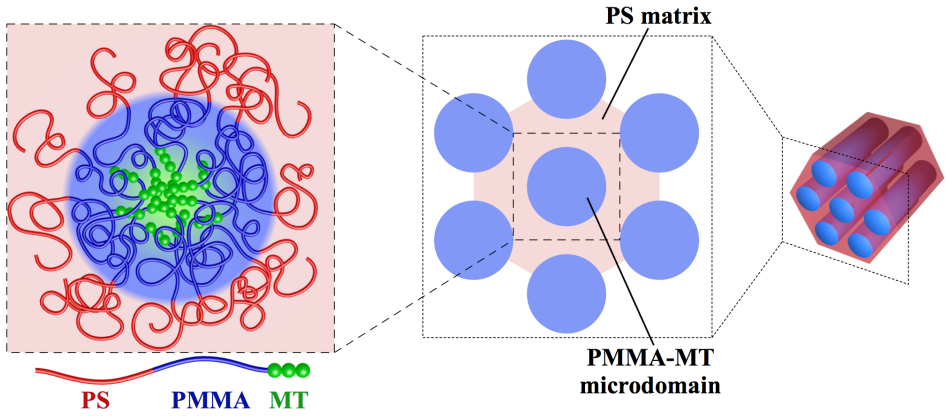


**Figure 4.8.** Schematic illustration of plausible chain packing structure in a **SM-MT** microdomain.

### *4.3.3 Microphase Separation in Thin Film*

The author next subjected thin films of **S6M3-MT** and **S4M4-MT** to atomic force microscopy (AFM) to visualize their surface morphologies. The thin films were prepared by spin coating 2.0-wt% DMF solutions onto silicon substrates and subsequent thermal annealing at 180 °C for 3 h. The thin film thicknesses are 43 and 44 nm for **S6M3-MT** and **S4M4-MT**, respectively. The AFM phase image of **S6M3-MT** displays circular microdomains that appear to be arranged on a distorted hexagonal lattice that corresponds to the (110) plane of BCC (Figure 4.8a).[16–18] The intersphere distance ($d_{S-S,AFM}$) was determined to be 10.2 nm from the fast Fourier transform (FFT) image, which is similar to the $d_{SAXS}$ value. The AFM phase image of **S4M4-MT** exhibits a fingerprint-like pattern that corresponds to the horizontal HEX structure (Figure 4.8b). The intercylinder distance ($d_{C-C,AFM}$) was determined to be 12.9 nm from the FFT image, which is consistent with the value calculated from the SAXS profile of the bulk material ($d_{C-C,SAXS} = 2/\sqrt{3}d_{SAXS}$ = 13.0 nm).

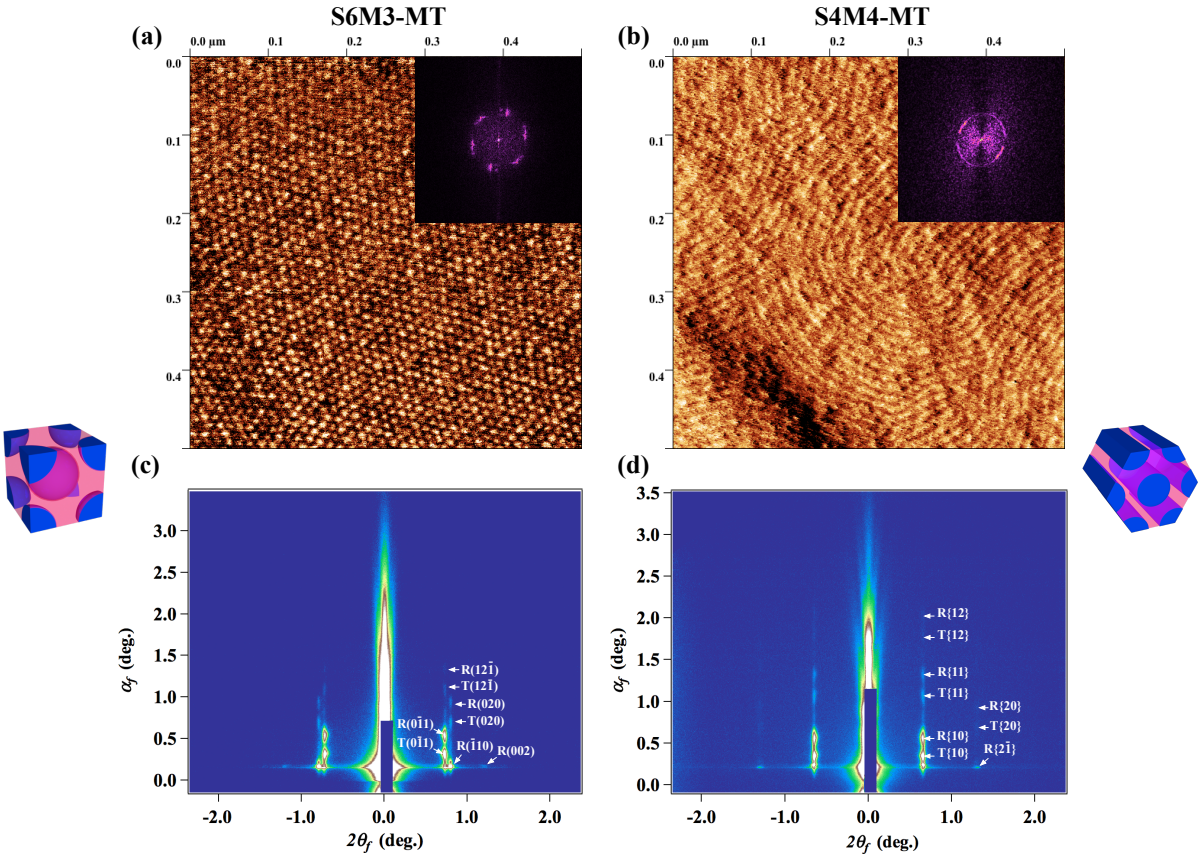


**Figure 4.8**. Morphological analyses of (a, c) **S6M3-MT** and (b, d) **S4M4-MT** thin films after thermal annealing at 180 °C for 3 h. (a, b) AFM phase images are displayed along with the corresponding FFT images. GISAXS patterns were acquired at $\alpha_i$ values of (c) 0.20° and (d) 0.15°. "R" and "T" refer to scatterings due to reflected and transmitted beams, respectively.

Grazing-incidence small-angle X-ray scattering (GISAXS) experiments were performed to further examine the morphologies inside the thin-film samples employed in the AFM experiments. The GISAXS data were acquired at several different incident angles ($a_i$s) to identify horizontally oriented component. The GISAXS image of **S6M3-MT** showed several scattering patterns splitting into reflected and transmitted ones at the $a_i$ of 0.20° (Figures 4.8c) while the scattering patterns without the splitting were observed at the $a_i$ of 0.15°. Note that the scattering spots marked by "T" and "R" represent the transmitted and reflected scatterings, respectively. The relative scattering vector lengths of R(0$\bar{1}$1), R(020), and R(12$\bar{1}$) were found to be 1, √2,

and √3, respectively, from the specular reflection position, suggesting that a BCC lattice had formed in the (110) plane parallel to the substrate, which supports the hexagonal packing observed by AFM. The *d* value was calculated to be 10.5 nm from the principal peak position observed at $a_f = 0.539$ and $2\theta_f = 0.730$, which corresponds to the $(1\bar{1}0)$ plane.[16,19–21] The GISAXS pattern of **S4M4-MT** exhibited five sets of splitting scatterings at the $a_i$ of 0.15° (Figures 4.8d) while the unsplitting scatterings were observed at the $a_i$ of 0.10°. The relative scattering vector lengths of R{10}, R{11}, R{20}, and R{12} were found to be 1, √3, √4, and √7, respectively, from the specular reflection position, consistent with a HEX lattice in which the {10} plane of the cylindrical microdomain is oriented parallel to the substrate. The *d* value was determined to be 11.1 nm from the scattering position due to the {10} plane, which is in good agreement with the {10} spacing ($d_{AFM}$) calculated from $d_{C-C,AFM}$ ($d_{AFM} = \sqrt{3}/2 d_{C-C,AFM} = 11.2$ nm). Hence, the author confirmed that **S6M3-MT** and **S4M4-MT** formed extremely small well-ordered patterns even in their thin-film states due to the contributions of the incorporated MT.

## 4.4 Conclusion

In summary, the author demonstrated that the incorporation of an oligosaccharide at the PMMA chain end is a facile and efficient modification technique for controlling the microphase-separation behavior of PS-*b*-PMMA. The terminal-selective transesterification demonstrated in this chapter is an extremely valuable tool for the introduction of an azido group at the PMMA chain end of PS-*b*-PMMA and facilitates further modification with a wide range of functional molecules through the use of click chemistry. The incorporation of a suitable oligosaccharide at the chain end induces a low-*N* PS-*b*-PMMA microphase separation with a sub-10-nm domain spacing; notably, the classical PS-*b*-PMMA is completely disordered prior to modification. This remarkable microphase-separation enhancement is attributed to the presence of the densely-integrated hydroxyl groups of the oligosaccharide segment. The strong aggregation of oligosaccharides at the chain ends contributes to a shift in the phase diagram of the diblock copolymer. The present strategy provides opportunities for PS-*b*-PMMA to form 10-nm-scale patternings that would lead to the development of further nanofabrication applications in light of their practical advantages.

## 4.5 References

1. Aissou, K.; Otsuka, I.; Rochas, C.; Fort, S.; Halila, S.; Borsali, R. Nano-Organization of Amylose-*b*-Polystyrene Block Copolymer Films Doped with Bipyridine. *Langmuir* **2011**, *27*, 4098−4103.

2. Cushen, J. D.; Otsuka, I.; Bates, C. M.; Halila, S.; Fort, S.; Rochas, C.; Easley, J. A.; Rausch, E. L.; Thio, A.; Borsali, R.; Willson, C. G.; Ellison, C. J. Oligosaccharide/Silicon-Containing Block Copolymers with 5 nm Features for Lithographic Applications. *ACS Nano* **2012**, *6*, 3424−3433.

3. Sakai-Otsuka, Y.; Zaioncz, S.; Otsuka, I.; Halila, S.; Rannou, P.; Borsali, R. Self-Assembly of Carbohydrate-*block*-Poly(3-hexylthiophene) Diblock Copolymers into Sub-10 nm Scale Lamellar Structures. *Macromolecules* **2017**, *50*, 3365−3376.

4. Otsuka, I.; Zhang, Y.; Isono, T.; Rochas, C.; Kakuchi, T.; Satoh, T.; Borsali, R. Sub-10 nm Scale Nanostructures in Self-Organized Linear Di- and Triblock Copolymers and Miktoarm Star Copolymers Consisting of Maltoheptaose and Polystyrene. *Macromolecules* **2015**, *48*, 1509−1517.

5. Otsuka, I.; Tallegas, S.; Sakai, Y.; Rochas, C.; Halila, S.; Fort, S.; Bsiesy, A.; Baron, T.; Borsali, R. Control of 10 nm scale cylinder orientation in self-organized sugar-based block copolymer thin films. *Nanoscale* **2013**, *5*, 2637−2641.

6. Otsuka, I.; Isono, T.; Rochas, C.; Halila, S.; Fort, S.; Satoh, T.; Kakuchi, T.; Borsali, R. 10 nm Scale Cylinder−Cubic Phase Transition Induced by Caramelization in Sugar-Based Block Copolymers. *ACS Macro Lett.* **2012**, *1*, 1379−1382.

7. Isono, T.; Ree, B. J.; Tajima, K.; Borsali, R.; Satoh, T. Highly Ordered Cylinder Morphologies with 10 nm Scale Periodicity in Biomass-Based Block Copolymers. *Macromolecules* **2018**, *51*, 428− 437.

8. Isono, T.; Otsuka, I.; Kondo, Y.; Halila, S.; Fort, S.; Rochas, C.; Satoh, T.; Borsali, R.; Kakuchi, T. Sub-10 nm Nano-Organization in AB2- and AB3-Type Miktoarm Star Copolymers Consisting of Maltoheptaose and Polycaprolactone. *Macromolecules* **2013**, *46*, 1461−1469.

9. Isono, T.; Otsuka, I.; Suemasa, D.; Rochas, C.; Satoh, T.; Borsali, R.; Kakuchi, T. Synthesis, Self-Assembly, and Thermal Caramelization of Maltoheptaose-Conjugated Polycaprolactones Leading to Spherical, Cylindrical, and Lamellar Morphologies. *Macromolecules* **2013**, *46*, 8932−8940.

10. Malkoch, M. Schleicher, K.; Drockenmuller, E.; Hawker, C. J.; Russell, T. P.; Wu, P.; Fokin, V . V . Structurally Diverse Dendritic Libraries: A Highly Efficient Functionalization Approach Using Click Chemistry. *Macromolecules* **2005**, *38*, 3663−3678.

11. Otsuka, I.; Fuchise, K.; Halila, S.; Fort, S.; Aissou, K.; Pignot-Paintrand, I.; Chen, Y.; Narumi, A.; Kakuchi, T.; Borsali, R. Thermoresponsive Vesicular Morphologies Obtained by Self-Assemblies of Hybrid Oligosaccharide-*block*-poly(*N*-isopropylacrylamide) Copolymer Systems. *Langmuir* **2010**, *26*, 2325–2332.

12. Daly, R.; Vaz, G.; Davies, A. M.; Senge, M. O.; Scanlan, E, M. Synthesis and Biological Evaluation of a Library of Glycoporphyrin Compounds. *Chem. Eur. J.* **2012**, *18*, 14671– 14679.

13. Ogura, Y.; Terashima, T.; Sawamoto, M. Terminal-Selective Transesterification of Chlorine-Capped Poly(Methyl Methacrylate)s: A Modular Approach to Telechelic and Pinpoint-Functionalized Polymers. *J. Am. Chem. Soc.* **2016**, *138*, 5012−5015.

14. Bates, F. S.; Schulz M. F.; Khandpur, A. K.; Förster, S; Rosedale, J. H. Fluctuations, Conformational Asymmetry and Block Copolymer Phase Behaviour. *Faraday Discuss.* **1994**, *98*, 7−18.

15. Matsen, M. W.; Bates, F. S. Conformationally Asymmetric Block Copolymers. *J. Polym. Sci., Part B: Polym. Phys.* **1997**, *35*, 945–952.

16. Stein, G. E.; Kramer, E. J.; Li, X. F.; Wang, J. Layering Transitions in Thin Films of Spherical-Domain Block Copolymers. *Macromolecules* **2007***, 40*, 2453− 2460.

17. Pitet, L. M.; Wuister, S.; Peeters, E.; Hawker, C. J.; Kramer, E. J.; Meijer, E. W. Well-Organized Dense Arrays of Nanodomains in Thin-Films of Poly(Dimethylsiloxane)-*b*-Poly(Lactide) Diblock Copolymers. *Macromolecules* **2013**, *46*, 8289−8295.

18. Minehara, H.; Pitet, L. M.; Kim, S.; Zha, R. H.; Meijer, E. W.; Hawker, C. J. Branched Block Copolymers for Tuning of Morphology and Feature Size in Thin Film Nanolithography. *Macromolecules* **2016**, *49*, 2318−2326.

19. Goodfellow, B. W.; Yu, Y.; Bosoy, C. A.; Smilgies, D. M.; Korgel, B. A. The Role of Ligand Packing Frustration in Body-Centered Cubic (bcc) Superlattices of Colloidal Nanocrystals. *J. Phys. Chem. Lett.* **2015**, *6*, 2406−2412.

20. Sinturel, C.; Grosso, D.; Boudot, M.; Amenitsch, H.; Hillmyer, M. A.; Pineau, A.; Vayer, M. Structural Transitions in Asymmetric Poly(styrene)-*block*-Poly(lactide) Thin Films Induced by Solvent Vapor Exposure. *ACS Appl. Mater. Interfaces* **2014**, *6*, 12146−12152.

21. Oveisi, H.; Suzuki, N.; Nemoto, Y.; Srinivasu, P.; Beitollahi, A.; Yamauchi, Y. Critical effect of aging condition on mesostructural ordering in mesoporous titania thin film. *Thin Solid Films* **2010**, *518*, 6714−6719.

# *Chapter 5*

## *Conclusions*

In this dissertation, the author proposed the ester-amide exchange reaction and terminal-selective transesterification as facile and efficient postpolymerization modification strategies of polystyrene-*block*-poly(methyl methacrylate) (PS-*b*-PMMA) to enable the microphase separation with a sub-20-nm-scale domain spacing. The ester-amide exchange reaction was utilized to convert a tiny amount of the methacrylates in the PMMA block into the methacrylamide units. The terminal-selective transesterification was performed to incorporate various functional groups into the $\omega$-chain end of the PS-*b*-PMMA. These postpolymerization modifications produced a series of PS-*b*-PMMAs with different side-chain and chain-end structures without any change in the degree of polymerization and dispersity, allowing one to extract the pure effect of these structures on the microphase-separation behaviors. A summary of the important achievements and findings in the present study is as follows:

*Chapter 2 "Ester-Amide Exchange Reaction of Polystyrene-block-Poly(methyl methacrylate) for Achieving Sub-10 nm Feature Size"*

The syntheses of the PS-*b*-PMMA derivatives having a series of methacrylamide units in the PMMA blocks were achieved by the ester-amide exchange reactions of PS-*b*-PMMA using various amines. Such PS-*b*-PMMA derivatives successfully formed microphase-separated structures with extremely small domain spacings unachievable by the bare PS-*b*-PMMA because of the presence of a tiny amount of the amide protons as well as hydroxy groups. Although several researchers designed the block copolymer (BCP) systems enabling the formation of the extremely small microphase-separated structures by using highly hydrophobic or hydrophilic segments, these BCPs suffer from practical disadvantages, such as complicated synthetic routes and high cost of the monomers. The side-chain modification strategy proposed in this chapter is a facile and efficient way to prepare BCP systems having a strong incompatibility from readily available BCP, i.e., PS-*b*-PMMA. In addition, the prepared PS-*b*-PMMA derivatives can be applied to the established standard nanofabrication process used for the bare PS-*b*-PMMA, thus demonstrating their practical utility.

*Chapter 3 Terminal-selective Transesterification of Polystyrene-block-Poly(methyl methacrylate) for Chain End Modification*

The chain-end modifications of the PMMA and PS-*b*-PMMA were accomplished by the terminal-selective transesterification. The terminal methacrylate unit in PMMA and PS-*b*-PMMA was selectively and efficiently transesterified in the presence of the alcohols and the corresponding titanium alkoxides. In this reaction system, various alcohols having hydrophobic, hydrophilic, and reactive functional groups can be used to synthesize a series of chain-end functionalized PMMAs and PS-*b*-PMMAs. The incorporation of the reactive functional groups into the polymer chain end of the unliving polymer is significantly important from the polymer synthesis point of view because it allows polymers to undergo a further chain-end modification. In addition, the author found that the hydroxy-functionalized polymers, *i.e.*, the poly(ethylene glycol) monomethyl ether, can also be applied to the reaction system to incorporate a polymer segment into the PMMA-chain end. The chain-end modification strategy established in this chapter provides a wide array of BCP systems with various chain-end structures and used as a novel synthetic approach for the PMMA-based BCPs. In addition, this strategy enables the investigation of the pure effect of the chain-end structure on the microphase-separation behaviors.

*Chapter 4 Chain-End Functionalization with a Saccharide for 10-nm Microphase Separation: "Classical" PS-b-PMMA versus PS-b-PMMA-Saccharide*

A series of PS-*b*-PMMAs having an oligosaccharide at the PMMA-chain end was synthesized by the terminal-selective transesterification with the azido-functionalized alcohol followed by the click reaction using the ethynyl-functionalized oligosaccharides. This novel BCP design that incorporates the oligosaccharide into the PMMA-chain end induces the microphase separation even in the low-molecular-weight region, producing extremely small nanostructures. The strong aggregation of the oligosaccharide at the chain end significantly affects the microphase-separation behavior of PS-*b*-PMMA, enabling the morphological fine-tuning. The proposed chain-end modification using an oligosaccharide is a powerful tool to fabricate the microphase-separated structures with a 10-nm-scale domain spacing from the readily-available PS-*b*-PMMA.

In conclusion, the author established the postpolymerization modification strategies enabling the PS-*b*-PMMA to form microphase-separated structures with a 10-nm-scale domain spacing. The findings obtained in the present study provide an insight into the BCP design for increasing the incompatibility between the blocks while keeping the original polymer backbones. Especially, the incorporation of the hydrophilic moieties into the side chain and chain end of the PMMA block was proved to be a powerful tool for increasing the incompatibility between the blocks, leading to the microphase separation in the low-molecular-weight-region. The PS-*b*-PMMA derivatives prepared in this dissertation are amenable to the established nanofabrication process using the bare PS-*b*-PMMA because they retain the original polymer backbone. Therefore, the author believes that the results obtained from the present study offer a better guidance to the fabrication of the extremely small nanostructures from the industrially-useful BCP, PS-*b*-PMMA, which leads to further development of the nanotechnologies based on the BCP microphase separation.